Towards an active acoustic anechoic chamber

Rick Haasjes

Towards an active acoustic anechoic chamber

DISSERTATION

to obtain
the degree of doctor at the University of Twente,
on the authority of the rector magnificus,
prof. dr. ir. A. Veldkamp,
on account of the decision of the Doctorate Board
to be publicly defended
on Monday 20 January 2025 at 14.45 hours

by

Rick Haasjes

born on the 9th of July, 1997
in Barneveld, the Netherlands

This dissertation has been approved by:

Promotor:
prof. dr. ing. B. Rosić

Co-promotor:
dr. ir. A.P. Berkhoff

Cover design: Dionne van Maanen & Rick Haasjes
Printed by: Gildeprint
Lay-out: Rick Haasjes
ISBN (print): 978-90-365-6282-9
ISBN (digital): 978-90-365-6283-6
URL: https://doi.org/10.3990/1.9789036562836

Graduation Committee:

Chair / secretary:	prof. dr. ir. H.F.J.M Koopman
Promotor:	prof. dr. ing. B. Rosić University of Twente
Co-promotor:	dr. ir. A.P. Berkhoff University of Twente TNO
Committee Members:	prof. dr. ir. M.J. Bentum Eindhoven University of Technology
	prof. dr. ir. G.J.T. Leus Delft University of Technology
	prof. dr. ing. P. Gardonio University of Udine
	prof. dr. ir. P.H. Veltink University of Twente
	prof. dr. ir. C.H. Venner University of Twente

Summary

An acoustic anechoic chamber is a space in which no reflections occur at the walls. The acoustic anechoic chamber therefore approaches free-field conditions, in which no reflections occur either. Acoustic free-field conditions allow measurements to be conducted without contamination from any boundary. The free-field conditions are realized with special laboratory facilities known as acoustic anechoic chambers. This allows for standardization, product testing, research and development and calibration, all under free-field conditions. The sound absorption in an acoustic anechoic chamber is typically realized by using absorption material, which is placed at the boundaries of the room. However, because the thickness of the absorption material is related to the wavelength of the acoustic waves, the performance of the absorption material deteriorates at lower frequencies. Consequently, a typical acoustic anechoic chamber has a lower cut-off frequency of up to 200 Hz, meaning that free-field conditions are not guaranteed below this frequency.

Active noise control is effective at lower frequencies, which therefore makes it a promising technique to complement the passive absorption and to lower the cut-off frequency of an acoustic anechoic chamber. To implement an active noise control system in an acoustic anechoic chamber, an accurate estimation of the reflected sound field is necessary. The solution to this problem is found in the application of the Kirchhoff-Helmholtz integral, which in two dimensions uses several microphones distributed along a circle. The microphones measure the acoustic pressure and the particle velocity, which are the input to the Kirchhoff-Helmholtz integral. The output of the Kirchhoff-Helmholtz integral is the reflected sound field due to any source located within the circle, while for any source located outside the circle it outputs the total sound field.

With increasing geometry sizes, more complex geometries and smaller wavelengths, the active noise control system needs to be up scaled. This means that a larger number of microphones is required to accurately measure the sound field, and a larger number of sources is required to accurately generate the secondary sound field. This results in a strong increase in computational complexity and memory consumption. Low computational complexity and memory consumption are important features of the desired algorithms. Three algorithms are derived. Two algorithms

achieve the largest reduction in computational complexity and memory consumption by computations in the frequency domain. However, filters that are computed in the frequency domain are not necessarily causal, which is necessary for real-time implementation. Therefore, techniques to ensure causality are applied at the one of the algorithms, allowing the use of this algorithm for real-time systems. One of the algorithms is computed in the time domain and therefore has the highest computational complexity and memory consumption, but in comparison with the other two algorithms, relaxes some requirements to reduce frequency domain artifacts.

The algorithms, together with the Kirchhoff-Helmholtz integral, are used in two-dimensional numerical studies and two-dimensional experiments. In the numerical studies a small-scale and a large-scale chamber are simulated. The results of these numerical studies show that the Kirchhoff-Helmholtz integral, together with two of the derived algorithms is effective at the suppression of the reflections from the walls and allows the number of microphones and loudspeakers to be increased. To verify the real-time effectiveness, an experimental setup is built. The experiments are conducted on a setup which is limited in its height so that it is considered two-dimensional within the frequency range of interest. The setup is equipped with 12 sensors along a circle. Each sensor has three microphones which are distributed in radial direction, to measure the acoustic pressure and to approximate the particle velocity. The results of the real-time experiments show a significant reduction in reverberation time, which is an indication of effective suppression of reflections.

Samenvatting

Een akoestische, anechoïsche kamer is een ruimte waarin geen reflecties optreden aan de wanden. De akoestische anechoïsche kamer benadert daarmee de vrije-veld voorwaarden, waarin ook geen reflecties optreden. Akoestische vrije-veld voorwaarden maken het mogelijk om metingen te doen zonder beïnvloeding van de omgeving. Om die reden wordt een vrije-veld omgeving benaderd met een zogenaamde akoestische anechoïsche kamer. Dit maakt standaardisatie, het testen van producten, kalibratie van meetapparatuur, onderzoek en ontwikkeling binnen deze vrije-veld omgeving mogelijk. De geluidabsorptie in een akoestische anechoïsche kamer wordt doorgaans gerealiseerd met absorptiemateriaal, dat aan de wanden van de kamer wordt gemonteerd. Echter, omdat de dikte van het absorptiemateriaal gerelateerd is aan de golflengte van de akoestische golven, verslechtert de prestatie van deze absorptie bij lagere frequenties. Om die reden heeft een typische akoestische anechoïsche kamer een kantelfrequentie van tot wel 200 Hz. Dit betekent dat aan de vrije-veld omstandigheden onder deze frequentie niet wordt voldaan.

Actieve geluidbeheersing is effectief bij lagere frequenties, wat om die reden een veelbelovende techniek is om de passieve absorptie aan te vullen en de kantelfrequentie van een akoestische echovrije kamer te verlagen. Om een actief geluidbeheersingssysteem in een akoestische echovrije kamer te implementeren, is een nauwkeurige schatting van het gereflecteerde geluidveld noodzakelijk. De oplossing voor dit probleem is gevonden in het gebruik van de Kirchhoff-Helmholtz integraal, die in twee dimensies een aantal microfoons verdeeld over een cirkel gebruikt. Met de microfoons worden de akoestische druk en de deeltjessnelheid bepaald, wat de invoer is voor de Kirchhoff-Helmholtz integraal. Het resultaat van deze integraal is het gereflecteerde geluidveld als gevolg van een bron die zich binnen de cirkel bevindt, terwijl het voor elke bron die zich buiten de cirkel bevindt het totale geluidveld geeft.

Met toenemende geometriegroottes, complexere geometrieën en kleinere golflengtes moet het actieve geluidbeheersingssystem worden opgeschaald. Dit betekent dat een groter aantal sensoren nodig is om het geluidveld nauwkeurig te meten en een groter aantal bronnen om het secundaire geluidveld nauwkeurig te genereren. De rekenkundige complexiteit en geheugengebruik van de algoritmes neemt

dan sterk toe. Een lage complexiteit en beperkt geheugengebruik is een belangrijk kenmerk van de gewenste algoritmes. Er worden drie algoritmes afgeleid. Twee algoritmes bereiken de grootste vermindering in rekenkundige complexiteit en geheugenverbruik door berekeningen in het frequentie domein. Echter, filters die in het frequentie domein worden berekend zijn niet noodzakelijkerwijs causaal, wat een vereiste is voor een real-time implementatie. Daarom worden technieken toegepast om causaliteit te garanderen bij één van de algoritmes, die het gebruik van het algoritme voor real-time systemen mogelijk maken. Eén van de algoritmes wordt in het tijd domein berekend en heeft daardoor de hoogste rekenkundige complexiteit en het hoogste geheugenverbruik. Vergeleken met de andere twee algoritmen is dit algoritme eenvoudiger in gebruik, omdat er geen rekening hoeft te worden gehouden met frequentie domein artefacten.

De algoritmen, samen met de Kirchhoff-Helmholtz integraal, worden gebruikt in tweedimensionale numerieke studies en tweedimensionale experimenten. In de numerieke studies worden een kleine en een grote kamer gesimuleerd. De resultaten van deze numerieke studies tonen aan dat de Kirchhoff-Helmholtz integraal samen met twee van de gepresenteerde algoritmen effectief is in het onderdrukken van de reflecties en het mogelijk maakt om op te schalen naar grotere afmetingen. Daarnaast is een experimentele opstelling gebouwd, zodat de realtime effectiviteit geverifieerd kan worden. De experimenten zijn uitgevoerd op een opstelling die beperkt is in hoogte, zodat deze als tweedimensionaal beschouwd kan worden binnen het belangrijkste frequentiebereik. De opstelling is uitgerust met 12 sensoren geplaatst langs een cirkel. Elke sensor is uitgerust met drie microfoons die in radiale richting zijn verdeeld, om zowel de meting van de akoestische druk mogelijk te maken, als de deeltjessnelheid te bepalen. De resultaten van de real-time experimenten laten een significante vermindering van de nagalmtijd zien, wat wijst op een effectieve onderdrukking van de reflecties.

Contents

Chapter 1

Introduction

If you heard the noise living inside of me, you would never question my love for silence.

Stephanie Bennett-Henry, November 2016

1.1 Background

Sound is ever-present in our daily lives. Sound can be pleasant, when we listen to our favourite music, have conversations, or enjoy the sounds of birds chirping during a walk. Unfortunately, unpleasant or annoying sounds exist too, these are typically referred to as noise. Examples are traffic noise, loud machines in factories, airplanes flying by, a vacuum cleaner, etc. Sound, but in general noise, can have a negative impact on our health. In the case of exposure to high sound pressure levels, hearing damage might occur. Furthermore, noise can have a negative impact on our mental health [1].

Acoustics is the science of sound, including its generation, transmission and reception. As well as being unpleasant to humans, noise is also undesirable in most engineering experiments, as it could refer to any fluctuation in the data that hinders the perception of a signal. A specific example is the situation of an acoustic free-field measurement. In free-field conditions the sound pressure level (SPL) decreases by 6 dB for every doubling of the distance between the source and receiver [3], while in non-free-field conditions the reflected sound affects the result. Therefore, the acoustic radiation of an arbitrary object needs to be studied under free-field conditions, such that no reflections from the boundaries or noise signals from outside sources contaminate the measurements. It is, however, not easy to obtain and maintain an acoustic free-field environment. Consequently, special laboratory facilities named acoustic anechoic chambers (AAC) [4] are studied and built, see Fig. 1.1.

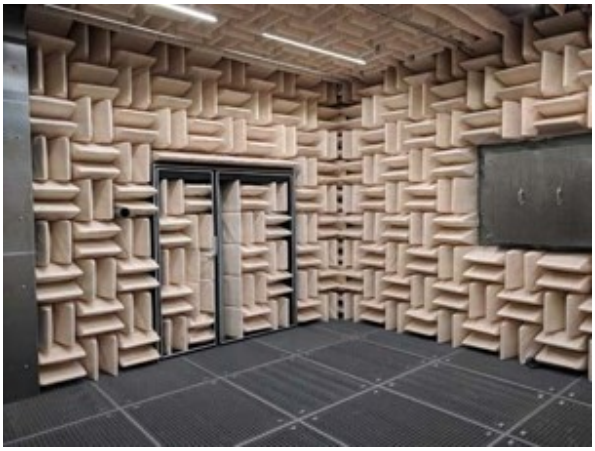

Figure 1.1: Anechoic chamber at the University of Twente [2].

1.2 Acoustic anechoic chamber

An AAC is designed to absorb acoustic waves at its boundaries, effectively creating a free-field environment that simulates an infinitely large chamber. Common applications of an AAC are in the automotive, military and aerospace industries. More specifically, a typical application of an AAC is found in one of the following categories:

1. *Standardization*: Many acoustic standards and specifications require free-field conditions to ensure consistency and comparability of measurements across different studies and applications. The general requirements for AACs are given in ISO 3745 [5], which to this date is the relevant ISO standard for AACs.

2. *Product testing*: In developing audio equipment (e.g. speakers [6,7] and hearing aids [8]) , as well as in aeroacoustic experiments [9], free-field measurements are crucial for evaluating the true performance of the product without environmental influences.

3. *Research and development*: For scientific research in acoustics, understanding the fundamental properties of sound waves in a controlled environment is essential. An example of a controlled environment is the (ideal) free-field condition [10].

4. *Calibration*: Free-field measurements are used to calibrate instruments and devices accurately, ensuring correct readings in various environments. An example is the calibration of microphones with the free-field conditions [11–13].

It is important to mention that alternatives to free-field measurements of loudspeakers are proposed in [14–16]. However, the use of an anechoic room for loudspeaker response measurements remains recommended [17]. An AAC should be calibrated, to confirm whether it approaches infinite free space. The most common method

to calibrate an AAC is to compare the decrease in pressure as the observer moves away from the sound source, with the inverse square law [18], which describes how the intensity of sound decreases as the distance from the sound source increases in situations without reflections [2, 19, 20].

In an AAC the anechoicity can be achieved with the use of passive absorption elements. An overview of passive sound absorption techniques and methods is given in [21], where it is shown that different factors play a role in the absorption of sound; these include the material, the thickness of the absorption layer, the amount of porosity in the absorption layer, internal friction or internal damping, the difference between a completely hard back wall or a layer of air behind the absorption layer, and the mounting method. These parameters influence the cut off frequency of the absorption element [18]. The absorption elements are specified with a cut off frequency, i.e. an expression of the lower frequency limit above which the pressure reflection rises to 10% of the pressure in a normally-incident wave [18]. This lower frequency limit corresponds to the frequency at which the absorption of the sound energy drops to 99% for normally-incident waves [7], which can be measured in an impedance tube [22]. Furthermore, the cut off frequency could also refer to the lower frequency limit above which the AAC shows anechoic behaviour. In that case, the cut off frequency is determined by the volume of the AAC, and the absorption surface, and depends on the configuration and type of the absorption elements. However, the cut off frequency of the absorption elements is not necessarily equal to the cut off frequency of the AAC, as is shown in [22, 23].

The main elements used in AACs are sound-absorbing wedges. These elements are cone-shaped, pyramid-shaped or wedge-shaped, and are designed in different dimensions and mounted on the boundaries of the chamber in specific arrangements [24]. If the floor of the chamber is not covered with elements, this is called a semi-anechoic chamber, which models the conditions of sound reflection from the ground [9], and also allows for heavy test-equipment to be installed in the chamber. In [18] five sound-absorbent samples with various shapes have been examined, in which the wedge-shaped element made of fibreglass was found to be the most effective to absorb the sound waves. Other studies to optimize the absorption of the elements have been conducted [22, 25–28]. These papers analyse the influence of porosity of the wedge materials, different shapes, dimensions and materials on the sound absorption. In the ideal case, all acoustic waves are absorbed at the walls due to these elements, eliminating the presence of reflections. However, because the thickness of the absorption material is related to the wavelength of the acoustic waves, the performance of passive absorption measures deteriorates at lower frequencies. At lower frequencies, and thus longer wavelengths, the size of the absorption material would increase so much that physical implementation is no longer feasible because of the reduced available space. Besides the shortcomings of the absorption techniques, the dimensions of the AAC also play a role. If the volume of the AAC becomes smaller than the Fresnel volume [29], the amplitudes of forward scattered waves are then affected [30]. The Fresnel volume is a region around the direct path between a source and receiver pair which can significantly influence the behaviour of the sound waves, primarily due to diffraction and interference effects.

In [31] an AAC designed with a cut off frequency of 75 Hz is studied, which showed perturbations in the 110 to 160 Hz frequency range. Therefore, the cut off

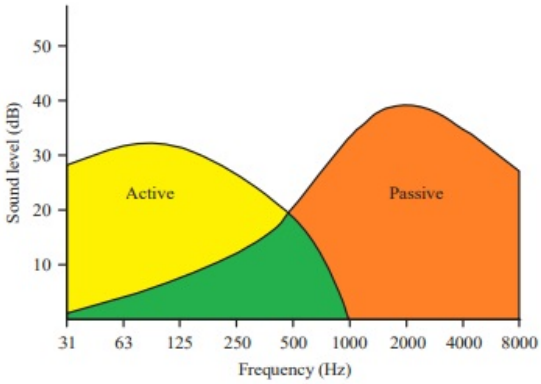

Figure 1.2: Frequency response region of the active and passive noise control methods. Image taken from [37].

frequency lies at 200 Hz rather than 75 Hz. One of the identified causes of imperfections is the doors in the AAC, even though they are fitted with acoustic lining. In [18] measurements in the Harvard University's AAC are compared with the theoretical inverse square law, which, dependent on the distance from the source, starts to show larger deviations below about 100 Hz. In [32] the measurements in the AAC at the Universidad Nacional Autónoma de México have been compared with the theoretical inverse square law. The largest deviations, depending on the source location and the distance from the source, start to show below 200 Hz, and increase for decreasing frequencies. Design principles of an acoustic anechoic chamber are described in [33–35], highlighting the design efforts required to lower the cut off frequency.

At this point it can be concluded that AACs suffer from low-frequency sound waves (up to about 200 Hz) reflecting off the walls, in some cases even above the cut off frequency the chamber is designed for. Hence the problem of lowering the cut off frequency is challenging. A solution to the low-frequency reflections may be found in the application of active noise control (ANC) [36]. Passive methods rely on materials and structures to absorb sound, while active methods involve electronic systems that detect the noise and generate counteracting sound waves. The effective frequency regions of the active and passive methods are indicated in Fig. 1.2. The figure shows the effective frequency range of the active and passive methods expressed in dB. It can be seen from the figure that active methods are typically more effective in the lower frequency range, while the passive methods are effective from the medium to high frequency range. Consequently, in this thesis, the feasibility, the solution strategies and the practical implementation of ANC to suppress the low-frequency reflections are studied.

1.3 Active noise control

ANC is a method to suppress undesired noise by the addition of a secondary signal (anti-noise signal) to cancel the existing noise signal. Examples of current applica-

tions are the implementation of ANC in the exhaust of a crawler crane [38], in a diesel generator in a luxury yacht [39], at a power transformer station [40], in an elevator cabin [41], and an active noise barrier for mitigation of noise from a construction site [42]. In ANC, control architectures can generally be realized in feedback or feedforward configurations or a combination of both, sometimes referred to as a hybrid system [43]. In the feedback architecture the error signal is measured and used to generate the control signals. With the feedforward architecture, reference signals are measured and used to generate the control signals, with the assumption that an upstream reference signal that is correlated to the disturbance signal is available. The term upstream refers to the requirement that the reference signal should have sufficient time-advance compared to the disturbance signal, whereby the control system is able to compute the control output. In acoustic control systems, this time-advancement of the reference signals is typically obtained through an advantageous spatial distance between the reference sensor and the location of noise suppression. Usually, a feedback architecture is used in situations where a correlated reference signal is not available. Often, when a feedforward system is considered in literature, it is assumed that either a purely feedforward system is available, or that any existing feedback loop from the secondary sources to the reference sensors is mitigated using internal model control (IMC) [44].

The simplest implementation of an ANC system is a single-input single-output (SISO) system. However, for more complex dynamic systems, increasing frequencies or larger geometries, a SISO system might result in poor performance. In such cases a system with multiple-inputs and multiple-outputs (MIMO) is required [44]. A decentralized MIMO control realization [45] is the combination of multiple SISO controllers, which, however, might influence each other. A centralized MIMO system [44], is a realization in which the influence of all sensor-loudspeaker combinations is taken into account with one single control unit. A distributed control system is composed of multiple localized controllers, which each have the ability to communicate with other controllers in the system [46]. A comparison between decentralized, centralized and distributed control is shown in [47]. The performance of a decentralized control architecture is typically inferior to that of a centralized control architecture [47, 48]. Furthermore, a distributed architecture requires sufficient bandwidth to allow real-time processing, and in general the communication delay reduces the performance [46, 49]. An effective ANC system requires spatial sampling of the microphone and loudspeaker distributions. The control capabilities of an ANC system depends, among other things, on the amount of distortions due to spatial aliasing [50]. For an enhanced bandwidth and for larger quiet zones, which is an area in which the ANC system suppresses the disturbances, a sufficient number of sources and sensors is required. However, computing the set of control filters for ANC systems with a large number of sources and sensors is computationally expensive, which is a problem studied in this thesis.

An active control system cancels the existing noise by the addition of a secondary signal, generated by the secondary sources. In the ideal case, the secondary signal is of the same amplitude but opposite phase as the noise signal. The simplest realization of an active control system consists of at least three different components: 1) (Multiple) sensors which measure the noise or a reference signal. 2) A secondary actuator, which generates the anti-noise or secondary signal. 3) A computer, the

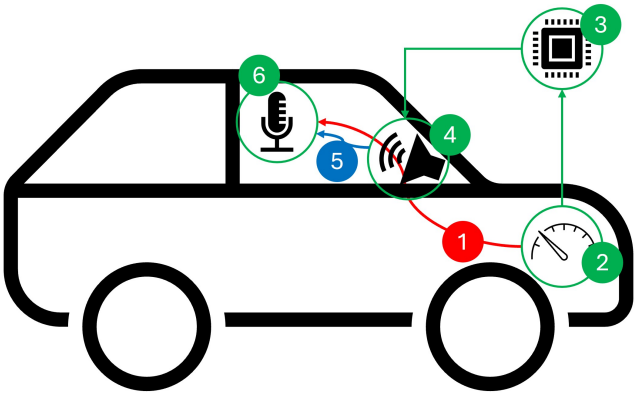

Figure 1.3: An illustration of a SISO feedforward active noise control system in a car, using a reference acceleration sensor (2), a control computer (3), a secondary loudspeaker (4) and an error microphone (6).

controller, which generates the control signal and drives the secondary actuators. An illustration of a SISO feedforward active noise control system is given in Fig. 1.3, in which the components (2), (3), (4) and (6) are involved with the control system, indicated by the colour green. The engine in the front of the car is running and generates noise. The noise travels to the interior of the car, indicated by the number 1 in red, which is undesirable. A reference acceleration sensor (number 2) is placed next to the engine and measures the upstream reference signal. The controller (number 3), drives the secondary source (number 4), based on the measured reference signal. The secondary source generates the (anti-noise) secondary signal (number 5 in blue), which cancels the noise signal. The error microphone (number 6) measures the residual noise. In this example a reference acceleration sensor (number 2) is used, but this could be any other type of sensor, which is problem dependent.

In the illustration of 1.3, a controller (number 3) is used. However, this controller needs instructions on what to do. In the linear case, this is typically described by a set of control coefficients that are uploaded to the control system. With the feedforward configuration, the control coefficients are applied to the upstream reference signals to generate the control output, which drives the secondary sources. The set of control coefficients can be obtained with offline and online algorithms, as described below.

Offline algorithms are typically used to pre-compute the optimal set of control

filters. In such cases, the controller is designed using a model of the complete ANC system, including its sources and sensors. The drawback of the offline approach is that the control coefficients are fixed, and that while running the control algorithm, the system is not able to adapt to variations in either the plant or disturbance. The advantage of this approach is that the real-time computational load is lower in comparison with adaptive algorithms, because the control coefficients are not updated while running the real-time control system. Furthermore, adaptive algorithms require time to converge, which is not the case with the offline approach. In the frequency domain, the optimal set of control filters minimizes the power spectral density of the squared error signal at each frequency. If the control problem is not causally constrained, the obtained set of control filters is not necessarily causal [44]. To obtain a set of causal control coefficients, the controller is constrained to be causal, which for MIMO systems is not so trivial. In the time domain, the optimal set of control filters that minimizes the expectation of the sum of squared error signals is called the Wiener set of filter coefficients [44]. The Wiener filter is obtained by solving a set of linear equations. For larger system sizes, with increasing numbers of sources and sensors, this becomes computationally expensive. In the case of MIMO systems, the set of linear equations to be solved for involves a Toeplitz-block matrix [44], which allows for efficient solvers, as explained in more detail in the next chapters.

In addition to offline algorithms there are online algorithms, also named adaptive algorithms, which are used to sequentially adjust the filter coefficients so that they evolve in a direction that minimizes the mean-square error. The benefit of this type of algorithm is that the filter coefficients are automatically re-adjusted if the correlation properties of the disturbance signals change. Therefore, the adaptive filter may be capable of tracking the statistics of non-stationary signals, provided the changes in the statistics occur slowly compared with the convergence time of the adaptive filter. With the online algorithms, the control coefficients are iteratively adapted while running the control system, under the assumption that the filter coefficients are changing slowly in comparison with the timescale of the plant dynamics. Well known algorithms for this purpose are the filtered-reference least mean squares (FxLMS) and filtered-error least mean squares (FeLMS) algorithms [44]. The drawback of the adaptive algorithms is the choice of step size, which, if chosen incorrectly results in slow convergence, or even divergence of the cost function, which is typically chosen as a function of the error signal. The choice of the step size is simplified by the introduction of a variable step size [51] and normalized step size [52] versions of the adaptive algorithms, where the control update step is scaled with the input power. For systems with multiple reference signals, the FeLMS algorithm is favourable in terms of computational complexity, although its convergence speed is lower than that of the FxLMS algorithm. The FeLMS algorithm uses a transpose plant model to filter the error signal, which is inherently non-causal. To ensure a causal system, the error signal is filtered with a delayed and time-reversed version of this plant model. However, the delay in the error signal is also matched with a delay in the reference signal, which in practice reduces the convergence speed. Furthermore, non-white, correlated reference signals and secondary path frequency dependence of the adaptation loop negatively affect the convergence speed of the FeLMS algorithm. Therefore, the preconditioned filtered-error algorithm is introduced in [44], which whitens and decorrelates the reference signals and uses the inverse of the minimum-phase

and the all-pass parts of the plant to reduce frequency dependence in the adaptation loop. A frequency domain approach to compute the prewhitening and decorrelation filter and to decompose the secondary path is shown in [53]. In [54] a regularized modified filtered-error algorithm is presented, which uses the minimum-phase and all-pass decomposition but is computed with an inner-outer factorization method. The delay in the adaptation loop is compensated in combination with double control filters, which are copied after every update. The algorithm also incorporates regularization to prevent high gains in the inverse of the minimum-phase part and prevents saturation of the control signal. Higher-order adaptive algorithms can improve convergence rate, with the downside of increased computational complexity per iteration. The Newton iteration [55] is a higher-order method, which, requires the auto-correlation matrix that can be challenging to compute. Another higher-order method is the recursive least squares (RLS) algorithm [56], which also requires the auto-correlation matrix. The robustness and computational complexity are major limitations of this algorithm. Fast implementations and more robust versions of the RLS algorithms are proposed in [57, 58]. One important remark to make at this point is that although these algorithms are presented as online algorithms, they can also be used in an offline manner, to iteratively pre-compute a fixed set of control filters, using a copy of the time history of the measured signals involved. If a perfect plant model is available and assuming that the adaptive algorithm is stable, the filter coefficients converge to the optimal set of filter coefficients in the steady state [44].

Typically, control algorithms used in ANC are model-based control design methods, which means that an (accurate) model of the systems involved is incorporated in the design process [59]. Considering model-based control design in the time domain, systems with a lightly damped resonant system are generally modelled with an infinite impulse response (IIR) filter [44], which as the name suggests takes an infinite time to decay. An example of a system that is typically modelled with an IIR filter is the structural response of an aluminum plate [44]. Conversely, systems with moderate to high damped resonances are generally modelled with a finite impulse response (FIR) filter [44], which is described by a finite number of time samples until the response has decayed. Provided that the coefficients are bounded, an FIR filter is always stable, while an IIR filter is not necessarily stable [44, 60]. An IIR filter is also more susceptible to finite bit precision effects than an FIR filter [61]. Contrary to FIR models, state-space models [62] are not common in ANC applications. The use of state-space models make it possible to take advantage of modern control design tools [63], to design a controller by solving Lyapunov equations, algebraic Riccati equations or linear matrix inequalities [64]. However, it is necessary to obtain an accurate MIMO state-space model. Although black-box subspace model identification methods [65–67] can be employed to estimate a state-space model, it is difficult for high-order systems frequently encountered in ANC [53]. In acoustics, most systems have relatively high damping, which means that they can typically be modelled with short FIR filters. Therefore, most algorithms developed for ANC are using the FIR structure.

Similarly to the adaptive algorithms, which iteratively adapt the set of filter coefficients, a machine learning model can be trained and employed as an instruction set to be uploaded to the controller. The use of machine learning is especially valuable in cases of system non-linearities, since previously introduced algorithms assume

linearity, and machine learning models are able to capture non-linearity. Nonlinear systems are different from linear systems in the sense that they do not obey the principle of superposition [44]. Machine learning covers the field of computer algorithms that can adapt either through experience, called reinforcement learning, or using data, which can be supervised or unsupervised. Typically, a supervised learning model is used to train the model in ANC applications. An example of a supervised implementation is a multilayer perceptron network in combination with the backpropagation algorithm [44]. In such a configuration, the output of the network is compared with a known desired signal and the error between the two is used to adjust the weights in the layers starting from the output layer until the input layer is reached. An example of this approach is shown in [68]. Another supervised implementation is shown in [69], a convolutional recurrent network is employed to estimate the secondary signal from the reference signal. The model is equipped with convolutional layers and deconvolutional layers with long short-term memory layers in between. The inputs of the model are the complex spectrograms of the reference signals, computed with a short time Fourier transform. The outputs of the model are the complex spectrograms of the secondary signal, which after the inverse Fourier transform result in the secondary signal in the time domain. The secondary signal summed with the primary noise signal results in the error signal. The loss function is defined as the mean-squared of the error signal, which is minimized to eliminate the primary noise. A similar supervised learning method is shown in [70], in which a convolutional neural network (CNN) is implemented on a field programmable gate array for in-ear headphone feedforward ANC. Due to the small dimensions of an in-ear headphone, the processing delay is longer than the acoustic propagation delay, resulting in challenging causality constraints. In [70] it is stated that the causality constraint is relaxed by employing a dilated CNN model to predict future data. However, existing algorithms also allow to predict future data, for example the prediction-error filter [71, 72]. Furthermore, with the application of ANC in an AAC, the causality constraint is not as challenging, due to the larger dimensions. Another machine learning approach is reinforcement learning, which is based on interaction with the environment to achieve its goals, i.e. how to map situations to actions. The most popular and simplest version is the Q-learning method, of which an ANC implementation is shown in [73]. The method uses an action-value table (Q), which represents the expected future rewards in a state when an action is selected. In this work, the control output signal is defined as a signal with tunable parameters. The action set consists of the three options to 1) increase or 2) decrease the parameters in the control output signal or 3) take no action. A simulation for a narrow band single tone in a duct and a simulation for a narrow band with multiple tones is shown. A similar approach is presented in [74], in which instead of positive rewards a negative reward is used which is proportional to the error signal. The method has good robustness but comes with a long settling time and huge memory requirements, which is not ideal for implementations in an AAC.

In general, an ANC system is equipped with microphones to measure the acoustic pressure, which is being suppressed with the secondary signal that is generated by the set of control filters. However, to effectively apply ANC to suppress the low-frequency reflections in an AAC, knowledge about the acoustic pressure does not suffice. Instead, a method to accurately determine the reflected sound field is nec-

essary. In this case the set of control filters can be designed to suppress the sound pressure due to the reflected sound waves instead of the total acoustic pressure.

1.4 Approximation of the reflected sound field

The total sound field is the sum of the reflected sound field and the direct sound field. However, both the reflected sound field and the direct sound field are non-measurable quantities. The total sound field can be measured but does not have any information about either the reflected sound field or the direct sound field. This section describes existing work to estimate the reflected sound field or methods to derive filters that can translate the total sound field to the reflected sound field, allowing the implementation of an ANC system to suppress the acoustic reflections. In the one-dimensional case, assuming normal incidence, the incident and reflected waves can be separated using the integration method, as shown in [75]. The approach utilizes two microphones which are placed a few centimeters apart. As long as the distance between both microphones is smaller than the smallest wavelength of the sound, simplifications can be made which allow evaluation of the spatial pressure derivative and the particle velocity. With the pressure derivative and the particle velocity, both incident and reflected wave quantities can be computed. However, this does not generalize to situations with more dimensions. A different approach is presented in [76, 77], in which the control of scattered acoustic radiation from a three-dimensional object is shown. The total noise is mapped to the scattered noise using a linear scattering filter. This scattering filter is deduced from two series of measurements with and without the diffracting object. The problem was found to be ill-conditioned, however, and requires regularization. Furthermore, in the case of an AAC, the reflections are coming from the boundaries of the chamber. This means that it is not possible to remove the diffracting object, making this approach unsuitable for application in an AAC. In [78] an integral relation is used to estimate the scattered field from the total pressure observed with microphones. This integral relation results in a mathematical operator, a matrix of filters to be applied on the error microphones. To obtain the mathematical operator, identification sources, of which the sound radiation patterns are known, are used to minimize the difference between the diffracted pressure and the output of the mathematical operator. However, discretization and regularization of the inverse problem are open questions. Furthermore, the design of a reference source with a known radiation pattern at lower frequencies is not so trivial, and might need improved low-frequency calibration solutions [79]. Another approach to separate the ingoing and outgoing wave fields is introduced in [30]. This method uses immersive boundary conditions (IBC) to virtually expand a physical domain. The full domain is seen as the physical domain embedded within a virtual domain. In between the physical and the virtual domain is a region that is bounded on the inner boundary by the recording surface, and on the outer boundary by the emitting surface. To separate the ingoing and outgoing wave fields, the extrapolated particle velocity of the full domain is required ahead of time. This particle velocity is obtained by using the Kirchhoff-Helmholtz integral to extrapolate the wave fields from the recording surface to the emitting surface. The particle velocity at the recording surface is then also required; this is obtained

through a finite-difference approximation with pressure measurements integrated in time. To account for differences in sensor coupling, inaccuracies in the estimated medium properties and sensor separation distance, and errors introduced due to the pressure interpolation and discretization of the finite-difference approximation time integral, a pre-computed frequency-dependent calibration filter is applied. The downside of this approach is the assumption of ideal sources and sensors for which a calibration solution is not shown. A completely different approach, to remove the imprint of the boundaries after the experiment has taken place, is shown in [80]. In this work, a multidimensional deconvolution method (MDD) is proposed, in which recorded experimental data is post-processed to remove the scattering imprint related to the domain boundary, such that the Green's functions associated with a scattering object of interest are obtained. The MDD method works with linear and time-invariant media. Similar to [30], a recording surface is required, which needs to satisfy the spatial Nyquist criterion. The source distribution does not need to satisfy the Nyquist criterion but needs to illuminate the medium inside the recording surface from all directions. The extrapolation of the waves in the method with IBCs of [30] needs to happen in real-time during a physical experiment, which is computationally expensive. On the other hand, MDD is significantly simpler to operate than an active system, since it is carried out after the physical experiment [80]. This method could also be used to obtain the Green's function of the reflected sound field. With the Green's function of the reflected sound field the translation from the total acoustic sound field to the reflected acoustic sound field can be made, which can be implemented with an ANC system. However, the inverse problem is ill-posed, which could result in distorted waveforms due to inversion errors.

1.5 Active control in an acoustic anechoic chamber

This section describes previous related work dedicated to the extension of the operable frequency range in AACs by implementation of active systems. In [81] an active sound absorber with a porous plate is presented. The active part has a role of realizing the zero pressure termination of the porous plate, by matching the flow resistance to the characteristic impedance of air. In [82, 83] so-called hybrid absorbers are studied. The term hybrid refers to the combination of passive absorbing materials and an active component. The absorption material is placed at a distance from a movable wall, leaving an air space. The control system matches the back surface impedance of the absorption layer to the characteristic impedance of air. The result is an impedance matching technique to minimize the reflected wave from the absorption layer. In [75] the active control of acoustic reflection, absorption and transmission using thin panel speakers is shown. The panels are controlled electronically, which allows the provision of surfaces with desired reflection coefficients. In [84] the active control of wall impedance is proposed and demonstrated with an experiment in a one-dimensional cavity, which is shown to give the same optimal performance as classical feedforward schemes. However, all previously mentioned experiments have been conducted in a plane-wave field with a normal incidence angle. Furthermore, the absorption coefficient estimated in plane-wave field conditions might not be as representative of actual absorption performance inside a room [85]. Therefore,

a study has considered the influence of the incidence angle as well [86], although this needs further development to work with broadband excitation. The method of active impedance control in a three-dimensional volume is shown in [87], but does not offer global sound pressure level reduction for broadband excitations. The benefit of local absorbing conditions is that the information of the diffracted sound field is not required. However, although these methods have achieved locally reacting absorbing conditions, this does not achieve a true anechoic condition, as shown in [87, 88]. Therefore, methods that take a non-local boundary condition into account have been presented. In [78] a simulation of active control in an AAC is presented, but the verification on an experimental setup has not yet been shown. A physical approach to expanding a finite-size laboratory with a virtual domain using active boundary control is shown in [30]. An experiment with a one-dimensional tube is shown, in which a reduction of 95% of the reflected energy in a frequency range from $0.6 - 5.6$ kHz is achieved. This approach utilizes IBC's, which have also been extended to cloaking and holography [89] and elastic immersive wave experimentations [90, 91]. However, the IBC method relies on ideal sources and sensors, in which frequency dependence and directionality are not considered. This requires a calibration solution, which has not yet been shown. An approach to remove the imprint of the domain boundary from the measurements with the MDD method is shown in [80]. The MDD method can transform recorded data contaminated with the imprint of the domain boundary to the Green's functions that are only related to the interior scatterer(s). Conversely, it is also possible to obtain the scattering wave field due to the enclosed volume. The MDD method is carried out after the experiment with post-processing. However, it requires a recording surface with microphones that satisfy the spatial Nyquist criterion, and it requires a source distribution. It is mentioned that, theoretically, a movable source and movable receiver would allow the use of a single source-receiver pair, but this has not been verified. The MDD method solves a Fredholm integral of the first kind, which for a single source recording is highly ill-conditioned. It is therefore suggested that multiple sources are used that illuminate the medium inside the recording surface from all directions. Nevertheless, the inverse problem is still ill-posed: it is also affected by the number of sources and the frequency bandwidths and needs regularization. Due to the ill-posedness the inverted waveforms could be distorted due to inversion errors. In [76] the real-time active suppression of scattered acoustic radiation is presented and in [77] active control of scattered acoustic radiation for a three-dimensional object is shown. It was found that the performance of the active control system is limited by the number of channels that are manageable. In general, control strategies are limited to relatively low frequencies, because, in many applications, the number of control sources required to achieve accurate secondary field generation increases as the wavelength becomes smaller [92]. Therefore, it is necessary to be able to increase the number of sources and sensors of an ANC system, for which algorithms with reduced computational complexity and memory consumption are needed to compute the filter coefficients.

1.6 Problem definition

In this section the problem is defined. The problem is separated into the description of the AAC, which suffers from low-frequency acoustic reflections, and the control architecture which is the technique considered to suppress the acoustic reflections.

1.6.1 The acoustic anechoic chamber

Existing AAC's suffer from low-frequency reflections of up to 200 Hz [18,31,32], due to limitations of the passive absorption material. If the sound wave encounters the absorption material and is not perfectly absorbed, this results in the generation of a secondary wave field. The secondary wave field is superimposed upon the original incident field and creates interference and modification of the pressure and intensity distributions. The processes of the secondary wave field generation are broadly classified as scattering, diffraction and reflection [93]. The scattering of acoustic waves is defined as: "A way by which obstacles or medium fluctuations of small dimensions can modify acoustic wave propagation in the medium" [94]. Furthermore diffraction is defined as: "The capacity of sound waves to bend at the edge of a barrier" [95]. The terms scattering and diffraction are often used interchangeably. Scattering is a broader term, however. For example, scattering from a rough surface may not involve diffraction [96]. Lastly, reflection is defined as: "the result of the constructive interference of many scattered or diffracted waves originating from scatterers in a stratified medium" [97]. In this thesis the term reflected sound field is used, which describes all the sound waves that are reflected from the walls. Hence, the inward traveling sound waves originating from the boundaries of the AAC are considered. In order to employ an ANC system to suppress the reflections, the reflected sound field needs to be known, which is one of the problems studied in this thesis.

1.6.2 The control architecture

To suppress the low-frequency reflections in an AAC a centralized multichannel fixed-gain feedforward ANC system is considered. However, in order to obtain satisfactory performance, the number of sources and sensors should increase for smaller wavelengths and increasing geometry sizes [47, 50, 76, 77]. The increase in sources and sensors leads to higher computational complexity and memory consumption. Therefore, algorithms with reduced computational complexity and memory consumption are needed. The algorithms operate by having a system model of the response of the system. The system is modelled with digital filters, which in this thesis are FIR filters. Reasons for this choice are that 1) an FIR filter is always stable, while an IIR filter is not necessarily stable [44, 60] and may be more susceptible to suffer from numerical instability issues [61], and 2) the use of state-space models requires an accurate MIMO state-space model, which can be difficult to obtain [53]. Furthermore, the use of the FIR descriptions allows for relatively straightforward extension, conversion and improvement of most existing algorithms. The goal of this approach is a solution strategy to compute the control coefficients for a control system, which is scalable to any specific AAC with varying dimensions and require-

ments, to suppress the low-frequency reflections and therefore extend the operable frequency range of the AAC.

1.6.3 Basic assumptions

In this thesis the following assumptions are made on the systems and signals considered:

1. **Stochastic, stationary and broadband disturbances** are generated by the object to be studied, located in the middle of the AAC. The disturbance signal is assumed to be a random noise process, which is stationary in time [44]. The term broadband refers to the power spectrum, meaning that the power of the disturbance signal is distributed over a particular bandwidth.

2. **Linear time invariant dynamic systems** are assumed, which includes the fluid whose behaviour is assumed to be linear, inviscid, adiabatic and homogeneous. Under these assumptions, acoustic waves in enclosures can be described by partial differential equations. Furthermore, the sources and sensors can be considered linear as long as the voltages and amplitudes stay relatively low. Due to the linearity assumption, the systems involved are assumed to obey the superposition principle. Lastly, the systems are assumed to be time invariant, which means that the system function is not a direct function of time.

3. **An upstream correlated reference signal is available**, obtained with reference sensors, which allows for feedforward control architectures to be applied.

4. **Microphones are preferred**, although more advanced sensors are available, for example acoustic vector sensors [98] and particle velocity sensors [99]. Furthermore, particle image velocimetry [100] is an optical measurement technique which allows the particle velocity to be obtained.

1.7 Research objectives

Following the literature review and problem definition, the research objectives are defined as follows:

To develop a technique to compute the reflected sound field such that active control can be applied to suppress the reflections from the walls. In order to design a control system with the objective of suppressing reflected sound waves from the walls, an accurate estimation of the reflected sound field must be obtained in real-time. Ideally, this technique should allow the use of pressure microphones, which reduces the cost of the system and allows for easy calibration procedures.

To develop an efficient method to compute a set of causal fixed-gain FIR control coefficients, which allows the control of large-scale systems with large numbers of sources and sensors. As found in the literature, to effectively apply ANC for increasing geometry sizes and decreasing wavelengths, the required number of sources and sensors increases.

To implement an offline active technique to suppress reflections from the walls in a numerical study, and verify its effectiveness. Numerical studies allow for

scaled-up system sizes with up to hundreds of sources and sensors, which at this stage cannot feasibly be tested in real-time.

To implement a real-time active technique to suppress reflections from the walls. Although a numerical study of the developed techniques is able to show the effectiveness, this relies on the mathematical models and typically simulates ideal circumstances, without sensor noise, hardware constraints or environmental influences. Therefore, the developed techniques should be implemented on a real-time system to show the effectiveness and performance to suppress the acoustic reflections from the walls.

1.8 Research achievements

The contributions of this thesis are listed under methodological achievements or implementation related achievements.

1.8.1 Methodological achievements

A technique to compute the reflected sound field is developed, which evaluates the Kirchhoff-Helmholtz integral (KHI). The method requires the particle velocity and acoustic pressure on a contour, which makes it possible to compute the reflected sound field within the contour due to sources positioned within the contour. The particle velocity is estimated with microphones positioned in radial outward direction (Chapter 3).

An iterative least mean squares (LMS) algorithm is developed, in which preconditioning and prewhitening filters are applied to improve convergence speed. These filters are derived in the frequency domain and delayed in the time domain to ensure causality (Sec. 4.2).

A preconditioned conjugate gradient time domain algorithm is improved, with the addition of regularization. The regularization is needed to maintain control stability in systems with internal model control, and therefore allows practical implementation in an AAC to suppress the reflections (Sec. 4.3).

A causally constrained frequency domain conjugate gradient algorithm is developed, which, due to the frequency domain computations, offers low computational complexity and memory consumption, while being causally constrained to compute causal filter coefficients (Sec. 4.4).

1.8.2 Implementation related achievements

The KHI method is verified with a numerical study, by comparing the results computed with the finite element method, to show 1) that the output of the KHI within the contour for a source inside the contour is the reflected sound field, 2) that the output of the KHI within the contour for a source outside the contour is the total sound field, 3) the error introduced by the particle velocity estimation and 4) the error introduced by noise at certain microphones on the contour. (Sec. 5.2).

The iterative LMS algorithm is applied in a numerical study, together with the KHI, with the objective of suppressing the reflections from the walls. The system configuration is based on the experimental setup (Sec. 5.3).

The causally constrained frequency domain CG algorithm is applied in a numerical study, together with the KHI, with the objective of suppressing reflections from the walls using a large-scale ANC system (Sec. 5.4).

Real-time implementations on a small-scale experimental setup are shown, in which the efficient PCG time domain algorithm is applied together with the KHI method in Sec. 6.3. The same implementation is shown using the causally constrained frequency domain CG algorithm together with the KHI method in Sec. 6.4. The results of both implementations show that the reverberation time has effectively been reduced.

1.9 Outline of the thesis

With reference to Fig. 1.4, the outline of the thesis is as follows. In Chapter 2 the description of the physics and algorithms for ANC are given. The first part describes the fundamental equations for acoustics, and the second part describes algorithms for ANC. In Chapter 3 the method of computing the reflected sound field due to the primary sources is derived. In Chapter 4 three different algorithms are derived, starting with the derivation of the FD-RMFE algorithm in Sec. 4.2, followed by the derivation of the PBC-CG algorithm in Sec. 4.3 and lastly in Sec. 4.4 the CC-CG algorithm is derived. In Chapter 5 the numerical studies are shown. The method of computing the reflected sound field is verified in Sec. 5.2. A numerical study to suppress the reflections from the walls involving the method to compute the reflected sound field and the FD-RMFE algorithm is shown in Sec. 5.3. A numerical study to suppress the reflections from the walls with a large-scale system involving the method to compute the reflected sound field and the CC-CG algorithm is shown in Sec. 5.4. A small-scale setup is built, which is used to verify the developed methods in real-time. A real-time experiment in which the control coefficients are computed with the PBC-CG algorithm is shown in Sec. 6.3, and in which the control coefficients are computed with the CC-CG algorithm is shown in Sec. 6.4. The conclusions are given in Chapter. 7.

The outline of the appendices is as follows. In Appendix A.1 an example is given on how to compute the reflected sound field with the finite element method, which allows for comparison with the output of the KHI due to the primary sources in Ch. 5. In Appendix A.2 the calibration procedure for the microphones is shown. In Appendix A.3 the electrical scheme of the microphone pre-amplifiers is shown. Lastly, in Appendix A.4 the FRFs of all involved transfer paths of the experimental setup are shown.

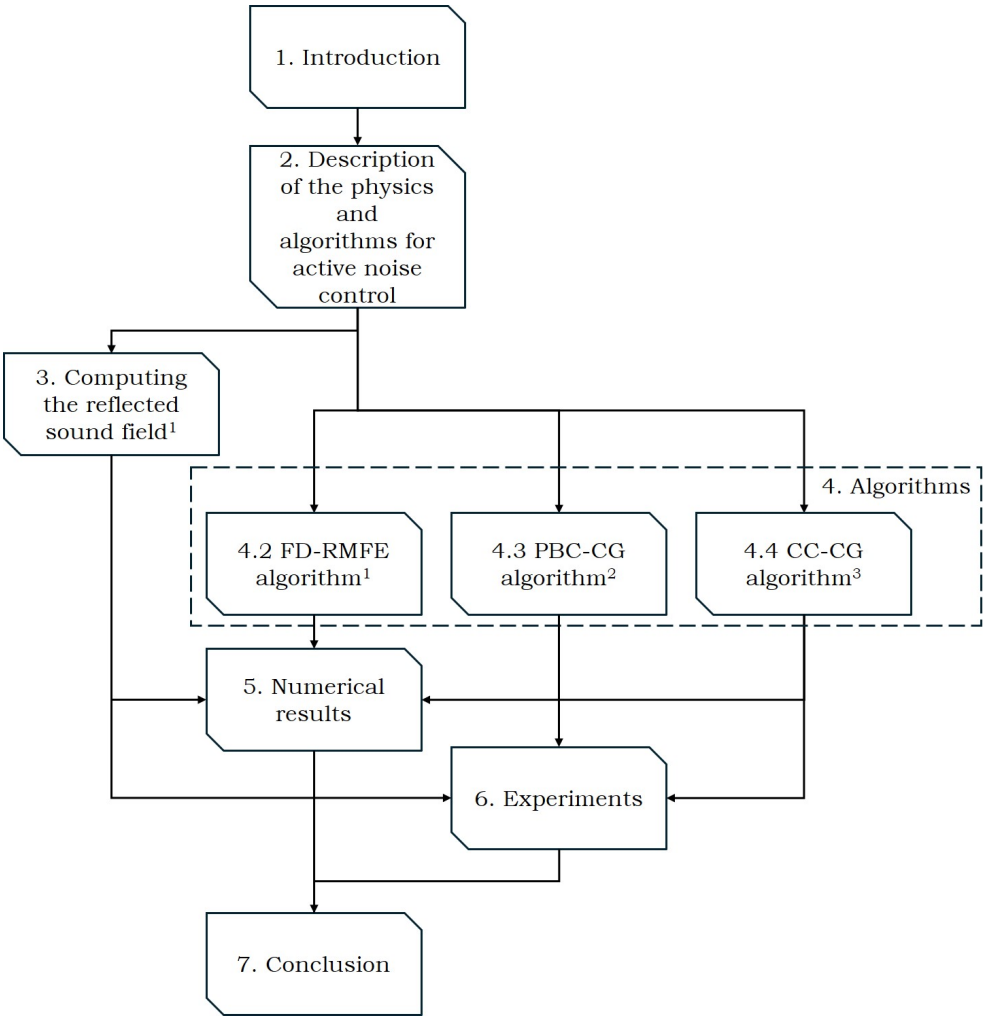

Figure 1.4: Dependencies among the chapters in this thesis.

[1] R. Haasjes and A.P. Berkhoff. An efficient offline scheme to compute an FIR controller for active reduction of acoustic reflections in an anechoic chamber. *Journal of Sound and Vibration*, **573**:118198, 2024.
[2] R. Haasjes and A.P. Berkhoff. A small-scale active anechoic chamber. *Applied Acoustics*, **224**:110130, 2024.
[3] R. Haasjes and A.P. Berkhoff. A solution method for active suppression of reflections in anechoic chambers. *The Journal of the Acoustical Society of America*, 2024, submitted.

Chapter 2

Description of the physics and algorithms for active noise control

This introductory chapter describes the existing physics and existing active noise control algorithms for acoustic applications, which are the basis for the methods and algorithms derived in this thesis. To employ an ANC system to suppress the acoustic reflections in the AAC, the reflected sound field needs to be known. The first part of this chapter is dedicated to the description of the fundamental equations for acoustics in Sec. 2.1, which is relevant for the computation of the reflected sound field. The second part of this chapter describes the existing algorithms and modelling strategies for ANC in Sec. 2.2. These algorithms and modelling strategies are the basis of the derivation of the algorithms with reduced computational complexity in this thesis.

2.1 Fundamental equations for acoustics

The AAC considered in this thesis is schematically shown in two dimensions in Fig. 2.1. The chamber could be of any dimensions, but is typically in the order of several metres in each dimension, see for example [31, 32]. It is assumed that at all the boundaries of the AAC, including the floor and the roof, absorption material is applied, which in the figure is drawn as a wedge, because this was found to be the best performing shape [18]. Furthermore, it is assumed that the object to be studied, is positioned in the middle of the AAC, indicated with the circle. The object to be studied in the AAC is assumed to generate noise with a spectral content of anywhere up to 20 kHz. As mentioned in the literature, the thickness of the absorption material is related to the wavelength of the acoustic waves. Therefore, with longer wavelengths (and thus lower frequencies), the performance of the absorption material at the boundaries of the AAC deteriorates, and the sound wave is not perfectly absorbed. The non-perfect absorption of the lower frequency sound waves results in low-frequency reflections. For an ANC system to suppress these reflections, the reflected sound field needs to be known. Therefore, this section describes the funda-

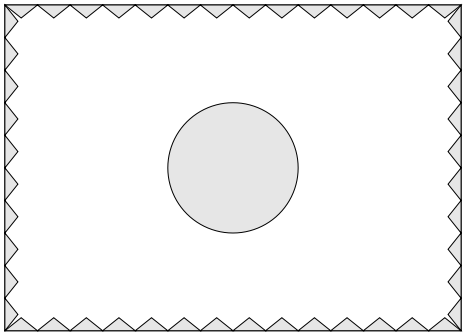

Figure 2.1: Two-dimensional configuration of a typical acoustic anechoic chamber, with wedges at its boundaries, and the object to be studied to be positioned anywhere in the circle.

mental equations for acoustics, which introduce the relevant physics, equations, assumptions and boundary conditions. With these fundamental equations for acoustics, the KHI is derived in the next chapter, which is used to compute the reflected sound field. The description of the physics starts with the acoustic wave equation.

2.1.1 The acoustic wave equation

Acoustic disturbances can usually be regarded as small-amplitude perturbations to an ambient state $(p_0, \rho_0, \mathbf{v}_0)$, which are the ambient pressure, density and particle velocity, respectively. With a disturbance present, this can be written as

$$p = p_0 + p', \quad \rho = \rho_0 + \rho', \tag{2.1}$$

in which p' and ρ' denote the pressure and density perturbations [101], respectively. Because it is assumed that the density and particle velocity fluctuations are small in comparison with the ambient state, the use of a linear approximation of the mass conservation and momentum equation is valid. Throughout this thesis it is assumed that the behaviour of the fluid is linear, inviscid and adiabatic and that body forces do not influence the dynamic behaviour. In specific cases these assumptions do not hold: for example, a sound wave can become non-linear when relatively high sound pressure levels are reached. Also, loudspeaker dynamics can become non-linear with relatively high driving signal amplitudes. These limitations of the assumptions should be considered while implementing the control system. By neglecting the second- and higher-order terms, the acoustic approximation to the linearized inhomogeneous equation of mass conservation [101] is written as

$$\frac{\partial \rho'}{\partial t} + \rho_0 \nabla \mathbf{v}' = q, \tag{2.2}$$

where ∇ denotes the gradient operator, $\mathbf{v}'$ denotes the perturbation of the particle velocity and q represents the rate at which mass is added to the medium [101]. Similarly, by neglecting the second- and higher-order terms, the acoustic approximation to the linearized inhomogeneous momentum equation [101] is formulated as

$$\rho_0 \frac{\partial \mathbf{v}'}{\partial t} + \nabla p' = \mathbf{f}, \tag{2.3}$$

in which $\mathbf{f}$ represents any external forces, for example body forces like gravity. The equation to describe the behaviour of acoustic waves is called the wave equation [96]. In order to obtain the homogeneous wave equation, it is assumed that no mass is being added or removed ($q = 0$) and that there are no external forces ($\mathbf{f} = 0$) acting on the fluid. For an isentropic process, the linearized relation $p' = c^2\rho'$ holds [96]. In [101,102] is shown that with the mass conservation equation, the divergence applied to the momentum equation and by using the relation $p' = c^2\rho'$ the homogeneous wave equation is obtained

$$\nabla^2 p(\mathbf{x}, t) - \frac{1}{c^2} \frac{\partial^2 p(\mathbf{x}, t)}{\partial t^2} = 0, \tag{2.4}$$

in which $p(\mathbf{x}, t)$ replaces p' and denotes the acoustic pressure at position $\mathbf{x}$ and time t. Furthermore, in this equation ∇^2 is the Laplace operator and c denotes the speed of sound in the medium. A typical value for the speed of sound in air at 20°C is 343 m/s. Similar to the acoustic pressure $p(\mathbf{x}, t)$, the prime of $\mathbf{v}'$ is dropped and the particle velocity is denoted by $\mathbf{v}(\mathbf{x}, t)$. The density of the acoustic medium is denoted by ρ. Given a time domain signal like the acoustic pressure $p(\mathbf{x}, t)$, the frequency domain version of this signal is written as

$$p(\mathbf{x}, \omega) = \mathcal{F}(p(\mathbf{x}, t)) = \int_{-\infty}^{\infty} p(\mathbf{x}, t) \mathrm{e}^{-\mathrm{j}\omega t} \mathrm{d}t, \tag{2.5}$$

in which $\mathcal{F}(\cdot)$ stands for the Fourier transform [103], $\omega = 2\pi f$ is the angular frequency, f is the frequency in Hz and $\mathrm{j} = \sqrt{-1}$ denotes the imaginary number. The frequency domain representation allows analysis of how the content of the signal is distributed within the frequency spectrum. Furthermore, in certain cases equations can be more straightforward or computationally less expensive to solve in the frequency domain than the time domain. An example is an equation that contains an integral over time. Frequency domain representations are typically complex-valued, consisting of both the magnitude and the phase of a set of sinusoids at each considered frequency. With the frequency domain representation, the inverse Fourier transform $\mathcal{F}^{-1}(\cdot)$ is used to return to the time domain

$$p(\mathbf{x}, t) = \mathcal{F}^{-1}(p(\mathbf{x}, \omega)) = \frac{1}{2\pi} \int_{-\infty}^{\infty} p(\mathbf{x}, \omega) \mathrm{e}^{\mathrm{j}\omega t} \mathrm{d}\omega. \tag{2.6}$$

Substitution of the last relation into the wave equation in Eq. (2.4), and computing the Fourier transform of the wave equation, the Helmholtz equation [104] is obtained

$$\nabla^2 p(\mathbf{x}, \omega) + k^2 p(\mathbf{x}, \omega) = 0, \tag{2.7}$$

in which $k = \omega/c$ is the wavenumber, which is dependent on the frequency. A variable that is also dependent on the frequency is the wavelength, defined as

$$\lambda = \frac{c}{f}, \tag{2.8}$$

which shows that the wavelength is inversely proportional to the frequency. Next to the acoustic pressure, another important quantity related to sound waves is the particle velocity $\mathbf{v}(\mathbf{x}, t)$, which describes the velocity of the fluid particles as they move back and forth as the sound wave propagates. The acoustic pressure and the particle velocity are related through the homogeneous linearized momentum equation in Eq. (2.3) with $\mathbf{f} = 0$, which is written as

$$\rho \frac{\partial \mathbf{v}(\mathbf{x}, t)}{\partial t} + \nabla p(\mathbf{x}, t) = 0. \tag{2.9}$$

This equation can be solved for the particle velocity by computing the integral

$$\mathbf{v}(\mathbf{x}, t) = -\frac{1}{\rho} \int \nabla p(\mathbf{x}, t) \mathrm{d}t. \tag{2.10}$$

This integral is an example of an equation that is more straightforward to solve in the frequency domain, in which case the equation is written as

$$\mathbf{v}(\mathbf{x}, \omega) = \frac{\mathrm{j}}{\rho\omega} \nabla p(\mathbf{x}, \omega), \tag{2.11}$$

which is obtained by taking the Fourier transform of Eq. (2.10). The wave equation (Eq. (2.4)) and the Helmholtz equation (Eq. (2.7)) are defined without a source term, because until now $q = 0$ in Eq. (2.2) and $\mathbf{f} = 0$ in Eq. (2.3) were assumed. The object to be studied in the AAC will generate sound so that this object can be seen as a source or external force, depending on the object. Adding a point mass source at location $\mathbf{x}_0$ with a volume rate of strength Q_s in m^3/s, appears on the right-hand side of Eq. (2.2) by writing $q = \rho \frac{\partial Q_s(t)}{\partial t} \delta(\mathbf{x} - \mathbf{x}_0)$. Similarly, by writing $\mathbf{f} = \mathbf{F}(t)\delta(\mathbf{x} - \mathbf{x}_0)$ a force $\mathbf{F}(t)$ is added on the right-hand side of Eq. (2.3). The derivation of the inhomogeneous wave equation is then similar to the homogeneous case as in shown in [101], with the inhomogeneous mass conservation equation, the divergence applied to the inhomogeneous momentum equation and the relation $p' = c^2 \rho'$, written as

$$\nabla^2 p(\mathbf{x}, t) - \frac{1}{c^2} \frac{\partial^2 p(\mathbf{x}, t)}{\partial t^2} = \nabla \cdot (\mathbf{F}(t)\delta(\mathbf{x} - \mathbf{x}_0)) - \rho \frac{\partial Q_s(t)}{\partial t} \delta(\mathbf{x} - \mathbf{x}_0), \tag{2.12}$$

in which δ is the Dirac delta function, for which $\int_{-\infty}^{\infty} \delta(t) dt = 1$. The addition of the point mass source and the external force on the fluid result in the inhomogeneous Helmholtz equation [101], written as

$$\nabla^2 p(\mathbf{x}, \omega) + k^2 p(\mathbf{x}, \omega) = \mathbf{F}(\omega) \cdot \nabla \delta(\mathbf{x} - \mathbf{x}_0) + \mathrm{j}\omega\rho Q_s(\omega) \delta(\mathbf{x} - \mathbf{x}_0), \tag{2.13}$$

in which $\mathbf{F}(\omega)$ and $Q_s(\omega)$ are the Fourier transform of the time-varying forces and sources $\mathbf{F}(t)$ and $Q_s(t)$, respectively. Several types of sources and their mathematical

descriptions can be found in [96, 101, 102]. The wave equation and the Helmholtz equation do not inherently include any type of boundary conditions. In the case of a bounded domain, the Dirichlet boundary condition, the Neumann boundary condition and the Robin boundary condition are examples that can be applied. In the case of an unbounded domain, a boundary condition is applied at infinity, called the Sommerfeld radiation condition [105], defined as

$$\lim_{r\to\infty} r^{\frac{h-1}{2}} \left(\frac{\partial p}{\partial r} - \mathrm{j}kp \right) = 0, \tag{2.14}$$

in which r denotes the radial distance starting from a harmonic source, and h denotes the number of dimensions. This condition requires that as r approaches infinity, only outgoing waves can exist and that no waves are allowed to travel from infinity to the domain.

In acoustics, the range of signal amplitudes is very large. Therefore, a logarithmic scale is very common in acoustics to compress this range. The logarithmic measure is called a level. Although levels are unitless, they are expressed in decibels (dB), which is widely used throughout this thesis. The most widely used level is the sound pressure level (SPL) [106], which is a measure of the root mean square pressure of a sound (p_{rms}), defined as

$$\mathrm{SPL} = 20\log_{10}\left(\frac{p_{\mathrm{rms}}}{p_{\mathrm{ref}}} \right), \tag{2.15}$$

in which p_{ref} is the reference pressure. Next to the SPL, also the intensity level and the sound power level are used in acoustics [96].

2.1.2 Green's functions

The solution to the inhomogenous Helmholtz equation is typically dealt with by the use of a Green's function [60]. A Green's function describes the complex pressure field produced by a harmonic point monopole source for given acoustic boundary conditions. The Green's function is a solution of the inhomogenous equation [107], written as:

$$(\nabla^2 + k^2) G(\mathbf{x}|\mathbf{x}_0, \omega) = -\delta(\mathbf{x} - \mathbf{x}_0), \tag{2.16}$$

in which $G(\mathbf{x}|\mathbf{x}_0, \omega)$ is the Green's function, where the first argument denotes the location of the listener, and the second argument denotes the location of the source. A universal property of the Green's functions is the reciprocity relation $G(\mathbf{x}|\mathbf{x}_0, \omega) = G(\mathbf{x}_0|\mathbf{x}, \omega)$, so G does not change, while source and listener positions are interchanged [101]. If the medium external to the source is unbounded, with the Sommerfeld boundary condition at infinity, G is identified as the free-space Green's function. The forward Green's function in a three-dimensional space, so that any position is described with three degrees of freedom $\mathbf{x} = \{x, y, z\}$, is written as:

$$G(\mathbf{x}|\mathbf{x}_0, \omega) = \frac{\mathrm{e}^{-\mathrm{j}kR}}{4\pi R}, \tag{2.17}$$

in which $R = \|\mathbf{x} - \mathbf{x}_0\|$ and the term $\mathrm{e}^{-\mathrm{j}kR}$ represents a forward propagation [108].

In a two-dimensional space, which means that any position is described with two degrees of freedom $\mathbf{x} = \{x, y\}$, the Green's function can be interpreted as the field due to a line source at $\mathbf{x_0}$. The Green's function can be derived by integrating the three-dimensional Green's function along one dimension [109], resulting in

$$G(\mathbf{x}|\mathbf{x}_0, \omega) = -\frac{\mathrm{j}}{4} H_0^{(2)}(kR), \tag{2.18}$$

in which $H_a^{(b)}$ is the Hankel function of kind b and order a [110]. In cases of multiple point sources, the Green's functions follow the superposition principle. Thus, with N point sources, the pressure amplitude satisfies the Helmholtz equation in Eq. (2.7) as a linear combination [101], written as:

$$p(\mathbf{x}, \omega) = \sum_{n=1}^{N} \hat{S}_n G(\mathbf{x}|\mathbf{x}_0, \omega), \tag{2.19}$$

in which $\hat{S}_n$ is the source strength of the corresponding source n.

2.1.3 Reverberation time

At this point the relevant physics, equations, assumptions and boundary conditions are introduced to derive the KHI, which is used to compute the reflected sound field. However, with the objective of removing the reflections in an AAC, a measure to indicate whether the reflections are being suppressed is necessary. One of the possibilities is to compute the reverberation time (RT). The RT defines the time required for the SPL to decrease after the source of sound has stopped. Typically the RT is denoted by T60, which represents the time measure by which the SPL has decreased by 60 dB. The reflections increase the reverberation time, due to the sound waves that keep bouncing between reflectors. So, by suppressing the reflections, the RT should decrease. For an empty room, the RT is predictable using Sabine's equation [101], written as:

$$T60 = \frac{0.161V}{\sum_i \alpha_i A_i}, \tag{2.20}$$

in which V is the volume of the room, A_i is the area of element i, characterized by an absorption coefficient α_i. The equation shows that the RT increases with the room dimensions, and decreases with the amount and quality of the absorption. A method to estimate the RT from a room's impulse response is with the Schroeder integration method [111], also known as reversed time integration.

With the RT to determine the effectiveness of suppressing the reflections, the relevant physics to compute the reflected sound field and to measure the effectiveness are described. The next section describes the algorithms and modelling strategies for ANC, which is the basis for the algorithms derived in this thesis.

2.2 Algorithms for active noise control

Once the reflected sound field is known, the goal of the ANC system is to suppress the low-frequency reflections that are present in an AAC. The ANC system should

complement the passive absorption, which takes care of the medium to high frequency range. The object to be studied in the AAC is represented by a set of primary sources, which generate stationary and ergodic noise from the middle of the chamber, anywhere in the indicated circle of Fig. 2.1. Although it is assumed that the object to be studied generates noise with a spectral content of anywhere up to 20 kHz, the medium to high frequencies are taken care of by the passive absorption. As found in literature, typical AAC's have a cut off frequency at about 200 Hz [18,31,32]. Therefore, the ANC system should be able to take care of the lower frequency reflections of up to about 200 Hz. To ensure overlap in the frequency range between the passive absorption and the ANC system, however, this upper frequency limit is ideally increased to about 600 Hz. In order to obtain satisfactory performance, the number of sources and sensors of the ANC system should be increased for smaller wavelengths and larger geometries [47, 50, 76, 77]. However, with larger number of sources and sensors, both the computational complexity and the memory consumption increases, so algorithms with reduced computational complexity and memory consumption to compute the set of filter coefficients for large systems are needed. In this section the existing algorithms, properties and modelling strategies for ANC are introduced; this is the basis for the derivation of the algorithms with reduced computational complexity and memory consumption in this thesis.

The variables in the previous section were functions of a continuous time variable t, while in this section the time variable is assumed to be discrete and to represent the sampled version of the physical signals from the previous section. To design a control system to suppress the reflections in an AAC, a mathematical model of every transfer path involved is required. The object to be studied in the AAC is considered as a combination of primary sources. In this case the transfer paths need to be modelled, such as the primary path from the primary sources to the error sensors, the secondary path from the secondary sources to the error sensors, the feedback path from the secondary sources to the reference sensors, and the set of filter coefficients that generate the control signals from the reference signals.

A general system can be written as a discrete-time state-space system [62], following

$$\begin{aligned} \mathbf{x}(n+1) &= f(n, \mathbf{x}(n), \mathbf{u}(n)), \\ \mathbf{y}(n) &= h(n, \mathbf{x}(n), \mathbf{u}(n)), \end{aligned} \tag{2.21}$$

in which n denotes the sample moment, $\mathbf{u}(n) \in \mathbb{R}^{\mathcal{M}\times 1}$ is the vector of $\mathcal{M}$ input signals, $\mathbf{y}(n) \in \mathbb{R}^{\mathcal{L}\times 1}$ is the vector of $\mathcal{L}$ output signals and $\mathbf{x}(n) \in \mathbb{R}^{\mathcal{S}\times 1}$ is a vector with the $\mathcal{S}$ states of the system. Two examples are given to describe the primary and secondary paths. In the case of the primary path, $\mathbf{u}(n)$ are the driving signals of the primary sources and $\mathbf{y}(n)$ are the disturbance signals measured at the error microphones. Similarly, in the case of the secondary path, $\mathbf{u}(n)$ are the driving signals of the secondary sources and $\mathbf{y}(n)$ are the secondary signals measured at the error microphones. In both cases $\mathbf{x}(n)$ are the state variables that describe the internal dynamics.

The relations between these variables are described by the functions f and h, which are dependent on the sample moment. By assuming time-invariant systems

[62], this is written as

$$\begin{aligned} \mathbf{x}(n+1) &= f(\mathbf{x}(n), \mathbf{u}(n)), \\ \mathbf{y}(n) &= h(\mathbf{x}(n), \mathbf{u}(n)), \end{aligned} \tag{2.22}$$

so that the functions f and h are not a function of time. Then, by assuming that the functions f and h are linear with respect to $\mathbf{x}(n)$ and $\mathbf{u}(n)$ [62, 67], the system obeys the superposition principle [44], and can therefore be written as

$$\begin{aligned} \mathbf{x}(n+1) &= \boldsymbol{A}\mathbf{x}(n) + \boldsymbol{B}\mathbf{u}(n), \\ \mathbf{y}(n) &= \boldsymbol{C}\mathbf{x}(n) + \boldsymbol{D}\mathbf{u}(n). \end{aligned} \tag{2.23}$$

This is a description of a linear time-invariant (LTI) system [112] in state-space form, with $\boldsymbol{A} \in \mathbb{R}^{\mathcal{S}\times\mathcal{S}}$, $\boldsymbol{B} \in \mathbb{R}^{\mathcal{S}\times\mathcal{M}}$, $\boldsymbol{C} \in \mathbb{R}^{\mathcal{L}\times\mathcal{S}}$ and $\boldsymbol{D} \in \mathbb{R}^{\mathcal{L}\times\mathcal{M}}$. Throughout this thesis linearity and time-invariance are assumed for all the systems and signals involved. While state-space models offer a powerful framework, a subspace model identification method to obtain an accurate description of the model is required. This state-space model can be difficult to obtain [53], especially for MIMO acoustic systems which yield high-order models [113]. High-order models are more difficult to use for control design [114] and also require more computational resources for real-time applications [115]. Besides the state-space formulation, an LTI system can be represented in different forms [114]. The first part of Eq. (2.23) can be written as

$$\mathbf{x}(n+1) = q\mathbf{x}(n) = \boldsymbol{A}\mathbf{x}(n) + \boldsymbol{B}\mathbf{u}(n), \tag{2.24}$$

in which q is the forward shift operator[1]. If the operator $[q\boldsymbol{I} - \boldsymbol{A}]$ is boundedly invertible [62], then the previous equation can be written as

$$\mathbf{x}(n) = (q\boldsymbol{I} - \boldsymbol{A})^{-1}\boldsymbol{B}\mathbf{u}(n), \tag{2.25}$$

where $\boldsymbol{I} \in \mathbb{R}^{\mathcal{S}\times\mathcal{S}}$ is an identity matrix. By expanding Eq. (2.25) into an infinite series as shown in [62], the digital filter

$$\mathbf{y}(n) = \sum_{i=0}^{\infty} \boldsymbol{h}(i)\mathbf{u}(n-i), \tag{2.26}$$

is obtained, where $\boldsymbol{h} \in \mathbb{R}^{\mathcal{L}\times\mathcal{M}}$ is the matrix of impulse responses of the system [62, 67], denoted by

$$\boldsymbol{h}(n) = \begin{cases} \boldsymbol{0}, & n < 0, \\ \boldsymbol{D}, & n = 0, \\ \boldsymbol{C}\boldsymbol{A}^{n-1}\boldsymbol{B}, & n > 0, \end{cases} \tag{2.27}$$

which could also be found by applying impulse inputs to Eq. (2.23) following [67]. The impulse response of the digital filter is causal, because $\boldsymbol{h}(n) = 0$ for $n < 0$. If the impulse response decays to zero within finite time, the system is called a finite impulse response (FIR) system, otherwise it is called an infinite impulse response (IIR)

[1] q denotes the forward shift operator. The operator q^{-1} corresponds to the delay of 1 sample, which can be written as $q^{-1}x(n) = x(n-1)$.

system. In digital signal processing, the recursive IIR filter and the non-recursive FIR filter are common modelling approaches [44,116]. IIR filters are most appropriate for lightly damped structural systems due to their efficiency with fewer coefficients [44]. However, they can suffer from parasitic oscillations, although these can be mitigated by using wave digital filters [117] and certain state-space structures [118]. On the other hand, FIR filters have poles only at zero [44], ensuring stability as long as the coefficients are bounded [60]. Furthermore, in practice, FIR filter coefficients can be easier to identify than those of IIR filters [44]. However, FIR filters typically require higher orders than IIR filters to achieve the same level of accuracy. Despite this, high-order FIR filters can be efficiently implemented using the fast fourier transform (FFT) [118]. In general, the number of coefficients in an FIR filter decrease with an increase in the amount of damping in the system [44]. Nevertheless, as found in the works of [119, 120] an FIR model can be just as accurate as an IIR model with a similar number of coefficients in three-dimensional enclosures. This holds true even when the enclosure is not well damped [44]. Furthermore, FIR filters can be efficiently estimated, are robust against noise [114, 121], and typically the FIR filter design formulation is a convex problem [122]. While a Kautz filter [123] is presented as a different modelling approach in situations with for example long reverberation times, in which the use of a FIR filter requires a lot of coefficients, the Kautz filter comes with a higher computational complexity. Therefore, the systems involved in the algorithms derived throughout this thesis are modelled with FIR filters, and the next section gives the description of an FIR filter.

2.2.1 Finite Impulse Response

In order to compute the output of the digital filter in finite time, the expansion in Eq. (2.26) is truncated to I samples, so that the digital filter is written as

$$\mathbf{y}(n) = \sum_{i=0}^{I-1} \boldsymbol{h}_i \mathbf{x}(n-i), \tag{2.28}$$

i.e. a digital filter with a FIR of length I, which is a tapped delay line. The impulse response of the filter is calculated by setting $\mathbf{x}(n) = \delta(n)$, a Kronecker impulse excitation, to obtain:

$$\mathbf{y}(n) = \begin{cases} \boldsymbol{h}_n, & 0 \leq n \leq I-1, \\ \mathbf{0}, & \text{otherwise}, \end{cases} \tag{2.29}$$

in which $\mathbf{y}(n)$ is the impulse response at n. The output of the digital system can be written as

$$\mathbf{y}(n) = \boldsymbol{H}(z)\mathbf{x}(n), \tag{2.30}$$

in which

$$\boldsymbol{H}(z) = \boldsymbol{h}_0 + \boldsymbol{h}_1 z^{-1} + \boldsymbol{h}_2 z^{-2} + , \ldots , + \boldsymbol{h}_{I-1} z^{-I+1}, \tag{2.31}$$

is the transfer function which relates the z-transform[1] of the output sequence to the z-transform of the input sequence. Previously, the operator q was introduced as the

[1]The two-sided z-transform of a sequence $h(n)$ is defined as $H(z) = \sum_{n=-\infty}^{\infty} h(n) z^{-n}$ [60]. The frequency response is obtained by substitution of $z = \mathrm{e}^{\mathrm{j}\omega T}$, in which $\mathrm{j} = \sqrt{-1}$ and ωT is the normalized angular frequency [44].

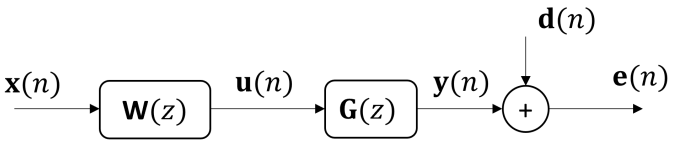

Figure 2.2: Block diagram of a general fixed-gain MIMO feedforward system.

forward shift operator. However, following [44], in the remaining text the operator z denotes the forward shift operator in the time domain signals so as to be consistent with the literature. To accurately represent a system, the number of filter coefficients I should be sufficient for the impulse response to have decayed.

2.2.2 Fixed-gain feedforward control

With the description of an FIR filter, (acoustic) systems can be modelled by measuring the input and output signals of the system involved. Furthermore, an FIR filter can also be specifically designed for certain objectives, which allows the implementation of an ANC system. It is assumed that the object to be studied is placed in the middle of the AAC. This results in an advantageous distance to obtain an upstream reference signal. This reference signal could be obtained from microphones, or acceleration/velocity sensors placed on the object. With an upstream reference signal available, a feedforward control system can be employed. In Fig. 2.2 a block diagram of a general MIMO fixed-gain feedforward control system is shown. In this block diagram, the secondary path from the secondary sources to the error sensors is modelled by an FIR filter $\boldsymbol{G}(z) \in \mathbb{R}^{L\times M}$, in which L denotes the number of error sensors and M denotes the number of secondary sources. The secondary path FIR filter needs to be computed beforehand with an identification procedure using the input and output signals [44]. The control coefficients can be modelled with an FIR filter, denoted by $\boldsymbol{W}(z) \in \mathbb{R}^{M\times K}$, in which K denotes the number of reference signals. Compared to a fixed-gain implementation, an adaptive configuration also incorporates the control filter coefficients update step, which increases the real-time computational complexity. Therefore, it is assumed that the control coefficients have a fixed gain.

The set of control coefficients can be designed in many ways, but in general for ANC, the objective is to suppress the error signal by finding a set of control coefficients which minimize a cost function. From this point, the term controller refers to the control system (i.e. computer) instructed with the set of control coefficients $\boldsymbol{W}(z)$. The objective of the controller is to minimize the error signal $\mathbf{e}(n) = \mathbf{d}(n) + \mathbf{y}(n)$, in which $\mathbf{e}(n) \in \mathbb{R}^{L\times 1}$, $\mathbf{d}(n) \in \mathbb{R}^{L\times 1}$ denotes the disturbance signal and $\mathbf{y}(n) \in \mathbb{R}^{L\times 1}$ denotes the secondary signal. The secondary signal is the control output signal $\mathbf{u}(n) \in \mathbb{R}^{M\times 1}$ filtered by the secondary path $\boldsymbol{G}(z)$, following

$$\mathbf{y}(n) = \boldsymbol{G}(z)\mathbf{u}(n). \tag{2.32}$$

The control output signal $\mathbf{u}(n)$ is the reference signal $\mathbf{x}(n) \in \mathbb{R}^{K\times 1}$, filtered by the

set of control coefficients $\boldsymbol{W}(z)$, written as

$$\mathbf{u}(n) = \boldsymbol{W}(z)\mathbf{x}(n). \tag{2.33}$$

As an illustration of ANC, the example given in Fig. 1.3 is used. The reference signal $\mathbf{x}(n)$ is measured by the microphone (2) next to the engine. This reference signal is fed to the controller (3), which computes the convolution of the set of filter coefficients $\boldsymbol{W}(z)$ with the reference signal to result in the control output signal $\mathbf{u}(n)$. The control output signal is driving the secondary source (4), which generates the secondary signal $\mathbf{y}(n)$ at the microphone (6) located in the cabin. The secondary signal cancels the disturbance signal $\mathbf{d}(n)$, so that the error signal $\mathbf{e}(n)$ measured at the microphone (6) in the cabin is being suppressed.

Assuming that the disturbances in the AAC are stationary in time, a set of fixed-gain control coefficients $\boldsymbol{W}(z)$ is used. However, they need to be re-computed if the disturbance signal changes. Furthermore, it is assumed that a feedforward reference signal is available in the AAC, which allows the implementation of a feedforward controller. Therefore, the fixed-gain feedforward control setup shown in this section can be applied to suppress the reflections in an AAC, with two challenges. First of all, the reflected sound field needs to be known, in order to design a set of control coefficients $\boldsymbol{W}(z)$ that specifically tries to suppress the reflections. Furthermore, as explained in the introduction, for effective control in larger geometries and with shorter wavelengths, the number of sources and sensors increases quickly. Therefore, obtaining the set of control coefficients $\boldsymbol{W}(z)$ for systems with a large number of sources and sensors can become computationally expensive. The next sections show the derivation of existing algorithms, which forms the basis for developing the algorithms with reduced computational complexity and memory consumption in this thesis.

To derive the existing algorithms, a feedforward system is assumed. The block diagram in Fig. 2.2 is purely feedforward, which is possible only in cases without, or with very little contamination of the reference signals, which might be possible if acceleration, velocity or other types of sensors are used, because these might have a weak acoustic coupling with the secondary sources. However, when reference microphones are used, internal model control (IMC) [44] is typically applied to compensate for the contamination of the reference signals due to the secondary sources. The idea of IMC is explained in the next section.

2.2.3 Internal model control (IMC)

Depending on the system configuration, the secondary source signals can significantly contaminate the reference signals. In general, this is the case if reference microphones are used, because the acoustic coupling with the secondary sources is typically strong. The coupling between the reference microphones and the secondary sources is schematically shown in the block diagram depicted in Fig. 2.3, in which one can see a feedback loop from the control signals $\boldsymbol{u}(n)$ driving the secondary sources to the reference signals $\boldsymbol{x}(n)$ via the path modelled with $\boldsymbol{G}_s(z) \in \mathbb{R}^{M\times K}$. This feedback signal can lead to a reduction in performance or instability of the noise control system, because a perfect feedforward model is assumed to compute the control

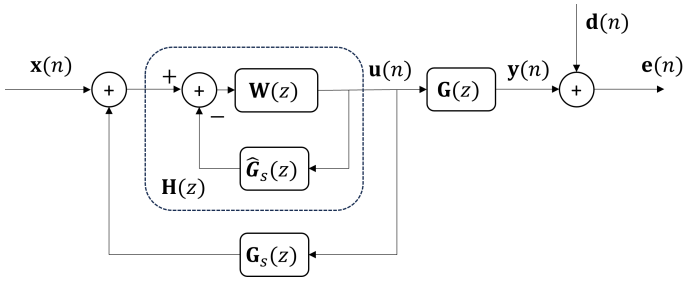

Figure 2.3: Block diagram of a multichannel feedforward control system with feedback cancellation using internal model control.

coefficients $\boldsymbol{W}(z)$. A method to account for the feedback path is by having an internal model of the feedback path $\hat{\boldsymbol{G}}_s(z) \in \mathbb{R}^{M\times K}$. Using this internal model, the feedback signals are predicted and subtracted from the measured reference signals [44]. The real feedback signals indicated with the filter $\boldsymbol{G}_s(z)$ are being added to the reference signals. Therefore, a model of the feedback path $\hat{\boldsymbol{G}}_s(z)$ is used to predict and subtract the feedback signals from the reference signals. If the model of the feedback path is perfect, so that $\boldsymbol{G}_s(z) = \hat{\boldsymbol{G}}_s(z)$, then the block diagram becomes purely feedforward, which is assumed in Sec. 2.2.2. It is assumed that by implementing IMC a feedforward configuration is obtained. The next section describes the derivation of the optimal set of control coefficients in the time domain, by assuming a feedforward configuration.

2.2.4 The optimal set of control coefficients in the time domain

By assuming that a (perfect) feedforward configuration is available, the set of optimal time domain control coefficients can be derived. As already explained, in Eq. (2.33) the controller needs a set of instructions, named the control coefficients $\boldsymbol{W}(z)$. The optimal causal set of control coefficients in the time domain is known as the Wiener filter and shown in [44]. The derivation starts in index-form, but could also be fully represented in a vector-form. With reference to the feedforward scheme in Fig. 2.2, the error signal is defined as

$$e_{\mathrm{l}}(n) = d_{\mathrm{l}}(n) + \sum_{m=1}^{M}\sum_{j=0}^{J-1} g_{\mathrm{lmj}} u_{\mathrm{m}}(n-j), \tag{2.34}$$

in which g_{lmj} represents the impulse response from the m-th secondary actuator to the l-th error sensor with a J-th-order FIR filter. The signal driving the m-th secondary actuator is defined as

$$u_{\mathrm{m}}(n) = \sum_{k=1}^{K}\sum_{i=0}^{I-1} W_{\mathrm{mki}} x_k(n-i), \tag{2.35}$$

in which W_{mki} represents the set of control filters from the k-th reference sensor to the m-th secondary actuator, with an I-th-order FIR filter. Therefore, the error signal

can be written as

$$e_{\mathrm{l}}(n) = d_{\mathrm{l}}(n) + \sum_{m=1}^{M}\sum_{j=0}^{J-1}\sum_{k=1}^{K}\sum_{i=0}^{I-1} g_{\mathrm{lmj}} W_{\mathrm{mki}} x_{\mathrm{k}}(n-i-j). \tag{2.36}$$

Assuming that the filters g_{lmj} and W_{mki} are time-invariant, which is valid for stationary and ergodic signals [44], the filters can be re-ordered. The filtered-reference signals are defined as

$$r_{\mathrm{lmk}}(n) = \sum_{j=0}^{J-1} g_{\mathrm{lmj}} x_{\mathrm{k}}(n-j). \tag{2.37}$$

This then leads to a new form of Eq. (2.36) written as:

$$e_{\mathrm{l}}(n) = d_{\mathrm{l}}(n) + \sum_{m=1}^{M}\sum_{k=1}^{K}\sum_{i=0}^{I-1} W_{\mathrm{mki}} r_{\mathrm{lmk}}(n-i), \tag{2.38}$$

or in a vector form as

$$e_{\mathrm{l}}(n) = d_{\mathrm{l}}(n) + \sum_{i=0}^{I-1} \boldsymbol{W}_i^T \boldsymbol{r}_{\mathrm{l}}(n-i), \tag{2.39}$$

in which

$$\boldsymbol{W}_i = [W_{11\mathrm{i}}, W_{12\mathrm{i}}, \ldots, W_{1\mathrm{Ki}}, W_{21\mathrm{i}}, \ldots, W_{\mathrm{MKi}}]^T, \tag{2.40}$$

and

$$\mathbf{r}_{\mathrm{l}}(n) = [r_{\mathrm{l}11}(n), r_{\mathrm{l}12}(n), \ldots, r_{\mathrm{l}1\mathrm{K}}(n), r_{\mathrm{l}21}(n), \ldots, r_{\mathrm{lMK}}(n)]^T. \tag{2.41}$$

The error signal can now be written as

$$\mathbf{e}(n) = \mathbf{d}(n) + \boldsymbol{R}(n)\boldsymbol{W}, \tag{2.42}$$

in which

$$\boldsymbol{R}(n) = \begin{bmatrix} \mathbf{r}_1^T(n) & \mathbf{r}_1^T(n-1) & \ldots & \mathbf{r}_1^T(n-I+1) \\ \mathbf{r}_2^T(n) & \mathbf{r}_2^T(n-1) & & \\ \vdots & & \ddots & \\ \mathbf{r}_{\mathrm{L}}^T(n) & \mathbf{r}_{\mathrm{L}}^T(n-1) & \ldots & \mathbf{r}_{\mathrm{L}}(n-I+1) \end{bmatrix}, \tag{2.43}$$

with

$$\boldsymbol{W} = [\mathbf{W}_0^T, \ldots, \mathbf{W}_{I-1}^T]^T, \tag{2.44}$$

and

$$\mathbf{d}(n) = [d_1(n), \ldots, d_L(n)]^T. \tag{2.45}$$

With the error signal expressed in the matrix form, the optimal set of filter coefficients is computed by minimizing the cost function. The cost function is defined as the expectation of the sum of the squared error signals, written as

$$\begin{aligned} \mathcal{J} &= \mathrm{E}\left[\boldsymbol{e}^T(n)\boldsymbol{e}(n)\right], \\ &= \boldsymbol{W}^T \mathrm{E}\left[\boldsymbol{R}^T(n)\boldsymbol{R}(n)\right]\boldsymbol{W} + 2\boldsymbol{W}^T \mathrm{E}\left[\boldsymbol{R}^T(n)\boldsymbol{d}(n)\right] + \mathrm{E}\left[\mathbf{d}^T(n)\mathbf{d}(n)\right], \end{aligned} \tag{2.46}$$

in which $\mathrm{E}[\cdot]$ denotes the expectation operator. The solution of the previous optimization problem has a global minimum if $\mathrm{E}\left[\boldsymbol{R}^T(n)\boldsymbol{R}(n)\right]$ is positive definite, which is the case if the inputs are sufficiently persistently excited [44]. The global minimum is found by setting the derivative of $\mathcal{J}$ with respect to the filter coefficients $\boldsymbol{W}$ equal to zero, written as

$$\frac{\partial \mathcal{J}}{\partial \boldsymbol{W}} = 2\mathrm{E}\left[\boldsymbol{R}^T(n)\boldsymbol{R}(n)\right]\boldsymbol{W} + 2\mathrm{E}\left[\boldsymbol{R}^T(n)\mathbf{d}(n)\right] = 0, \tag{2.47}$$

which further can be solved for the optimal set of filter coefficients

$$\boldsymbol{W}_{\mathrm{opt}} = -\mathrm{E}\left[\boldsymbol{R}^T(n)\boldsymbol{R}(n)\right]^{-1}\mathrm{E}\left[\boldsymbol{R}^T(n)\mathbf{d}(n)\right]. \tag{2.48}$$

The matrix $\mathrm{E}\left[\boldsymbol{R}^T(n)\boldsymbol{R}(n)\right]$ is of size MKI-by-MKI, and has a Toeplitz-block structure [124]. Direct inversion is possible, but this operation is computationally expensive with a complexity of $\mathcal{O}((MKI)^3)$. Levinson-Durbin recursion [71] reduces the complexity from $\mathcal{O}(I^3)$ to $\mathcal{O}(I^2)$ for SISO systems, although this can be extended to MIMO systems [125]. This algorithm solves the equations recursively to avoid resolving them for each sample number [126]. In [127] a recursive algorithm is shown that utilizes the structural and displacement-rank properties of the Toeplitz matrix. It is mentioned that the extension to Toeplitz-block systems is straightforward, but this is not shown. The numerical stability and propagation of roundoff errors during calculations has not yet been investigated. In [128] an implementation of the generalized Schur algorithm for a real positive definite Toeplitz matrix is suggested, but, an extension to Toeplitz-block systems has not been presented. In [129] an algorithm is shown to compute Padé approximants and to solve Toeplitz systems of equations. It is shown that the Padé tables and Toeplitz systems are intimately related. It is mentioned that the algorithm can be generalized to deal with Toeplitz-block systems, in which matrix coefficients rather than scalar coefficients should be considered. However, the question of numerical stability is not studied. In [130] the Bareiss algorithm [131] is used to calculate the coefficients in the Levinson recurrence and then the solution is computed using the Levinson recursion. An extension towards Toeplitz-block matrices is not studied. These presented algorithms [127–130] are named fast Toeplitz solvers, which have a computational complexity of $\mathcal{O}(MKI\log^2(MKI))$. The concept of displacement structure [132] has been used to solve problems connected with Toeplitz matrices, in which the displacement rank is introduced as a measure of how 'close' to Toeplitz a given matrix is. Similar to the displacement structure, hierarchical techniques are proposed [133–135]. With these hierarchical techniques, the matrix is represented in a sequentially semi-separable (SSS) or a hierarchically semi-separable (HSS) structure, which requires $\mathcal{O}((MKI)^2)$ computational complexity for the conversion. Once in the SSS or HSS representation, matrix inversion is of $\mathcal{O}(k^3MKI)$ complexity [136] in which k denotes the level of hierarchy. A superfast structured solver for Toeplitz systems via randomized sampling is proposed in [137]. In this work, the use of displacement equations to transform a Toeplitz matrix into a Cauchy-like matrix is proposed. Such a Cauchy-like matrix has low-numerical-rank off-diagonal blocks, which allows for a fast conversion to the HSS representation. However, it is unclear whether this gen-

eralizes to Toeplitz-block matrices. Iterative methods based on the conjugate gradient (CG) method are proposed to solve the system of linear equations involving a Toeplitz-block matrix [138, 139]. Later, preconditioning techniques are proposed to improve convergence speed [140], resulting in the preconditioned conjugate gradient (PCG) algorithm with a computational complexity of $\mathcal{O}(MKI\log(MKI))$ for SISO systems. Different preconditioners are proposed [141–144], which introduce refinements that try to further reduce the condition number to improve convergence speed. Besides the algorithms for classical computers, algorithms to solve Toeplitz systems for quantum computing are presented in [145, 146].

Apart from computing or precomputing the optimal set of control filters in the time domain, it is also possible to deploy an adaptive algorithm [44]. The next sections show the derivation of different adaptive algorithms, starting with the filtered-reference least mean squares (FxLMS) algorithm [44], which is shown in the next section, to allow a natural comparison with the filtered-error least mean squares (FeLMS) algorithm [44].

2.2.5 The filtered-reference least mean squares algorithm (FxLMS)

A commonly used adaptive algorithm in active noise control is the FxLMS algorithm, which assumes that the plant model $\boldsymbol{G}(z)$ is available. In contrast to Sec. 2.2.4, in which the control filters are assumed to be time invariant, with this algorithm the control filters are time-variant and are only varying slowly in comparison with the timescales of the plant dynamics. In such a case, the vector of error signals is denoted by

$$\mathbf{e}(n) = \mathbf{d}(n) + \boldsymbol{R}(n)\boldsymbol{W}(n). \tag{2.49}$$

Because the control filter coefficients $\boldsymbol{W}(n)$ are time-dependent, an instantaneous cost function given by the instantaneous sum of squared outputs of the error signals can be introduced:

$$\begin{aligned}\mathcal{J} &= \mathbf{e}^T(n)\mathbf{e}(n),\\ &= \boldsymbol{W}^T(n)\boldsymbol{R}^T(n)\boldsymbol{R}(n)\boldsymbol{W}(n) + 2\boldsymbol{W}^T(n)\boldsymbol{R}^T(n)\mathbf{d}(n) + \mathbf{d}^T(n)\mathbf{d}(n),\end{aligned} \tag{2.50}$$

which is different from the cost function of the optimal time domain filter in Eq. (2.46), defined as the expectation of the sum of squared error signals. The derivative of this cost function with respect to the filter coefficients $\boldsymbol{W}(n)$ then reads

$$\frac{\partial\mathcal{J}}{\partial\boldsymbol{W}(n)} = 2[\boldsymbol{R}^T(n)\boldsymbol{R}(n)\boldsymbol{W}(n) + \boldsymbol{R}^T(n)\mathbf{d}(n)], \tag{2.51}$$

which is referred to as the gradient, and can be rewritten as

$$\frac{\partial\mathcal{J}}{\partial\boldsymbol{W}(n)} = 2\boldsymbol{R}^T(n)\mathbf{e}(n), \tag{2.52}$$

by substitution of Eq. (2.49). The vector of derivatives of the instantaneous squared errors is used to adapt the control filter coefficients, which is used as an estimate for

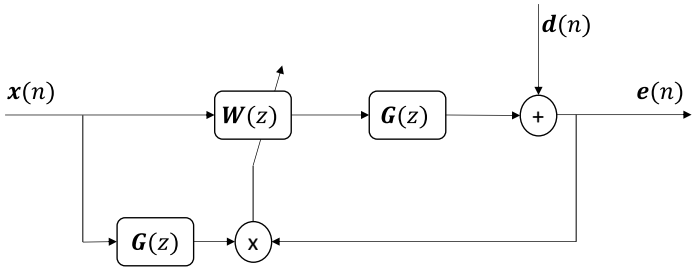

Figure 2.4: Block diagram of the filtered-reference LMS algorithm.

the output of the expectation operator. This gives the update rule of the multichannel FxLMS algorithm

$$\boldsymbol{W}(n+1) = \boldsymbol{W}(n) - \alpha \boldsymbol{R}^T(n)\mathbf{e}(n), \tag{2.53}$$

in which α is the convergence coefficient, resulting in the FxLMS block diagram as shown in Fig. 2.4. The total number of operations of this algorithm per sample is $(I+J)KLM$ [44]. A different popular adaptive algorithm with a lower computational complexity in the case of multiple reference signals is the FeLMS algorithm.

2.2.6 The filtered-error least mean squares algorithm (FeLMS)

Besides the FxLMS algorithm, the FeLMS algorithm is also popular in ANC applications. A multichannel form of the FeLMS algorithm can be obtained starting from the error signal in Eq. (2.36), by dropping the dependence on the primary sources, resulting in a matrix-vector formulation:

$$\mathbf{e}(n) = \mathbf{d}(n) + \sum_{j=0}^{J-1}\sum_{i=0}^{I-1} \boldsymbol{G}_j \boldsymbol{W}_i \mathbf{x}(n-i-j). \tag{2.54}$$

With this error signal, the cost function in Eq. (2.46) is used [60], of which the derivative with respect to the elements of the i-th matrix of controller coefficients can be written as

$$\frac{\partial \mathcal{J}}{\partial \boldsymbol{W}_i} = 2\mathrm{E}\left[\sum_{j=0}^{J-1} \boldsymbol{G}_j^T \mathbf{e}(n+j)\mathbf{x}^T(n-i)\right], \tag{2.55}$$

as shown in [44]. The vector of M filtered-error signals is defined as

$$\mathbf{f}(n) = \sum_{j=0}^{J-1} \boldsymbol{G}_j^T \mathbf{e}(n+j), \tag{2.56}$$

which upon substitution in Eq. (2.55) results in

$$\frac{\partial \mathcal{J}}{\partial \boldsymbol{W}_i} = 2\mathrm{E}\left[\mathbf{f}(n)\mathbf{x}^T(n-i)\right]. \tag{2.57}$$

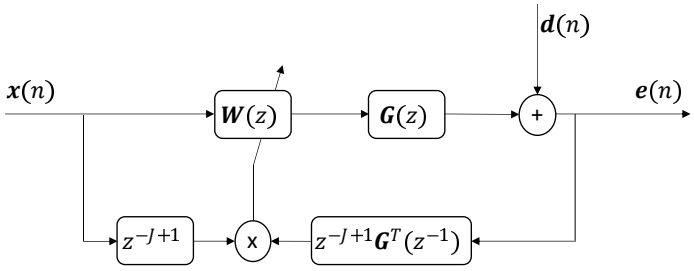

Figure 2.5: Block diagram of the filtered-error LMS algorithm.

The derivative contains the expectation operator, which in practice would need to be realized by performing an average over time after each iteration of the algorithm [60]. This is very time-consuming and therefore an instantaneous version of this derivative is used, which is taken at a specific moment in time instead of an average over time. Using the instantaneous version of this derivative to adapt the matrix of the i-th control filter coefficients at the n-th time, the multichannel adaptive form of the filtered-error LMS algorithm reads as:

$$\boldsymbol{W}_i(n+1) = \boldsymbol{W}_i(n) - \alpha \mathbf{f}(n)\mathbf{x}^T(n-i), \tag{2.58}$$

which is known as the adjoint LMS algorithm, because the error is filtered through an adjoint filter of the error channel [147]. However, Eq. (2.56) requires time-advanced error signals, which are not available in causal systems. To mitigate the causality problem, a delay of both the filtered-error signals and the reference signals by $J-1$ samples is introduced, such that the update equation becomes

$$\boldsymbol{W}_i(n+1) = \boldsymbol{W}_i(n) - \alpha \mathbf{f}(n-J+1)\mathbf{x}^T(n-i-J+1). \tag{2.59}$$

This results in the FeLMS algorithm of which the block diagram is shown in Fig. 2.5. The figure shows that the error signal is filtered causally with the delayed, transposed and time-reversed version of the secondary path $(z^{-J+1})\boldsymbol{G}^T(z^{-1})$, resulting in the filtered-error signal. Furthermore, the reference signal is delayed by the same number of samples, resulting in the delayed reference signal. The outer product of the filtered-error signals and the delayed reference signals is then used to update the control coefficients.

The total number of operations of this algorithm per sample is $(IK + JL)M$ [44], which is lower than the number of operations of the FxLMS algorithm when multiple reference signals are used. However, the FeLMS algorithm may have a lower convergence rate than the FxLMS algorithm due to the added delay to make the algorithm causal [44].

2.2.7 A rapidly converging filtered-error algorithm

The FeLMS algorithm as derived in the previous section suffers from poor convergence due to the correlated reference signals and the coupled plant response. There-

fore, the preconditioned LMS algorithm is proposed in [44]. In this algorithm, preconditioning and decoupling filters are added in the secondary path to reduce the coupling in the plant response. Furthermore, a prewhitening filter is added which decorrelates and whitens the reference signals. However, the preconditioned LMS algorithm still needs the delay in the adaptation path to ensure causality, similar to Eq. (2.59). This delay results in reduced convergence speed. Therefore, a modified and preconditioned version of the FeLMS algorithm is proposed in [54]. The block scheme of the proposed algorithm is shown in Fig. 2.6. The figure shows that the adaptation loop with the LMS update is completely free from any delays, by introducing a copy of the filter coefficients. With an inner-outer factorization approach a preconditioning filter $\bar{\boldsymbol{G}}_o^{-1}$, which is the inverse of the minimum-phase part of the secondary path $\bar{\boldsymbol{G}}$, is computed. Furthermore, with the inner-outer factorization, the adjoint $\bar{\boldsymbol{G}}_i^*$ of the all-pass part of $\bar{\boldsymbol{G}}$ is computed. The use of the preconditioning filter at the control output signals, together with the adjoint filter $\bar{\boldsymbol{G}}_i^*$ at the error signals, diagonalizes the system, so that frequency dependence is reduced. Lastly, the scheme incorporates regularization of the secondary path $\bar{\boldsymbol{G}}$, to reduce the controller output at frequencies where the secondary path has low amplification values. This results in a rapidly converging filtered-error algorithm.

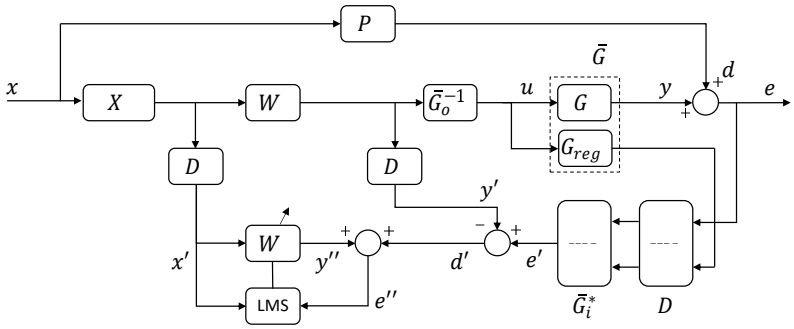

Figure 2.6: Block diagram of the regularized modified filtered-error adaptive control scheme [54].

The inner-outer factorization approach requires a state-space model of the plant, and has a computational complexity of $2(N+M)^2$, in which N is the number of states of the state-space model. Furthermore, the computational complexity of each control filter is $2IKM$ and the computational complexity of the filtering of the error signals is $4JLM$ [54].

2.2.8 The optimal set of control coefficients in the frequency domain

Besides the time domain strategies, the equations of the optimal controller can also be expressed in the frequency domain. This section shows the derivation of the causally unconstrained controller in the frequency domain, following the approach shown in [44]. Using the same convention as in the time domain case, the Fourier

transform of the error signal in Eq. (2.36) can be written in a vector-form as

$$\mathbf{e}(\mathrm{e}^{\mathrm{j}\omega}) = \mathbf{d}(\mathrm{e}^{\mathrm{j}\omega}) + \boldsymbol{G}(\mathrm{e}^{\mathrm{j}\omega})\boldsymbol{W}(\mathrm{e}^{\mathrm{j}\omega})\mathbf{x}(\mathrm{e}^{\mathrm{j}\omega}), \tag{2.60}$$

in which $\boldsymbol{G}(\mathrm{e}^{\mathrm{j}\omega})$ is the matrix of FRFs of the secondary path and $\boldsymbol{W}(\mathrm{e}^{\mathrm{j}\omega})$ is the set of control filter FRFs. The trace operator is invariant under circular shifts, allowing for the most convenient method of analysis [44]. Therefore, the cost function is defined as the trace of the outer product of the error signal summed over the primary sources, as follows:

$$\mathcal{J} = \mathrm{E}\left[\mathbf{e}^H(\mathrm{e}^{\mathrm{j}\omega})\mathbf{e}(\mathrm{e}^{\mathrm{j}\omega})\right] = \mathrm{tr.E}\left[\mathbf{e}(\mathrm{e}^{\mathrm{j}\omega})\mathbf{e}^H(\mathrm{e}^{\mathrm{j}\omega})\right], \tag{2.61}$$

in which the superscript $(\cdot)^H$ denotes the Hermitian transpose and tr.$(\cdot)$ denotes the trace operator. For simplicity of notation, in further text the explicit dependence on $(\mathrm{e}^{\mathrm{j}\omega})$ is left out. In the unconstrained case the matrix of controller responses that minimizes the cost function independently at each frequency is found, which means that after transformation to the time domain the controller is not necessarily causal. By writing the filter coefficients as

$$\boldsymbol{W}(z) = \sum_{n=0}^{I-1} \boldsymbol{w}(n) z^{-n}, \tag{2.62}$$

the non-causality occurs if

$$\boldsymbol{w}(n) \neq 0, \quad n < 0, \tag{2.63}$$

which means that the filter has a nonzero response in negative time. Substitution of Eq. (2.60) into Eq. (2.61) results in

$$\mathcal{J} = \mathrm{tr.E}\left[\boldsymbol{G}\boldsymbol{W}\mathbf{x}\mathbf{x}^H\boldsymbol{W}^H\boldsymbol{G}^H + \boldsymbol{G}\boldsymbol{W}\mathbf{x}\mathbf{d}^H + \mathbf{d}\mathbf{x}^H\boldsymbol{W}^H\boldsymbol{G}^H + \mathbf{d}\mathbf{d}^H\right]. \tag{2.64}$$

Because the expectation needs to be taken only over the stochastic parts, which involve $\mathbf{x}$ and $\mathbf{d}$, it is convenient to define the K-by-K matrix of power and cross spectral densities for the reference signals as

$$\boldsymbol{S}_{\mathrm{xx}} = \mathrm{E}\left[\mathbf{x}\mathbf{x}^H\right]. \tag{2.65}$$

The L-by-K matrix of cross spectral densities between the disturbance and reference signals is defined as

$$\boldsymbol{S}_{\mathrm{xd}} = \mathrm{E}\left[\mathbf{d}\mathbf{x}^H\right], \tag{2.66}$$

and the L-by-L matrix of power and cross spectral densities for the disturbance signals is defined as

$$\boldsymbol{S}_{\mathrm{dd}} = \mathrm{E}\left[\mathbf{d}\mathbf{d}^H\right]. \tag{2.67}$$

Using these definitions, the cost function in Eq. (2.64) further reads as

$$\mathcal{J} = \mathrm{tr.}\left[\boldsymbol{G}\boldsymbol{W}\boldsymbol{S}_{\mathrm{xx}}\boldsymbol{W}^H\boldsymbol{G}^H + \boldsymbol{G}\boldsymbol{W}\boldsymbol{S}_{\mathrm{xd}}^H + \boldsymbol{S}_{\mathrm{xd}}\boldsymbol{W}^H\boldsymbol{G}^H + \boldsymbol{S}_{\mathrm{dd}}\right], \tag{2.68}$$

from which the optimal filter can be derived at each frequency, by differentiating the cost function with respect to the real $\mathcal{R}(\cdot)$ and imaginary $\mathcal{I}(\cdot)$ parts of $\boldsymbol{W}$ and equating this to zero

$$\frac{\partial \mathcal{J}}{\partial \mathcal{R}(\boldsymbol{W})} + j\frac{\partial \mathcal{J}}{\partial \mathcal{I}(\boldsymbol{W})} = 2(\boldsymbol{G}^H \boldsymbol{G}\boldsymbol{W}\boldsymbol{S}_{\mathrm{xx}} + \boldsymbol{G}^H \boldsymbol{S}_{\mathrm{xd}}) = 0. \tag{2.69}$$

The matrix of unconstrained optimal filter coefficients is found by solving the previous equation to obtain:

$$\boldsymbol{w}_{\mathrm{opt}} = -[\boldsymbol{G}^H \boldsymbol{G}]^{-1} \boldsymbol{G}^H \boldsymbol{S}_{\mathrm{xd}} \boldsymbol{S}_{\mathrm{xx}}^{-1}, \tag{2.70}$$

for each frequency, provided both $[\boldsymbol{G}^H \boldsymbol{G}]$ and $\boldsymbol{S}_{\mathrm{xx}}$ are positive definite such that the cost function in Eq. (2.68) has a unique global minimum [44]. Computing the solution of Eq. (2.70) for each frequency is computationally more attractive than the computation of the time domain controller in Eq. (2.48). However, the filter obtained using this frequency domain approach is not necessarily causal, which means that it may require knowledge of the future as well as the past behaviour of the reference signal [60], as shown in Eq. (2.63). Therefore, a non-causal controller cannot be implemented in real-time systems, and a causal controller is a necessity for real-time active control of stochastic disturbances [44].

2.2.9 Causally constraining the control coefficients

In the previous section the derivation of the optimal set of control coefficients in the frequency domain is shown. However, the resulting set of control coefficients is not necessarily causal. Therefore, this section shows the involved equations expressed in the z-domain, to constrain the set of filter coefficients, to be causal. The approach in this section follows the derivation shown in [44]. In the z-domain, this constraint can be written as

$$\{\boldsymbol{G}^T(z^{-1}) \boldsymbol{S}_{\mathrm{xe}}(z)\}_+ = \boldsymbol{0}, \tag{2.71}$$

in which

$$\boldsymbol{S}_{\mathrm{xe}}(z) = \mathrm{E}\left[\mathbf{e}(z)\mathbf{x}^T(z^{-1})\right]. \tag{2.72}$$

Here, $\{\cdot\}_+$ denotes the causality constraint, which is defined as retaining the causal part of the quantity inside the brackets. The matrix $\boldsymbol{G}^T(z^{-1})$ represents the transposed and time-reversed matrix of plant impulse responses. By expressing the error signal in the z-domain, written as

$$\mathbf{e}(z) = \mathbf{d}(z) + \boldsymbol{G}(z)\boldsymbol{W}(z)\mathbf{x}(z), \tag{2.73}$$

the spectral density matrix is rewritten as

$$\boldsymbol{S}_{\mathrm{xe}}(z) = \boldsymbol{S}_{\mathrm{xd}}(z) + \boldsymbol{G}(z)\boldsymbol{W}(z)\boldsymbol{S}_{\mathrm{xx}}(z), \tag{2.74}$$

in which

$$\boldsymbol{S}_{\mathrm{xd}}(z) = \mathrm{E}\left[\mathbf{d}(z)\mathbf{x}^T(z^{-1})\right], \tag{2.75}$$

and

$$\boldsymbol{S}_{\mathrm{xx}}(z) = \mathrm{E}\left[\mathbf{x}(z)\mathbf{x}^T(z^{-1})\right]. \tag{2.76}$$

The condition for the optimal matrix of causal filters can thus be written as

$$\{\boldsymbol{G}^T(z^{-1})\boldsymbol{S}_{\mathrm{xd}}(z) + \boldsymbol{G}^T(z^{-1})\boldsymbol{G}(z)\boldsymbol{W}(z)\boldsymbol{S}_{\mathrm{xx}}(z)\}_+ = \mathbf{0}. \tag{2.77}$$

In order to solve Eq. (2.77) for the filter coefficients $\boldsymbol{W}(z)$ and to evaluate the causality constraint, the poles and zeros of $\boldsymbol{S}_{\mathrm{xx}}(z)$, $\boldsymbol{S}_{\mathrm{xd}}(z)$ and $\boldsymbol{G}(z)$ are required [44]. If these poles and zeros are not available, the problem can be expressed in the discrete frequency domain to evaluate the causality constraint. For an arbitrary filter $M(\xi)$ the causality constraint can be evaluated [44] as

$$\{M(\xi)\}_+ = \mathcal{F}\left[h(n)\mathcal{F}^{-1}\left(M(\xi)\right)\right], \tag{2.78}$$

in which ξ is the discrete frequency bin number and $h(n)$ is the unit step function with $h(n) = 1, n \geq 0$ and otherwise $h(n) = 0$. It should be noted that the number of frequency bins N must be large enough for the causal part of the impulse response $\mathcal{F}^{-1}(M(\xi))$ to have decayed to zero within $N/2$ samples. The approach of Eq. (2.78) is applied in the algorithm presented in Sec. 4.4 to evaluate the causality constraint in combination with conjugate gradient iterations in the frequency domain.

Chapter 3

Computing the reflected sound field due to the primary sources

3.1 Introduction

To employ an ANC system to suppress the reflections in an AAC, the reflected sound field must be known. This chapter describes an approach to compute the reflected sound field, which is inherently a non-measurable quantity. The approach involves the Kirchhoff-Helmholtz integral (KHI), which allows the computation of the reflected sound field from the measured acoustic pressure and the particle velocity on an enclosed contour. Starting from the inhomogeneous Helmholtz equation, a solution for an unbounded medium is shown in Sec. 3.2. Under appropriate conditions, the inhomogeneous Helmholtz equation reduces to the KHI, which is explained in Sec. 3.3. The KHI for the three-dimensional case is derived in Sec. 3.4, which is shown for completeness. Thereafter, the two-dimensional case is derived and discretized in Sec. 3.5 and Sec. 3.6, and is used throughout the thesis to compute the reflected sound field due to the primary sources in numerical studies and in experiments.

3.2 The solution of the inhomogeneous Helmholtz equation

The starting point of the derivation of the KHI is the inhomogeneous Helmholtz equation. This section shows the derivation of the inhomogeneous Helmholtz equation with a solution in an unbounded medium, following the approach of [60]. The object to be studied is positioned in the middle of the AAC. At this point it is assumed that the object to be studied can be enclosed by an arbitrary surface S enclosing the volume V containing the object, as depicted in Fig. 3.1, showing the cross-section of the volume. The normal vector $\mathbf{n}$ is pointing into the volume V.

Parts of the method presented in this chapter are published and applied in [148], [149] and submitted in [150].

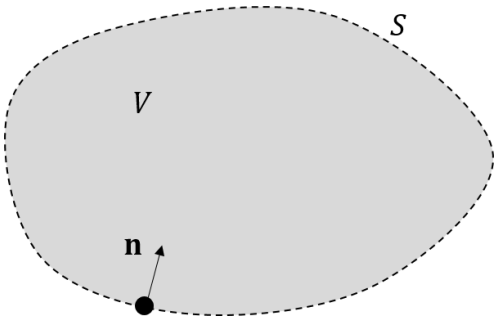

Figure 3.1: The volume V and its bounding surface S with its normal vector $\mathbf{n}$.

The inhomogeneous Helmholtz equation is introduced in Eq. (2.13), which can be rewritten as

$$\nabla^2 p(\mathbf{x},\omega) + k^2 p(\mathbf{x},\omega) = -Q_{\text{vol}}(\mathbf{x},\omega), \tag{3.1}$$

in which $Q_{\text{vol}}(\mathbf{x},\omega)$ can consist of a combination of different types of sources, for example a point mass source or an external force on the fluid, as explained in Sec. 2.1.1. Multiplication of Eq. (3.1) with $G(\mathbf{x}|\mathbf{x}_0,\omega)$ results in

$$G(\mathbf{x}|\mathbf{x}_0,\omega)\nabla^2 p(\mathbf{x},\omega) + k^2 G(\mathbf{x}|\mathbf{x}_0,\omega)p(\mathbf{x},\omega) = -G(\mathbf{x}|\mathbf{x}_0,\omega)Q_{\text{vol}}(\mathbf{x},\omega). \tag{3.2}$$

Multiplication of Eq. (2.16) with $p(\mathbf{x},\omega)$, which is the Helmholtz equation expressed with the Green's function, followed by multiplication with the acoustic pressure, yields

$$p(\mathbf{x},\omega)(\nabla^2 + k^2)G(\mathbf{x}|\mathbf{x}_0,\omega) = -p(\mathbf{x},\omega)\delta(\mathbf{x}-\mathbf{x}_0). \tag{3.3}$$

Subtraction of Eq. (3.3) from Eq. (3.2) results in

$$\begin{aligned} G(\mathbf{x}|\mathbf{x}_0,\omega)\nabla^2 p(\mathbf{x},\omega) - p(\mathbf{x},\omega)\nabla^2 G(\mathbf{x}|\mathbf{x}_0,\omega) = \\ -Q_{\text{vol}}(\mathbf{x},\omega)G(\mathbf{x}|\mathbf{x}_0,\omega) + p(\mathbf{x},\omega)\delta(\mathbf{x}-\mathbf{x}_0). \end{aligned} \tag{3.4}$$

The variables $\mathbf{x}$ and $\mathbf{x}_0$ are interchanged, the symmetry of $\delta(\mathbf{x}-\mathbf{x}_0)$ and the reciprocity property $G(\mathbf{x}|\mathbf{x}_0,\omega) = G(\mathbf{x}_0|\mathbf{x},\omega)$ are utilized [102], and both sides of the equation are integrated over a volume V that is bounded by a surface S with respect to the variables $\mathbf{x}_0$ [102], as depicted in Fig. 3.1, resulting in

$$\begin{aligned} &\int_{\mathbf{x}_0\in V} G(\mathbf{x}|\mathbf{x}_0,\omega)\nabla^2 p(\mathbf{x}_0,\omega) - p(\mathbf{x}_0,\omega)\nabla^2 G(\mathbf{x}|\mathbf{x}_0,\omega)\mathrm{d}\mathbf{x}_0 \\ &+ \int_{\mathbf{x}_0\in V} Q_{\text{vol}}(\mathbf{x}_0,\omega)G(\mathbf{x}|\mathbf{x}_0,\omega)\mathrm{d}\mathbf{x}_0 = \begin{cases} p(\mathbf{x},\omega), & \mathbf{x} \text{ within } V, \\ 0, & \mathbf{x} \text{ outside } V, \end{cases} \end{aligned} \tag{3.5}$$

by using the property of the Dirac delta function, written as

$$\int_{\mathbf{x}_0\in V} f(\mathbf{x}_0)\delta(\mathbf{x}_0-\mathbf{x})\mathrm{d}\mathbf{x}_0 = \begin{cases} f(\mathbf{x}), & \mathbf{x} \text{ within } V, \\ 0, & \mathbf{x} \text{ outside } V. \end{cases} \tag{3.6}$$

Lastly, Green's theorem [151] is used to transform the volume integral V on the upper part of Eq. (3.5) into an integral over the surface S, this gives [60, 102]

$$p(\mathbf{x},\omega) = \int_{\mathbf{x}_0 \in V} Q_{\text{vol}}(\mathbf{x}_0,\omega) G(\mathbf{x}|\mathbf{x}_0,\omega) \mathrm{d}\mathbf{x}_0 + \int_{\mathbf{x}_0 \in S} [G(\mathbf{x}|\mathbf{x}_0,\omega) \nabla p(\mathbf{x}_0,\omega) - p(\mathbf{x}_0,\omega) \nabla G(\mathbf{x}|\mathbf{x}_0,\omega)] \cdot \mathbf{n} \mathrm{d}\mathbf{x}_0, \quad (3.7)$$

in which $\mathbf{x}_0$ and $\mathbf{x}$ denote the source position and a position in the volume V, respectively. Thus, the total pressure $p(\mathbf{x},\omega)$ consists of the contribution due to the source distribution $Q_{\text{vol}}(\mathbf{x}_0,\omega)$ in the volume V and the contribution of the surface integral, which requires the acoustic pressure $p(\mathbf{x}_0,\omega)$ and its gradient $\nabla p(\mathbf{x}_0,\omega)$ to be known. To show what the volume integral in Eq. (3.7) represents, first the situation of an unbounded medium is derived, although this is not used in this thesis. In an unbounded medium, the bounding surface S is at infinity. As shown in [60, 102], by applying the Sommerfeld radiation condition (Eq. (2.14)), the two terms in the surface integral of Eq. (3.7) add to zero at all points on the surface S as the radial distance approaches infinity, which means that no energy is reflected back from an infinite distance. In that case, the part of Eq. (3.7) containing the volume integral remains. The solution to the inhomogeneous wave equation in an unbounded medium is therefore written as

$$p(\mathbf{x},\omega) = \int_{\mathbf{x}_0 \in V} Q_{\text{vol}}(\mathbf{x}_0,\omega) G(\mathbf{x}|\mathbf{x}_0,\omega) \mathrm{d}\mathbf{x}_0. \quad (3.8)$$

By substituting the free-space Green's function, as introduced in Eq. (2.17), one arrives at

$$p(\mathbf{x},\omega) = \int_{\mathbf{x}_0 \in V} Q_{\text{vol}}(\mathbf{x}_0,\omega) \frac{\mathrm{e}^{-\mathrm{j}k|\mathbf{x}-\mathbf{x}_0|}}{4\pi|\mathbf{x}-\mathbf{x}_0|} \mathrm{d}\mathbf{x}_0. \quad (3.9)$$

Using the relation that the source term is a combined distribution of volume sources, written as

$$Q_{\text{vol}}(\mathbf{x}_0,\omega) = \mathrm{j}\omega\rho q_{\text{vol}}(\mathbf{x}_0), \quad (3.10)$$

followed by the introduction of a point monopole source at $\mathbf{x}_0$, written as $q_{\text{vol}}(\mathbf{x}) = q\delta(\mathbf{x}-\mathbf{x}_0)$, one arrives at

$$p(\mathbf{x},\omega) = \int_{\mathbf{x}_0 \in V} \mathrm{j}\omega\rho q \delta(\mathbf{x}-\mathbf{x}_0) \frac{\mathrm{e}^{-\mathrm{j}k|\mathbf{x}-\mathbf{x}_0|}}{4\pi|\mathbf{x}-\mathbf{x}_0|} \mathrm{d}\mathbf{x}_0. \quad (3.11)$$

Evaluation of the volume integral, results in

$$p(\mathbf{x},\omega) = \mathrm{j}\omega\rho q \frac{\mathrm{e}^{-\mathrm{j}k|\mathbf{x}-\mathbf{x}_0|}}{4\pi|\mathbf{x}-\mathbf{x}_0|}, \quad (3.12)$$

which is the expression for the complex pressure produced by a point monopole source that is radiating into free-space without any bounds. This shows that the first part of Eq. (3.7) describes the direct sound field, and therefore, the second part of Eq. (3.7) describes the reflected sound field, which is shown in the next section.

3.3 The Kirchhoff-Helmholtz integral

Conversely to the solution of the inhomogeneous wave equation in an unbounded medium, this section shows the KHI, which is used to compute the reflected sound field. With reference to Fig. 3.1, it is assumed that an object to be studied is positioned in the middle of the AAC, surrounded by a volume V, enclosed by a surface S. The part of Eq. (3.7) that describes the direct sound field from a source inside V to the outside of V is not modelled. Then, by choosing the free-field Green's function, the solution to the inhomogeneous wave equation Eq. (3.7) reduces to the KHI equation [60, 101], given by

$$p(\mathbf{x},\omega) = \int_{\mathbf{x}_0 \in S} \left(G(\mathbf{x}|\mathbf{x}_0,\omega) \nabla p(\mathbf{x}_0,\omega) - p(\mathbf{x}_0,\omega) \nabla G(\mathbf{x}|\mathbf{x}_0,\omega) \right) \cdot \mathbf{n} \mathrm{d}\mathbf{x}_0, \tag{3.13}$$

which computes the reflected sound field. Substitution of the inverse propagating Green's function results in the inverse KHI, while substitution of the forward propagating Green's function results in the forward KHI. By choosing to point the normal vector $\mathbf{n}$ to the volume V, the forward KHI computes the sound field generated by a source positioned outside the volume V [108]. Until now the general description has been that the reflected sound field is required. However, at this point it is important to make a distinction between the primary sources and the secondary sources. The primary sources are located within the volume V, which represent the object to be studied in the AAC. The secondary sources, which generate the secondary signal are positioned outside of the volume V. The objective is to suppress the reflected sound field due to the primary sources. Therefore, the forward propagating KHI is suitable, with the configuration as shown in Fig. 3.2. This figure shows that it is assumed that the source is located outside of the volume V, to compute the sound field in the volume V, denoted by position $\mathbf{x}$. With the forward KHI the reflected sound field due to the primary sources is obtained, because only the sound field originating from outside the volume V is modelled (i.e. the reflections), although the source is located within the volume V. Furthermore, the output of the KHI due to the secondary sources is the total sound field, because both the direct sound field and the reflected sound field originate from outside the volume V. However, a transformation of the position variables in Eq. (3.13) is required to model the sound from sources outside of the volume V. Therefore, the substitution $\mathbf{x}_0 \rightarrow \mathbf{x}_s$ is made in Eq. (3.13), which is allowed because the choice of symbols to denote position is only a matter of definition [101]. This gives

$$p(\mathbf{x},\omega) = \int_{\mathbf{x}_s \in S} \left(G(\mathbf{x}|\mathbf{x}_s,\omega) \frac{\partial p(\mathbf{x}_s,\omega)}{\partial n} - p(\mathbf{x}_s,\omega) \frac{\partial G(\mathbf{x}|\mathbf{x}_s,\omega)}{\partial n} \right) \mathrm{d}\mathbf{x}_s, \tag{3.14}$$

in which $\frac{\partial(\cdot)}{\partial n}$ denotes taking the gradient in the direction normal to S [96], and $\mathbf{x}_s$ denotes the position on the surface S. The next sections are dedicated to the derivation of the forward KHI for both the three-dimensional and two-dimensional case, in which the specific Green's functions and its derivatives are shown.

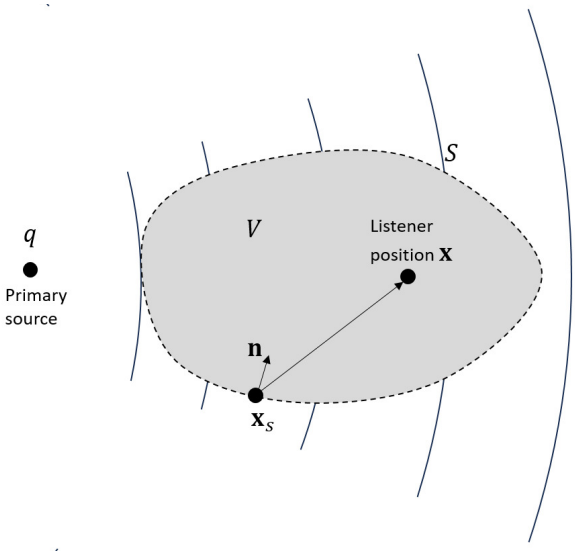

Figure 3.2: Parameters used for the derivation of the Kirchhoff-Helmholtz integral in the general case.

3.4 The three-dimensional Kirchhoff-Helmholtz integral

In this section the three-dimensional version of the forward KHI is derived. Although the numerical studies and experimental tests are all two-dimensional, the three-dimensional version is shown for completeness and future work. The KHI as stated in Eq. (3.14) requires the Green's function, the partial derivative of the Green's function with respect to the normal vector and the pressure and its gradient on the surface. In three dimensions, the free-fields Green's function, as introduced in Eq. (2.17), is defined as

$$G(\mathbf{x}|\mathbf{x}_s,\omega) = \frac{\mathrm{e}^{-\mathrm{j}k|\mathbf{x}-\mathbf{x}_s|}}{4\pi|\mathbf{x}-\mathbf{x}_s|}, \tag{3.15}$$

and its partial derivative with respect to the normal vector $\mathbf{n}$ is written as

$$\begin{aligned}\frac{\partial G(\mathbf{x}|\mathbf{x}_s,\omega)}{\partial n} &= \frac{\partial G(\mathbf{x}|\mathbf{x}_s,\omega)}{\partial \mathbf{x}}\cdot\mathbf{n}, \\ &= -\mathrm{e}^{-\mathrm{j}k|\mathbf{x}-\mathbf{x}_s|}\frac{(1+\mathrm{j}k|\mathbf{x}-\mathbf{x}_s|)}{4\pi|\mathbf{x}-\mathbf{x}_s|^3}(\mathbf{x}-\mathbf{x}_s)\cdot\mathbf{n}.\end{aligned} \tag{3.16}$$

Following [108], the partial derivative of the pressure to the normal direction at S can be written in terms of the particle normal velocity V_n at S as

$$\frac{\partial p(\mathbf{x}_s,\omega)}{\partial n} = \mathrm{j}\rho c k V_n(\mathbf{x}_s,\omega). \tag{3.17}$$

By substituting Eq. (3.15), Eq. (3.16) and Eq. (3.17) into Eq. (3.14) the three-dimensional forward KHI is obtained, written as

$$p^{(3)}(\mathbf{x},\omega) = \frac{1}{4\pi}\int_{\mathbf{x}_s\in S} \frac{\mathrm{e}^{-\mathrm{j}k|\mathbf{x}-\mathbf{x}_s|}}{|\mathbf{x}-\mathbf{x}_s|}(\mathrm{j}\rho ckV_n(\mathbf{x}_s,\omega) + p(\mathbf{x}_s,\omega)\frac{(1+\mathrm{j}k|\mathbf{x}-\mathbf{x}_s|)}{|\mathbf{x}-\mathbf{x}_s|^2}(\mathbf{x}-\mathbf{x}_s)\cdot\mathbf{n})\mathrm{d}\mathbf{x}_s, \quad (3.18)$$

in which the superscript $(\cdot)^{(3)}$ is used to indicate that it is the three-dimensional version. This version of the KHI is necessary in three-dimensional geometries, with for example a spherical surface.

3.5 The two-dimensional Kirchhoff-Helmholtz integral

With respect to Fig. 3.2, in two dimensions the surface becomes a closed contour, in this section denoted by S. The variable $\mathbf{x}_s$ now denotes the position on the contour S instead of on the surface as in the previous section. The KHI as stated in Eq. (3.14) requires the Green's function, the partial derivative of the Green's function with respect to the normal vector and the pressure and its gradient on the surface. The two-dimensional free-field Green's function, which is introduced in Eq. (2.18), is defined as

$$G(\mathbf{x}|\mathbf{x}_s,\omega) = -\frac{\mathrm{j}}{4}H_0^{(2)}(k|\mathbf{x}-\mathbf{x}_s|), \quad (3.19)$$

in which $H_0^{(2)}(\cdot)$ is the second-order Hankel function, defined as

$$H_0^{(2)}(x) = J_0(x) - \mathrm{j}Y_0(x). \quad (3.20)$$

Here, $J_0(\cdot)$ is the Bessel function of the first kind and order 0, and $Y_0(\cdot)$ is the Bessel function of the second kind and order 0. The partial derivative of both Bessel functions are

$$\frac{\partial J_0}{\partial x} = -J_1(x), \quad (3.21)$$

and

$$\frac{\partial Y_0}{\partial x} = -Y_1(x), \quad (3.22)$$

respectively. The partial derivative of the Hankel function then reads

$$\begin{aligned}\frac{\partial H_0^{(2)}(x)}{\partial x} &= -J_1(x) + \mathrm{j}Y_1(x),\\ &= -H_1^{(2)}(x).\end{aligned} \quad (3.23)$$

By using the previous equation, the partial derivative of the Green's function in Eq. (3.19) with respect to the normal vector $\mathbf{n}$ becomes

$$\begin{aligned}\frac{\partial G(\mathbf{x}|\mathbf{x}_s,\omega)}{\partial n} &= \frac{\partial G(\mathbf{x}|\mathbf{x}_s,\omega)}{\partial \mathbf{x}}\cdot\mathbf{n},\\ &= \frac{\mathrm{j}k}{4}H_1^{(2)}(k|\mathbf{x}-\mathbf{x}_s|)\frac{\mathbf{x}-\mathbf{x}_s}{|\mathbf{x}-\mathbf{x}_s|}\cdot\mathbf{n}.\end{aligned} \quad (3.24)$$

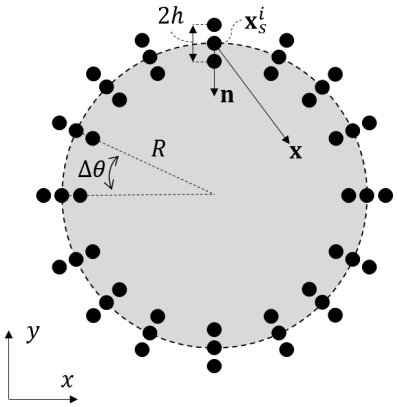

Figure 3.3: Geometry used for the derivation of the Kirchhoff-Helmholtz integral in case of a circular microphone array.

Similarly to the three-dimensional case, Eq. (3.17) can also be applied in two dimensions. Therefore, substitution of Eq. (3.17), Eq. (3.19) and Eq. (3.24) into Eq. (3.14) leads to the two-dimensional forward KHI, written as

$$p^{(2)}(\mathbf{x},\omega) = \frac{-\mathrm{j}k}{4}\int_{\mathbf{x}_s\in S}\Big(\mathrm{j}\rho c V_n(\mathbf{x}_s,\omega)H_0^{(2)}(k|\mathbf{x}-\mathbf{x}_s|) + p(\mathbf{x}_s,\omega)H_1^{(2)}(k|\mathbf{x}-\mathbf{x}_s|)\frac{\mathbf{x}-\mathbf{x}_s}{|\mathbf{x}-\mathbf{x}_s|}\cdot\mathbf{n}\Big)\,\mathrm{d}\mathbf{x}_s, \quad (3.25)$$

in which the superscript $(\cdot)^{(2)}$ is used to indicate that the problem is two-dimensional.

3.6 Discretization and practical implementation of the two-dimensional Kirchhoff-Helmholtz integral

The three-dimensional and two-dimensional KHI as presented in Sec. 3.4 and Sec. 3.5, respectively, require discretization in order to be implemented in practice. This section shows the discretization of the two-dimensional KHI, which is applied in the numerical studies and the experiments throughout this thesis. Fig. 3.3 shows the circular geometry, in which the black dots represent microphones. This geometry is used to discretize the KHI equation. The middle microphone is defined by radii R, the inner microphone is at $R-h$ and the outer microphone is at $R+h$. The angle between each microphone triplet is defined by $\Delta\theta$, assuming that the microphone triplets are equidistantly distributed along the circle. Following the notation of Fig. 3.3, the two-dimensional KHI is simplified using a circular geometry and discretized following [152]. The discrete two-dimensional forward KHI is written as

$$p^{(2)}(\mathbf{x},\omega) = \frac{-\mathrm{j}k}{4}\sum_{i=1}^{L}\Big(\mathrm{j}\rho c V_n(\mathbf{x}_s^i,\omega)H_0^{(2)}(k|\mathbf{x}-\mathbf{x}_s^i|) + p(\mathbf{x}_s^i,\omega)H_1^{(2)}(k|\mathbf{x}-\mathbf{x}_s^i|)\frac{\mathbf{x}-\mathbf{x}_s^i}{|\mathbf{x}-\mathbf{x}_s^i|}\cdot\mathbf{n}\Big)R\Delta\theta, \quad (3.26)$$

in which L denotes the number of sensors on the contour and $\mathbf{x}_s^i$ denotes the position of the sensor i on the contour. As can be seen from Eq. (3.26), the two-dimensional forward KHI requires the acoustic pressure ($p(\mathbf{x}_s^i,\omega)$) and the particle velocity ($V_n(\mathbf{x}_s^i,\omega)$) at the surface. The pressure can be measured using microphones, and the particle velocity can be measured using acoustic vector sensors [98] or particle velocity sensors [99]. However, these sensors are expensive, and it is preferred to use microphones. The use of a circular geometry allows the particle velocity to be approximated with respect to the radial component by a pressure difference at all locations on the contour, which enables the use of microphones. Therefore, in two dimensions, the particle velocity in the radial outward direction is estimated by a difference quotient between the sound pressure levels at $r_{s-h}^i = \|\mathbf{x}_s^i\| - h$ and $r_{s+h}^i = \|\mathbf{x}_s^i\| + h$ (in polar coordinates) and assuming that the centre of the circle is positioned at $(x,y) = (0,0)$, written as

$$V_n(\mathbf{x}_s^i,\omega) = \frac{p(r_{s+h}^i,\omega) - p(r_{s-h}^i,\omega)}{2\mathrm{j}h\omega\rho}, \quad (3.27)$$

in which h is the distance between the sensors in radial direction as indicated in Fig. 3.3. Eq. (3.27) holds as long as h is smaller than the smallest wavelength, such that at least two samples per minimum wavelength are obtained at the Nyquist frequency of the control system. On the other hand, the distance h should not become too small, since this decreases the signal-to-noise ratio of the gradient estimate [30] in Eq. (3.27).

3.7 Conclusion

In this chapter both the two-dimensional and three-dimensional Kirchhoff-Helmholtz integral equations are derived. The evaluation of the forward Kirchhoff-Helmholtz integral within the contour results in the reflected sound field due to a source positioned within the contour. Conversely, evaluation of the forward Kirchhoff-Helmholtz integral within the contour with a source positioned outside the contour results in the total sound field. Throughout this thesis two-dimensional applications are considered. Therefore, to allow practical implementation, the two-dimensional integral is discretized for a circular geometry. To evaluate the integral, the acoustic pressure and the particle velocity at the contour are required. The particle velocity is estimated with a difference quotient between two closely spaced sound pressure measurements, which is possible due to the circular geometry.

Chapter 4

Offline algorithms for active noise control

4.1 Introduction

In the previous chapter the method to compute the reflected sound field due to the primary sources is derived. Once the reflected sound field is known, the set of control filters can be computed with the objective of suppressing the reflections. As explained in Ch. 1, for effective ANC in larger geometries and with shorter wavelengths, the number of sources and sensors increases quickly. The computation of the set of filter coefficients for configurations with a large number of sources and sensors becomes computationally expensive and memory-consuming with existing algorithms. For this reason, this chapter is dedicated to the derivation of three different offline algorithms with reduced computational complexity and memory consumption. The algorithms in this chapter compute a set of control filters that can be implemented using the scheme as shown in Fig. 2.2, such that this set of control filters can be implemented with a fixed-gain feedforward configuration in an AAC. The dependence on the primary sources is shown throughout the derivations, for multiple primary sources in the AAC. With reference to Fig. 2.2, the signals as introduced in Sec. 2.2 are written as $\mathbf{x}(n) \in \mathbb{R}^{K\times 1}$, $\mathbf{u}(n) \in \mathbb{R}^{M\times 1}$, $\mathbf{y}(n) \in \mathbb{R}^{L\times 1}$, $\mathbf{d}(n) \in \mathbb{R}^{L\times 1}$ and $\mathbf{e}(n) \in \mathbb{R}^{L\times 1}$, although dependence on a primary source is indicated with subscript p throughout this chapter. The algorithms are derived using error sensors indicated with L, to have consistency with the literature. However, if the KHI is used with, for example, the application within an AAC, the error sensors L are replaced by the performance sensors L_{perf} throughout the derivations in this chapter. In this case the signal $\mathbf{d}(n) \in \mathbb{R}^{L_{perf}\times 1}$ is the primary noise signal, which is the output of the KHI with the primary sources active, $\mathbf{y}(n) \in \mathbb{R}^{L_{\text{perf}}\times 1}$ is the secondary signal, which is the output of the KHI with the secondary sources active and $\mathbf{e}(n) \in \mathbb{R}^{L_{\text{perf}}\times 1}$ is the performance signal, measured at the performance sensors. The layout of the chapter is as follows, in Sec. 4.2 a scheme is derived which applies LMS iterations to update the set of control filters. In Sec. 4.3 a conjugate gradient

scheme that applies block-circulant preconditioning in the time domain is derived. In Sec. 4.4 a conjugate gradient scheme in the frequency domain is derived, which applies causal control coefficient updates.

4.2 The regularized modified filtered-error scheme with filters derived in the frequency domain

The rapidly converging filtered-error algorithm as described in Sec. 2.2.7 is based on the FeLMS algorithm (Sec. 2.2.6) but as explained in Sec. 2.2.7, has increased computational complexity for larger numbers of sources and sensors. The approach presented in the present section is to derive the preconditioning, decoupling, and prewhitening filter in the frequency domain, which reduces the computational complexity. The multichannel LMS algorithms may suffer from the problem of slow convergence due to [44,53]: 1) the auto-correlation properties of each of the random reference signals, 2) the cross-correlation between the individual reference signals, 3) the dynamic response of each path in the plant response and 4) the cross-coupling between the individual paths in the multichannel plant response. The prewhitening filter is applied to the reference signals to reduce the effects of possible coloring and correlation, which improves convergence speed. The preconditioning and decoupling filters suppress the dynamic responses in the adaptation loop and remove the cross-coupling between the individual paths, which also improves convergence speed. The application of the prewhitening, preconditioning and decoupling filters to the rapidly converging filtered-error algorithm as described in Sec. 2.2.7 results in the regularized modified filtered-error scheme, abbreviated with FD-RMFE which is further referred to in the remainder of the thesis. The block scheme of the FD-RMFE algorithm is shown in Fig. 4.1, which is similar to the block scheme shown in Sec. 2.2.7, but with different preconditioning and decoupling filters. Additionally, a prewhitening filter is added. Although this results in an adaptive algorithm which is typically used in an online approach, the idea is to record the involved signals and pre-compute the set of filter coefficients offline. Using the adaptive algorithm in an offline manner allows an artificial delay to be introduced in the noise signal, which is needed to ensure the causality of the filters because of the delays. After running the algorithm, the obtained filter coefficients can be implemented following the configuration of Fig. 2.2. Although multiple primary sources are considered, the FxLMS algorithm does not initially have knowledge of the spatial distribution of the primary sound field, so it must acquire this information separately and incorporate it into the iterations [153]. The same applies to the FeLMS algorithms and its extensions, such as the FD-RMFE algorithm derived in this section. The dependence on the primary sources is dropped by summation, so that the total primary field remains, assuming that the outputs of the reference sensors are correlated to the outputs of the error sensors [44]. Therefore, with respect to Fig. 4.1, the reference signal is computed as

$$\mathbf{x}(n) = \boldsymbol{X}(z)\mathbf{s}(n), \tag{4.1}$$

The algorithm derived in this section is published in [148].

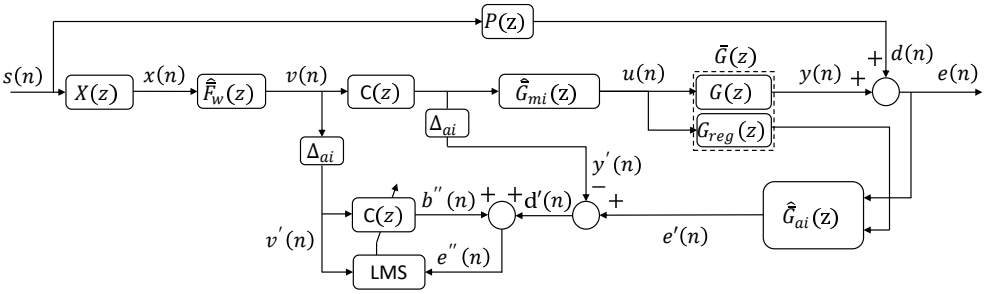

Figure 4.1: Block diagram of the FD-RMFE algorithm with frequency domain derived preconditioning- and prewhitening-filters.

in which $\mathbf{x}(n) \in \mathbb{R}^{K\times 1}$ is the reference signal, $\boldsymbol{X}(z) \in \mathbb{R}^{K\times P}$ is the transfer function matrix from the primary sources to the reference sensors, in which P denotes the number of primary sources, and $\mathbf{s}(n) \in \mathbb{R}^{P\times 1}$ is the driving signal of the primary sources. Similarly, the disturbance signal is computed as

$$\mathbf{d}(n) = \mathbf{P}(z)\mathbf{s}(n), \tag{4.2}$$

in which $\mathbf{d}(n) \in \mathbb{R}^{L\times 1}$ is the disturbance signal and $\boldsymbol{P}(z) \in \mathbb{R}^{L\times P}$ is the transfer function matrix from the primary sources to the error sensors.

The signal $\mathbf{v}(n)$ is obtained after filtering with the prewhitening filter $\hat{\bar{\boldsymbol{F}}}_w(z) \in \mathbb{R}^{K\times K}$. The secondary path $\boldsymbol{G}(z)$ is preconditioned by the filter $\hat{\bar{\boldsymbol{G}}}_{\mathrm{mi}}(z) \in \mathbb{R}^{M\times M}$. The error signal is filtered by the adjoint filter $\hat{\bar{\boldsymbol{G}}}_{\mathrm{ai}}(z) \in \mathbb{R}^{M\times(L+M)}$ to obtain $\mathbf{e}'(n)$. The signal $\mathbf{v}'(n)$ is a delayed version of $\mathbf{v}(n)$, written as

$$\mathbf{v}'(n) = \Delta_{\mathrm{ai}}(z)\mathbf{v}(n), \tag{4.3}$$

in which $\Delta_{\mathrm{ai}}(z)$ is the simulation delay operator corresponding to the delay of Δ_{ai} samples in the filter $\hat{\bar{\boldsymbol{G}}}_{\mathrm{ai}}(z)$ to ensure its causality. Similarly, the signal $\mathbf{y}'(n)$ is a delayed version of the controller output, so that the delays are matched, written as

$$\mathbf{y}'(n) = \Delta_{\mathrm{ai}}(z)\boldsymbol{C}(z)\mathbf{v}(n). \tag{4.4}$$

The secondary path $\boldsymbol{G}(\mathrm{e}^{\mathrm{j}\omega})$ is regularized to reduce the controller output at frequencies where the secondary path has small values to prevent large amplifications, resulting in the augmented filter $\bar{\boldsymbol{G}}(z) \in \mathbb{R}^{(L+M)\times M}$. The update rule for the controller is

$$\boldsymbol{C}_i(n+1) = \boldsymbol{C}_i(n) - \alpha\mathbf{e}''(n)\mathbf{v}'^{T}(n-i), \quad i = 0,\ldots,I-1, \tag{4.5}$$

in which i denotes the tap-delay of the FIR coefficients, assuming a FIR filter length I and α is the convergence coefficient defined as

$$\alpha = \frac{\alpha_0}{\bar{r}}, \tag{4.6}$$

such that α is normalized by the input power and α_0 should be ~ 1. The normalization factor $\bar{r}$ is computed as the norm of the filtered-reference signal $\boldsymbol{r}(n)$ following

$$\bar{r} = ||\bar{\boldsymbol{G}}(z)\hat{\bar{\boldsymbol{G}}}_{\mathrm{mi}}(z)\hat{\bar{\boldsymbol{F}}}_w(z)\mathbf{x}(n)||^2, \tag{4.7}$$

The implementation of input normalization removes the requirement that the user needs to input a convergence coefficient which, if chosen wrongly, may deteriorate algorithm performance. After running the FD-RMFE algorithm, a controller $\boldsymbol{C}(z)$ is obtained, which is converted to the desired controller $\boldsymbol{W}(z)$, similar to the preconditioned LMS algorithm in [44], following

$$\boldsymbol{W}(z) := \hat{\bar{\boldsymbol{G}}}_{\mathrm{mi}}(z)\boldsymbol{C}(z)\hat{\bar{\boldsymbol{F}}}_w(z). \tag{4.8}$$

In this manner the control coefficients $\boldsymbol{W}(z)$ can be implemented following the feedforward configuration as shown in Fig. 2.2.

4.2.1 Frequency domain formulation of the prewhitening and decorrelation filter

In Fig. 4.1 K discrete-time real-valued random reference signals are assumed to be stationary. Otherwise the filter coefficients would be functions of time [44]. The reference signals are possibly correlated, denoted by

$$\mathbf{x}(n) = [x_{1p}(n), \ldots, x_k(n)]^T. \tag{4.9}$$

The correlation matrix of the signal $\mathbf{x}(n)$ [53] can be written as

$$\boldsymbol{R}_{\mathrm{xx}}(m) = E[\mathbf{x}(n+m)\mathbf{x}^T(n)], \qquad -\infty < m < \infty, \tag{4.10}$$

which with the help of the discrete-time Fourier transform, gives the power spectral density (PSD) [154] matrix

$$\boldsymbol{S}_{\mathrm{xx}}(\mathrm{e}^{\mathrm{j}\omega}) = \sum_{m=-\infty}^{\infty} \boldsymbol{R}_{\mathrm{xx}}(m)\mathrm{e}^{-\mathrm{j}\omega m}. \tag{4.11}$$

The PSD matrix $\boldsymbol{S}_{\mathrm{xx}}(\mathrm{e}^{\mathrm{j}\omega}) \in \mathbb{C}^{K\times K}$, which is off-diagonally complex, is a positive semi-definite Hermitian matrix, and therefore an eigenvalue decomposition (EVD) always exists [155], which can be computed for all frequencies following

$$\boldsymbol{S}_{\mathrm{xx}}(\mathrm{e}^{\mathrm{j}\omega}) = \boldsymbol{Q}(\mathrm{e}^{\mathrm{j}\omega})\boldsymbol{D}(\mathrm{e}^{\mathrm{j}\omega})\boldsymbol{Q}^H(\mathrm{e}^{\mathrm{j}\omega}), \tag{4.12}$$

in which $\boldsymbol{D}(\mathrm{e}^{\mathrm{j}\omega})$ is a diagonal matrix containing the real eigenvalues and $\boldsymbol{Q}(\mathrm{e}^{\mathrm{j}\omega})$ contains the normalized eigenvectors. A prewhitening and decorrelation filter can be written as

$$\boldsymbol{F}_w(\mathrm{e}^{\mathrm{j}\omega}) = \boldsymbol{D}^{-\frac{1}{2}}(\mathrm{e}^{\mathrm{j}\omega})\boldsymbol{Q}^H(\mathrm{e}^{\mathrm{j}\omega}), \tag{4.13}$$

which is shown in [53] to diagonalize the PSD matrix of the filtered signal to:

$$\boldsymbol{S}_{\mathrm{ww}}(\mathrm{e}^{\mathrm{j}\omega}) = \boldsymbol{F}_w(\mathrm{e}^{\mathrm{j}\omega})\boldsymbol{S}_{\mathrm{xx}}(\mathrm{e}^{\mathrm{j}\omega})\boldsymbol{F}_w^H(\mathrm{e}^{\mathrm{j}\omega}). \tag{4.14}$$

Substitution of Eq. (4.12) and Eq. (4.13) into Eq. (4.14), results in

$$\begin{aligned} \boldsymbol{S}_{\mathrm{ww}}(\mathrm{e}^{\mathrm{j}\omega}) =& \boldsymbol{D}^{-1/2}(\mathrm{e}^{\mathrm{j}\omega})\boldsymbol{Q}^{H}(\mathrm{e}^{\mathrm{j}\omega})\boldsymbol{Q}(\mathrm{e}^{\mathrm{j}\omega}) \\ & \boldsymbol{D}(\mathrm{e}^{\mathrm{j}\omega})\boldsymbol{Q}^{H}(\mathrm{e}^{\mathrm{j}\omega})\boldsymbol{Q}(\mathrm{e}^{\mathrm{j}\omega}) \left[\boldsymbol{D}^{-1/2}(\mathrm{e}^{\mathrm{j}\omega})\right]^{H}, \\ =& \boldsymbol{I}. \end{aligned} \tag{4.15}$$

The previous results were obtained following [53] and by using

$$\boldsymbol{Q}^{H}(\mathrm{e}^{\mathrm{j}\omega})\boldsymbol{Q}(\mathrm{e}^{\mathrm{j}\omega}) = \boldsymbol{Q}(\mathrm{e}^{\mathrm{j}\omega})\boldsymbol{Q}^{H}(\mathrm{e}^{\mathrm{j}\omega}) = \boldsymbol{I}. \tag{4.16}$$

The filtering of the reference signals with the prewhitening filter gives

$$\mathbf{v}(\mathrm{e}^{\mathrm{j}\omega}) = \boldsymbol{F}_{w}(\mathrm{e}^{\mathrm{j}\omega})\mathbf{x}(\mathrm{e}^{\mathrm{j}\omega}), \tag{4.17}$$

such that the signals $\mathbf{x}_{p}(\mathrm{e}^{\mathrm{j}\omega})$ are whitened and decorrelated.

The matrix $\boldsymbol{D}^{-\frac{1}{2}}(\mathrm{e}^{\mathrm{j}\omega})$ in Eq. (4.13) exists if the reference signals have non-zero frequency contents within the control bandwidth [53]. To improve the conditioning of the matrix $\boldsymbol{D}(\mathrm{e}^{\mathrm{j}\omega})$, regularization is applied

$$\bar{\boldsymbol{D}}(\mathrm{e}^{\mathrm{j}\omega}) = \boldsymbol{D}(\mathrm{e}^{\mathrm{j}\omega}) + \beta_{F_{w}}\boldsymbol{I}_{K}, \tag{4.18}$$

where $\boldsymbol{I}_{K} \in \mathbb{R}^{K\times K}$ is an identity matrix, with the regularization parameter $\beta_{F_{w}}$. The regularization procedure decreases the condition number of the matrix. The regularized filter is defined as

$$\bar{\boldsymbol{F}}_{w}(\mathrm{e}^{\mathrm{j}\omega}) = \bar{\boldsymbol{D}}^{-\frac{1}{2}}(\mathrm{e}^{\mathrm{j}\omega})\boldsymbol{Q}^{H}(\mathrm{e}^{\mathrm{j}\omega}). \tag{4.19}$$

At this point a regularized prewhitening filter is obtained which, when applied to the reference signals, reduces the effects of colouring and correlation and therefore improves the speed of convergence. However, the prewhitening filter is formulated in the frequency domain, which for practical implementation needs to be converted to the time domain. The procedure for this conversion is described in Sec. 4.2.3. The next section describes the frequency domain formulation of the preconditioning and decoupling filters, which also improves convergence speed.

4.2.2 Frequency domain formulation of the system's preconditioning and decoupling filters

To further improve the convergence speed of the algorithm, system preconditioning and decoupling filters are applied. Because a system matrix is possibly non-square and in general not Hermitian [53], a singular value decomposition (SVD) is used instead of the EVD to decouple the system. Assuming that a stable MIMO linear time-invariant system is described by the frequency response matrix $\boldsymbol{G}(\mathrm{e}^{\mathrm{j}\omega})$, this matrix is extended with a regularized transfer function matrix [54], written as

$$\bar{\boldsymbol{G}}(\mathrm{e}^{\mathrm{j}\omega}) = \begin{bmatrix} \boldsymbol{G}(\mathrm{e}^{\mathrm{j}\omega}) \\ \boldsymbol{G}_{\mathrm{reg}}(\mathrm{e}^{\mathrm{j}\omega}) \end{bmatrix} \in \mathbb{C}^{(L+M)\times M}, \tag{4.20}$$

in which the regularizing transfer function is defined as

$$\boldsymbol{G}_{\text{reg}}(\mathrm{e}^{\mathrm{j}\omega}) = \sqrt{\beta_G}\boldsymbol{I}_M, \tag{4.21}$$

and β_G is the regularization parameter. The regularization with parameter β_G prevents high gains in $\hat{\bar{\boldsymbol{G}}}_{\text{mi}}$ that might occur due to the inverse operation, and therefore prevents saturation of the control signal [54]. This parameter is usually chosen in the range of expected reduction levels in dB.

Decoupling of the regularized system matrix in Eq. (4.20) by the SVD at each frequency results in

$$\bar{\boldsymbol{G}}(\mathrm{e}^{\mathrm{j}\omega}) = \bar{\boldsymbol{U}}(\mathrm{e}^{\mathrm{j}\omega})\bar{\boldsymbol{\Sigma}}(\mathrm{e}^{\mathrm{j}\omega})\bar{\boldsymbol{V}}^H(\mathrm{e}^{\mathrm{j}\omega}), \tag{4.22}$$

in which $\bar{\boldsymbol{U}}(\mathrm{e}^{\mathrm{j}\omega}) \in \mathbb{C}^{(L+M)\times M}$ are the left singular vectors, $\bar{\boldsymbol{\Sigma}}(\mathrm{e}^{\mathrm{j}\omega}) \in \mathbb{C}^{M\times M}$ is the matrix containing the singular values and $\bar{\boldsymbol{V}}^H(\mathrm{e}^{\mathrm{j}\omega}) \in \mathbb{C}^{M\times M}$ are the right singular vectors.

The preconditioner is applied to the plant to improve convergence speed by compensating for the dynamic response of the plant [156]. The preconditioner in the direct path is written as

$$\bar{\boldsymbol{G}}_{\text{mi}}(\mathrm{e}^{\mathrm{j}\omega}) = \bar{\boldsymbol{V}}(\mathrm{e}^{\mathrm{j}\omega})\bar{\boldsymbol{\Sigma}}^{-1}(\mathrm{e}^{\mathrm{j}\omega}), \tag{4.23}$$

which results in the preconditioned direct path

$$\begin{aligned}\bar{\boldsymbol{G}}(\mathrm{e}^{\mathrm{j}\omega})\bar{\boldsymbol{G}}_{\text{mi}}(\mathrm{e}^{\mathrm{j}\omega}) = \\ \bar{\boldsymbol{U}}(\mathrm{e}^{\mathrm{j}\omega})\bar{\boldsymbol{\Sigma}}(\mathrm{e}^{\mathrm{j}\omega})\bar{\boldsymbol{V}}^H(\mathrm{e}^{\mathrm{j}\omega})\bar{\boldsymbol{V}}(\mathrm{e}^{\mathrm{j}\omega})\bar{\boldsymbol{\Sigma}}^{-1}(\mathrm{e}^{\mathrm{j}\omega}) = \\ \bar{\boldsymbol{U}}(\mathrm{e}^{\mathrm{j}\omega}).\end{aligned} \tag{4.24}$$

The decoupling of the regularized system $\bar{\boldsymbol{G}}(\mathrm{e}^{\mathrm{j}\omega})$ is achieved by choosing

$$\bar{\boldsymbol{G}}_{\text{ai}}(\mathrm{e}^{\mathrm{j}\omega}) = \bar{\boldsymbol{U}}^H(\mathrm{e}^{\mathrm{j}\omega}), \tag{4.25}$$

which, together with the preconditioning filter, results in

$$\bar{\boldsymbol{G}}_{\text{ai}}(\mathrm{e}^{\mathrm{j}\omega})\bar{\boldsymbol{G}}(\mathrm{e}^{\mathrm{j}\omega})\bar{\boldsymbol{G}}_{\text{mi}}(\mathrm{e}^{\mathrm{j}\omega}) = \bar{\boldsymbol{U}}^H(\mathrm{e}^{\mathrm{j}\omega})\bar{\boldsymbol{U}}(\mathrm{e}^{\mathrm{j}\omega}) = \tilde{\boldsymbol{I}}. \tag{4.26}$$

This shows that the system is diagonalized and thus decoupled. The benefit of the decoupled system is that the cross-coupling between the individual paths in the plant response is removed, which improves convergence speed [53].

4.2.3 Time domain formulation of the frequency domain filters

In order to causally implement the filters into the scheme of Fig. 4.1, the filters need to be converted from the frequency domain to the time domain. The frequency response matrices can be converted to impulse response matrices using the inverse discrete-time Fourier transform. However, the discrete Fourier transform could introduce wrap-around effects, and together with the truncation effects this might result in non-causality of the time domain filters. Therefore, causality of the filters must be ensured by introducing appropriate delay and truncation procedures.

The frequency response matrix of the prewhitening filter $\bar{\boldsymbol{F}}_w(\mathrm{e}^{\mathrm{j}\omega})$ is transformed to the impulse response matrix $\bar{\boldsymbol{F}}_w(z)$, with reference to the symmetry property of the frequency response matrix $\bar{\boldsymbol{F}}_w(\mathrm{e}^{-\mathrm{j}\omega}) = \bar{\boldsymbol{F}}_w^*(\mathrm{e}^{\mathrm{j}\omega})$, in which the superscript $(\cdot)^*$ denotes the complex conjugate. The obtained impulse response matrix $\bar{\boldsymbol{F}}_w(z)$ is not necessarily causal, and therefore an appropriate number of sample delays denoted by Δ_F is added, to ensure that the non-causal part of the filter has been shifted to positive time for all entries of the impulse response matrix. This results in the new impulse response matrix $\tilde{\bar{\boldsymbol{F}}}_w(z)$. Lastly the non-causal part of $\tilde{\bar{\boldsymbol{F}}}_w(z)$ is truncated to obtain the coefficients of FIR filters $\hat{\bar{\boldsymbol{F}}}_w(z)$ of length O.

A similar procedure is necessary for the preconditioning and decoupling filters. The frequency response matrices $\bar{\boldsymbol{G}}_{\mathrm{mi}}(\mathrm{e}^{\mathrm{j}\omega})$ and $\bar{\boldsymbol{G}}_{\mathrm{ai}}(\mathrm{e}^{\mathrm{j}\omega})$ are converted to the impulse response matrices $\bar{\boldsymbol{G}}_{\mathrm{mi}}(z)$ and $\bar{\boldsymbol{G}}_{\mathrm{ai}}(z)$ by taking the inverse discrete Fourier transform, with reference to the symmetry property of the frequency response matrices: $\bar{\boldsymbol{G}}_{\mathrm{mi}}(\mathrm{e}^{-\mathrm{j}\omega}) = \bar{\boldsymbol{G}}_{\mathrm{mi}}^*(\mathrm{e}^{\mathrm{j}\omega})$ and $\bar{\boldsymbol{G}}_{\mathrm{ai}}(\mathrm{e}^{-\mathrm{j}\omega}) = \bar{\boldsymbol{G}}_{\mathrm{ai}}^*(\mathrm{e}^{\mathrm{j}\omega})$. To shift the non-causal part of $\bar{\boldsymbol{G}}_{\mathrm{mi}}(\mathrm{e}^{-\mathrm{j}\omega}) = \bar{\boldsymbol{G}}_{\mathrm{mi}}^*(\mathrm{e}^{\mathrm{j}\omega})$ to positive time, a delay of Δ_{mi} samples is added to obtain $\tilde{\bar{\boldsymbol{G}}}_{\mathrm{mi}}(z)$. The delay Δ_{mi} is incorporated in $\bar{\boldsymbol{G}}_{\mathrm{ai}}(z)$ but time-reversed, since it is based on the adjoint and on the Hermitian in the frequency domain of the product $\bar{\boldsymbol{G}}(\mathrm{e}^{\mathrm{j}\omega})\bar{\boldsymbol{G}}_{\mathrm{mi}}(\mathrm{e}^{\mathrm{j}\omega})$. Thereafter, $\bar{\boldsymbol{G}}_{\mathrm{ai}}(z)$ is delayed by Δ_{ai} samples to shift its non-causal part to positive time. Therefore, the procedure for both filters can be written as

$$\begin{aligned} \tilde{\bar{\boldsymbol{G}}}_{\mathrm{mi}}(z) &= \Delta_{\mathrm{mi}}(z)\bar{\boldsymbol{G}}_{\mathrm{mi}}(z), \\ \tilde{\bar{\boldsymbol{G}}}_{\mathrm{ai}}(z) &= \Delta_{\mathrm{ai}}(z)\Delta_{\mathrm{mi}}^{-}(z)\bar{\boldsymbol{G}}_{\mathrm{ai}}(z), \end{aligned} \tag{4.27}$$

in which $\Delta_{\mathrm{mi}}^{-}(z)$ represents a negative delay. Lastly, the non-causal parts of $\tilde{\bar{\boldsymbol{G}}}_{\mathrm{mi}}(z)$ and $\tilde{\bar{\boldsymbol{G}}}_{\mathrm{ai}}(z)$ are truncated to obtain the coefficients of the FIR filters $\hat{\bar{\boldsymbol{G}}}_{\mathrm{mi}}(z)$ and $\hat{\bar{\boldsymbol{G}}}_{\mathrm{ai}}(z)$ of length J.

4.3 The conjugate gradient scheme with block-circulant preconditioning in the time domain

The FD-RMFE algorithm in the previous section is equipped with filters computed in the frequency domain. Delays are introduced in these filters to ensure their causality. However, this gives rise to a lot of adjustable parameters. Furthermore, owing to the delays in the filters of the direct path, more time advance on the reference signals may be required. In this section, an algorithm that applies CG updates is derived with significantly less adjustable parameters and without artificial delays. The algorithm presented in this section computes the set of optimal control filters as described in Sec. 2.2.4, which is the starting point of the derivation of the algorithm. The speed of convergence of the CG algorithm is improved by applying a block-circulant preconditioning method which is given in [140], resulting in the PCG algorithm. This section derives a modified version of the PCG algorithm in which regularization is incorporated. The regularization is needed to maintain control stability in systems with IMC and therefore allows practical implementation in

The algorithm derived in this section is published in [149].

an AAC to suppress the reflections. The result is the preconditioned block-circulant conjugate gradient scheme, abbreviated PBC-CG, which is further referred to in the remainder of the thesis. The derivation starts with the block diagram of a feedforward active noise control system which is shown in Fig. 2.2. To find the optimal set of control filters, the cost function is written as the expectation of the sum of the squared error signals

$$\mathcal{J} = \sum_{p=1}^{P} \mathrm{E}\left[\mathbf{e}_p^T(n)\mathbf{e}_p(n)\right], \tag{4.28}$$

in which the subscript p denotes the dependence on a primary source. The optimal set of control filters is found by taking the derivative of the cost function with respect to the control filters, such that

$$\frac{\partial \mathcal{J}}{\partial \boldsymbol{W}} = 2\sum_{p=1}^{P} \mathrm{E}\left[\boldsymbol{R}_p^T(n)\boldsymbol{R}_p(n)\right]\boldsymbol{W} + 2\sum_{p=1}^{P} \mathrm{E}\left[\boldsymbol{R}_p^T(n)\mathbf{d}_p(n)\right] = 0, \tag{4.29}$$

holds. As described in Sec. 2.2.4, the previous equation can be solved by computing

$$\boldsymbol{W}_{\text{opt}} = -\sum_{p=1}^{P} \mathrm{E}\left[\boldsymbol{R}_p^T(n)\boldsymbol{R}_p(n)\right]^{-1} \sum_{p=1}^{P} \mathrm{E}\left[\boldsymbol{R}_p^T(n)\mathbf{d}_p(n)\right], \tag{4.30}$$

for multiple primary sources P. However, instead of computing the direct inverse shown in the first term in Eq. (4.30), which is computationally expensive and memory consuming, following [139], an iterative procedure with regularization is used. Let $\boldsymbol{W}_k$ be the approximation of $\boldsymbol{W}$ at iteration k, and let the residual be given as

$$\boldsymbol{R}_k = \boldsymbol{b} - \boldsymbol{T}_B\boldsymbol{W}_k, \tag{4.31}$$

in which

$$\boldsymbol{T}_B = \sum_{p=1}^{P} \mathrm{E}\left[\boldsymbol{R}_p^T(n)\boldsymbol{R}_p(n)\right] + \beta\boldsymbol{I}, \tag{4.32}$$

$$\boldsymbol{b} = \sum_{p=1}^{P} \mathrm{E}\left[\boldsymbol{R}_p^T(n)\mathbf{d}_p(n)\right]. \tag{4.33}$$

Note that in Eq. (4.32) β has been introduced as an optional regularization parameter. The matrix in Eq. (4.32) has a Toeplitz-block structure [124] in the case of a system with multiple secondary sources M and multiple reference sensors K [44]. This matrix is structured as

$$\boldsymbol{T}_B = \begin{bmatrix} \boldsymbol{T}_{11} & \boldsymbol{T}_{12} & \dots & \boldsymbol{T}_{1N} \\ \boldsymbol{T}_{21} & \ddots & & \vdots \\ \vdots & & & \\ \boldsymbol{T}_{N1} & \dots & \dots & \boldsymbol{T}_{NN} \end{bmatrix}, \tag{4.34}$$

in which $N = MK$ and each block $\boldsymbol{T}_{ij}$ has size I-by-I. Typically, the matrix $\boldsymbol{T}_B$ is of dimensions MKI-by-MKI. However, each block $\boldsymbol{T}_{ij}$ is fully defined by the first

element of each row and column. Therefore, the matrix $\boldsymbol{T}_B$ can be stored using $(2I-1)M^2K^2$ elements. With the equation of the residual (Eq. (4.31)), the update of the controller matrix $\boldsymbol{W}_k$ is defined by

$$\boldsymbol{W}_k = \boldsymbol{W}_{k-1} + \alpha_k \boldsymbol{p}_k, \tag{4.35}$$

in which α_k is a scalar quantity that defines the orthogonal steepest-descent directions. These directions are written as [157]

$$\alpha_k = \frac{\boldsymbol{R}_{k-1}^T \boldsymbol{z}_{k-1}}{\boldsymbol{p}_k^T \boldsymbol{v}_k}, \tag{4.36}$$

with

$$\boldsymbol{v}_k = \boldsymbol{T}_B \boldsymbol{p}_k. \tag{4.37}$$

The last equation can be computed efficiently using a circulant representation. Any Toeplitz matrix $\boldsymbol{T} \in \mathbb{R}^{n\times n}$ can be embedded into a $2n$-by-$2n$ circulant matrix following [139], such that

$$\underbrace{\begin{bmatrix} \boldsymbol{T} & \times \\ \times & \boldsymbol{T} \end{bmatrix}}_{\boldsymbol{C}} \begin{bmatrix} \boldsymbol{p} \\ \boldsymbol{0} \end{bmatrix} = \begin{bmatrix} \boldsymbol{T}\boldsymbol{p} \\ \dagger \end{bmatrix}, \tag{4.38}$$

holds. Here $\boldsymbol{C} \in \mathbb{R}^{2n\times 2n}$ is a circulant matrix, that can be diagonalized by the Fourier matrix $\boldsymbol{\mathcal{F}}$, following

$$\boldsymbol{C} = \boldsymbol{\mathcal{F}}^H \boldsymbol{\Lambda} \boldsymbol{\mathcal{F}}, \tag{4.39}$$

in which $\boldsymbol{\Lambda}$ is the eigenvalue matrix of $\boldsymbol{C}$ [139]. This technique can also be applied in the Toeplitz-block case. The matrix $\boldsymbol{T}_B$ is embedded into a block circulant matrix $\boldsymbol{C}_n \in \mathbb{R}^{2N\times 2N}$, in which each block itself is a $2I$-by-$2I$ circulant matrix. The vector $\boldsymbol{p}_k$ is extended to a $4IN$-vector by putting zeros in the appropriate places. Then the solution can efficiently be obtained using FFTs [139]. Substitution of Eq. (4.35) into Eq. (4.31) and using Eq. (4.37) leads to

$$\boldsymbol{R}_k = \boldsymbol{R}_{k-1} - \alpha_k \boldsymbol{v}_k. \tag{4.40}$$

The PCG directions are given by [157]

$$\boldsymbol{p}_k = \begin{cases} \boldsymbol{z}_{k-1}, & k = 1, \\ \boldsymbol{z}_{k-1} + \beta_k \boldsymbol{p}_k, & k > 1, \end{cases} \tag{4.41}$$

in which

$$\beta_k = \frac{\boldsymbol{R}_{k-1}^T \boldsymbol{z}_{k-1}}{\boldsymbol{R}_{k-2}^T \boldsymbol{z}_{k-2}}, \tag{4.42}$$

and $\boldsymbol{z}_k$ is computed by solving

$$\mathrm{circ}^1(\boldsymbol{T}_B)\boldsymbol{z}_k = \boldsymbol{R}_k, \tag{4.43}$$

in which $\text{circ}^1(\boldsymbol{T}_B)$ is the preconditioner, a block circulant approximation to each individual block in the Toeplitz matrix [140]. This preconditioner is computed as the solution to the following optimization problem:

$$\min_{\boldsymbol{C}} \|\boldsymbol{C} - \boldsymbol{A}\|_F, \tag{4.44}$$

in which the subscript $(\cdot)_F$ denotes the Frobenius norm, $\boldsymbol{C}$ denotes the preconditioning matrix and $\boldsymbol{A}$ denotes any general matrix. This minimization problem applies to any general matrix $\boldsymbol{A}$, but in the case of a Toeplitz matrix $\boldsymbol{T}$, the entries of the preconditioner are given by [140]

$$c_i = \frac{it_{m-i} + (m-i)t_i}{m}, \quad i = \pm 1, \ldots, \pm(m-1), \tag{4.45}$$

in which t denotes an entry of the Toeplitz matrix $\boldsymbol{T}$ and m denotes the size of the Toeplitz matrix. This preconditioning technique is extended to the Toeplitz-block case, in which the preconditioning approach is applied to each individual block in the Toeplitz-block matrix. This then leads to

$$\text{circ}^1(\boldsymbol{T}_B) = \begin{bmatrix} \text{circ}(\boldsymbol{T}_{11}) & \text{circ}(\boldsymbol{T}_{12}) & \ldots & \text{circ}(\boldsymbol{T}_{1N}) \\ \text{circ}(\boldsymbol{T}_{21}) & \ddots & & \vdots \\ \vdots & & & \\ \text{circ}(\boldsymbol{T}_{N1}) & \ldots & \ldots & \text{circ}(\boldsymbol{T}_{NN}) \end{bmatrix}, \tag{4.46}$$

in which $\text{circ}(\cdot)$ denotes the circulant preconditioner as defined in Eq. (4.45). At each iteration of the PCG, Eq. (4.43) must be solved. Similar to computing Eq. (4.37), Eq. (4.43) can be solved efficiently using FFTs. Each block $\text{circ}(\boldsymbol{T}_{ij})$ is circulant, so that

$$\text{circ}(\boldsymbol{T}_{ij}) = \boldsymbol{\mathcal{F}}^H \boldsymbol{\Lambda}_{ij} \boldsymbol{\mathcal{F}}. \tag{4.47}$$

Let $\tilde{\boldsymbol{\mathcal{F}}} = \boldsymbol{I} \otimes \boldsymbol{\mathcal{F}}$ be a block diagonal matrix with the Fourier matrix $\boldsymbol{\mathcal{F}}$ repeated along the diagonal. By defining $\boldsymbol{P}$ as the permutation matrix that satisfies

$$(\boldsymbol{P}^* \boldsymbol{T}_{mn} \boldsymbol{P})_{k,l;i,j} = (\boldsymbol{T}_{mn})_{i,j;k,l}, \tag{4.48}$$

for $1 \leq i, j \leq n$, $1 \leq k, l \leq m$, and by defining the dense matrix $\boldsymbol{D}_m \in \mathbb{R}^{N \times N}$ as

$$(\boldsymbol{D}_m)_{ij} = \left(\boldsymbol{\Lambda}_{ij}\right)_m, \tag{4.49}$$

then Eq. (4.43) is solved by computing [140]

$$\boldsymbol{z}_k = \tilde{\boldsymbol{\mathcal{F}}}^H \left\{ \boldsymbol{P}^T \left[\text{diag}(\boldsymbol{D}_1^{-1}, \ldots, \boldsymbol{D}_I^{-1}) \left(\boldsymbol{P} \left(\tilde{\boldsymbol{\mathcal{F}}} \boldsymbol{R}_k \right) \right) \right] \right\}. \tag{4.50}$$

The algorithm is terminated as soon as the maximum number of iterations is reached, or if the relative tolerance is achieved, written as

$$\left| \frac{\boldsymbol{R}_k^T \boldsymbol{R}_k}{\boldsymbol{R}_0^T \boldsymbol{R}_0} \right| < \epsilon, \tag{4.51}$$

in which ϵ is the relative tolerance parameter.

The algorithm has a before-solving cost of $(MK)^2I + (MK)^2 \cdot FFT(I) + (MK)^3I/3$, with a per-iteration cost of $(MK)^2I + 2MK \cdot FFT(I)$, and $FFT(I)$ being the cost of a Fourier transform applied on a vector of length I. It should be noted that another level of preconditioning ($\text{circ}_F^2(\boldsymbol{T}_B)$) could be applied to reduce the before solving cost to $(MK)^2I + (MK)^2 \cdot FFT(I) + MKI + I \cdot FFT(MK)$ and the per-iteration cost to $MKI + 2I \cdot FFT(MK) + 2MK \cdot FFT(I)$. However, after application of the first level of the preconditioner, the block matrices in matrix $\text{circ}_F^1(\boldsymbol{T}_B)$ are generally not Toeplitz, and circulant approximations which are defined only for Toeplitz matrices cannot be used for the second level of approximation [140]. Therefore a circulant approximation of the block matrices in matrix $\text{circ}_F^1(\boldsymbol{T}_B)$ is required. Because of the two levels of approximation, using $\text{circ}_F^2(\boldsymbol{T}_B)$ may require more iterations than using $\text{circ}_F^1(\boldsymbol{T}_B)$ [140].

4.4 The causally constrained conjugate gradient scheme in the frequency domain

In the previous section the PBC-CG algorithm which applies CG updates in the time domain is derived. However, this algorithm still has a relatively high computational complexity and memory consumption. In this section, an algorithm is derived that also applies CG updates to adapt the filter coefficients, but in this case in the frequency domain. This significantly reduces the computational complexity and memory consumption. Because of the frequency domain computations, a causal constraint is applied to the control filter coefficient updates to ensure a causal set of filter coefficients. The derivation in this section uses the equations and the definition of the causality brackets as introduced in Sec. 2.2.8, but the frequency domain is used instead of the z-domain. The computational complexity is significantly reduced with the frequency domain computations, while causal time domain control coefficients are obtained by using the causality constraint in the control coefficients update. This results in the causally constrained conjugate gradient frequency domain scheme, abbreviated CC-CG in the remainder of the thesis.

The derivation starts from the block diagram of a time domain fixed-gain feedforward control scheme as shown in Fig. 2.2. The objective is to design a fixed-gain controller $\boldsymbol{W}(z)$ by minimizing the cost function with respect to the control coefficients. The cost function, which is defined as the expectation of the sum of the squared error signals, is written as

$$\mathcal{J} = \sum_{p=1}^{P} \text{tr.E}\left[\mathbf{e}_p(n)\mathbf{e}_p^T(n)\right]. \tag{4.52}$$

Similar to [44], the derivative of the cost function with respect to the i-th matrix of control filter coefficients $\boldsymbol{W}_i$ is written as

$$\nabla_i = \frac{\partial \mathcal{J}}{\partial \mathbf{W}_i} = 2\sum_{j=0}^{J-1} \mathbf{G}_j^T \mathbf{R}_{\text{xe}}(i+j), \tag{4.53}$$

The algorithm derived in this section is submitted in [150].

in which

$$\boldsymbol{R}_{\mathrm{xe}}(m) = \sum_{p=1}^{P} \mathrm{E}\left[\mathbf{e}_p(n+m)\mathbf{x}_p^T(n)\right], \tag{4.54}$$

is the matrix of cross-correlation functions between each error signal and each reference signal. In [44] it is shown that the gradient in Eq. (4.53) can be evaluated in the frequency domain, taking causality into account. In the frequency domain, the causal gradient becomes

$$\begin{aligned}\left\{\nabla(\mathrm{e}^{\mathrm{j}\omega})\right\}_+ &= \left\{\frac{\partial\mathcal{J}}{\partial\mathcal{R}(\boldsymbol{W}(\mathrm{e}^{\mathrm{j}\omega}))} + \mathrm{j}\frac{\partial\mathcal{J}}{\partial\mathcal{I}(\boldsymbol{W}(\mathrm{e}^{\mathrm{j}\omega}))}\right\}_+, \\ &= 2\left\{\boldsymbol{G}^H(\mathrm{e}^{\mathrm{j}\omega})\boldsymbol{S}_{\mathrm{xe}}(\mathrm{e}^{\mathrm{j}\omega})\right\}_+,\end{aligned} \tag{4.55}$$

in which $\boldsymbol{S}_{\mathrm{xe}}(\mathrm{e}^{\mathrm{j}\omega})$ is the spectral density matrix between the error signals and reference signals, written as

$$\boldsymbol{S}_{\mathrm{xe}}(\mathrm{e}^{\mathrm{j}\omega}) = \sum_{p=1}^{P} \mathrm{E}\left[\mathbf{E}_p(\mathrm{e}^{\mathrm{j}\omega})\mathbf{X}_p^H(\mathrm{e}^{\mathrm{j}\omega})\right]. \tag{4.56}$$

The use of the causality brackets in the frequency domain implies that a transformation to the time domain has been made, which allows truncation of the non-causal part, followed by a transformation back to the frequency domain.

An iterative CG scheme similar to that of [158] is assumed to minimize $\mathcal{J}$, in which $\mathbf{E}_p(\mathrm{e}^{\mathrm{j}\omega}) \in \mathcal{C}^{L\times 1}$ is approximated by $\mathbf{E}_{k,p}(\mathrm{e}^{\mathrm{j}\omega}) \in \mathcal{C}^{L\times 1}$ at iteration k. The frequency domain representation of Eq. (2.73) [44] with primary source dependence p at iteration k is written as

$$\mathbf{E}_{k,p}(\mathrm{e}^{\mathrm{j}\omega}) = \mathbf{D}_p(\mathrm{e}^{\mathrm{j}\omega}) + \boldsymbol{G}(\mathrm{e}^{\mathrm{j}\omega})\boldsymbol{W}_k(\mathrm{e}^{\mathrm{j}\omega})\mathbf{X}_p(\mathrm{e}^{\mathrm{j}\omega}), \tag{4.57}$$

in which $\boldsymbol{W}_k(\mathrm{e}^{\mathrm{j}\omega})$ is the set of control coefficients at iteration k. The cost function $\mathcal{J}_k$ at iteration k is evaluated as an integral in the frequency domain:

$$\mathcal{J}_k = \mathrm{tr.}\int \sum_{p=1}^{P} \mathrm{E}\left[\mathbf{E}_{k,p}(\mathrm{e}^{\mathrm{j}\omega})\mathbf{E}_{k,p}^H(\mathrm{e}^{\mathrm{j}\omega})\right]\mathrm{d}\omega. \tag{4.58}$$

The update of the controller coefficients is written as

$$\boldsymbol{W}_k(\mathrm{e}^{\mathrm{j}\omega}) = \boldsymbol{W}_{k-1}(\mathrm{e}^{\mathrm{j}\omega}) + \eta_k\boldsymbol{C}_k(\mathrm{e}^{\mathrm{j}\omega}), \tag{4.59}$$

in which η_k is a variational parameter and $\boldsymbol{C}_k(\mathrm{e}^{\mathrm{j}\omega})$ are the search directions. Substitution of Eq. (4.59) into Eq. (4.57) results in

$$\boldsymbol{E}_{k,p}(\mathrm{e}^{\mathrm{j}\omega}) = \mathbf{E}_{k-1,p}(\mathrm{e}^{\mathrm{j}\omega}) - \eta_k\mathbf{r}_{k,p}(\mathrm{e}^{\mathrm{j}\omega}), \tag{4.60}$$

in which

$$\mathbf{r}_{k,p}(\mathrm{e}^{\mathrm{j}\omega}) = -\boldsymbol{G}(\mathrm{e}^{\mathrm{j}\omega})\boldsymbol{C}_k(\mathrm{e}^{\mathrm{j}\omega})\mathbf{X}_p(\mathrm{e}^{\mathrm{j}\omega}). \tag{4.61}$$

Upon substitution of Eq. (4.60) into Eq. (4.58), the cost function $\mathcal{J}_k$ is written as

$$\mathcal{J}_k = \text{tr.} \int \sum_{p=1}^{P} \text{E}\left[(\mathbf{E}_{k-1,p}(\text{e}^{\text{j}\omega}) - \eta_k \mathbf{r}_{k,p}(\text{e}^{\text{j}\omega}))(\mathbf{E}_{k-1,p}(\text{e}^{\text{j}\omega}) - \eta_k \mathbf{r}_{k,p}(\text{e}^{\text{j}\omega}))^H\right] \text{d}\omega, \tag{4.62}$$

which is rewritten as

$$\mathcal{J}_k = \mathcal{J}_{k-1} - 2\Re\left(\eta_k \text{tr.} \int \sum_{p=1}^{P} \text{E}\left[\mathbf{r}_{k,p}(\text{e}^{\text{j}\omega})\mathbf{E}_{k-1,p}^H(\text{e}^{\text{j}\omega})\right] \text{d}\omega\right) + |\eta_k|^2 \text{tr.} \int \sum_{p=1}^{P} \text{E}\left[\mathbf{r}_{k,p}(\text{e}^{\text{j}\omega})\mathbf{r}_{k,p}^H(\text{e}^{\text{j}\omega})\right] \text{d}\omega. \tag{4.63}$$

The previous equation can be written as

$$\mathcal{J}_k = \mathcal{J}_{k-1} - 2\Re(\eta_k A_k) + |\eta_k|^2 B_k, \tag{4.64}$$

in which

$$B_k = \text{tr.} \int \sum_{p=1}^{P} \text{E}\left[\mathbf{r}_{k,p}(\text{e}^{\text{j}\omega})\mathbf{r}_{k,p}^H(\text{e}^{\text{j}\omega})\right] \text{d}\omega, \tag{4.65}$$

and

$$A_k = \text{tr.} \int \sum_{p=1}^{P} \text{E}\left[\mathbf{r}_{k,p}(\text{e}^{\text{j}\omega})\mathbf{E}_{k-1,p}^H(\text{e}^{\text{j}\omega})\right] \text{d}\omega. \tag{4.66}$$

For the search directions, the CG directions are taken [157], written as

$$\boldsymbol{C}_k(\text{e}^{\text{j}\omega}) = \begin{cases} -\left\{\nabla_{k-1}(\text{e}^{\text{j}\omega})\right\}_+, & k = 1, \\ -\left\{\nabla_{k-1}(\text{e}^{\text{j}\omega})\right\}_+ + \frac{A_k}{A_{k-1}} \boldsymbol{C}_{k-1}(\text{e}^{\text{j}\omega}), & k > 1, \end{cases} \tag{4.67}$$

in which

$$\left\{\nabla_k(\text{e}^{\text{j}\omega})\right\}_+ = 2\left\{\boldsymbol{G}^H(\text{e}^{\text{j}\omega})\boldsymbol{S}_{\text{xe},k}(\text{e}^{\text{j}\omega})\right\}_+, \tag{4.68}$$

and

$$\boldsymbol{S}_{\text{xe},k}(\text{e}^{\text{j}\omega}) = \sum_{p=1}^{P} \text{E}\left[\mathbf{E}_{k,p}(\text{e}^{\text{j}\omega})\mathbf{X}_p^H(\text{e}^{\text{j}\omega})\right]. \tag{4.69}$$

By following [158] and [153], with substitution of Eq. (4.67) and Eq. (4.61), the scalar A_k, can be rewritten as

$$A_k = \text{tr.} \int \left\{\nabla_{k-1}(\text{e}^{\text{j}\omega})\right\}_+ \left[\left\{\nabla_{k-1}(\text{e}^{\text{j}\omega})\right\}_+\right]^H \text{d}\omega, \tag{4.70}$$

using the cyclic property of the trace operator. Because of the inner product in Eq. (4.70), A_k is always real, thus the cost function can be rewritten as

$$\mathcal{J}_k = \mathcal{J}_{k-1} - \frac{|A_k|^2}{B_k} + \left|\eta_k - \frac{A_k}{B_k}\right|^2 B_k, \tag{4.71}$$

which, as a function of η_k, has a minimum at

$$\eta_k = \frac{A_k}{B_k}. \tag{4.72}$$

The advantage of this scheme is that all MIMO convolutions are computed as matrix multiplications in the frequency domain, which can be computed very efficiently, while causality is enforced through a constraint applied to the gradient. The causality constraint is computed with forward and inverse FFTs, which are relatively efficient. Therefore, the CC-CG scheme is completely causal, as can be seen in Eq. (4.67), because every control coefficient update is a combination of the previous causal updates and the causal part of the gradient. Alternatively, the update equation for the control coefficients (Eq. (4.59)) and the CG directions (Eq. (4.67)) can also be computed in the time domain.

4.5 Comparing the algorithms

In this section, the algorithms that are derived in this chapter are compared. First a table with the computational complexities and memory consumption is shown in Table. 4.1. A graph of the computational complexity with respect to the number of sources and sensors $K = L = M = P$ is shown in Fig. 4.2. It should be noted that for the PBC-CG algorithm, just one level of preconditioning is considered. By using two levels of preconditioning the before solving and per-iteration cost are reduced, but may require more iterations, as described in Sec. 4.3. From the figure can be seen that in general the CC-CG algorithm has the lowest computational complexity. However, from about $K = L = M = P = 500$ the FD-RMFE algorithm is preferred to the CC-CG algorithm in terms of computational complexity.

Table 4.1: Overview of the computational complexities and memory consumption of the algorithms derived in this chapter. The variable N_{freq} corresponds to the number of frequency bins in the frequency response matrices. The cost of a Fourier Transform applied on a vector of length n is denoted as $FFT(n)$.

	FD-RMFE	PBC-CG[1]	CC-CG
Before solving cost	$FFT(N_{\text{freq}})(K^2 + 3M^2 + 2LM) + FFT(n)K^2 + N_{\text{freq}}(K^2 + 3K^3 + 2M^2 + 3M^3 + LM + LM^2)$	$(MK)^2 I + (MK)^2 \cdot FFT(I) + (MK)^3 I/3$	None
Per-iteration cost	$OK^2 + 3MKI + JM^2 + 2J(L + M)M$	$(MK)^2 I + 2MK \cdot \text{FFT}(I)$	$N_{\text{freq}}(8KM + 4LP + KLM + KLP + KMP + LMP) + KM \cdot \text{FFT}(2N_{\text{freq}}) + 2KM \cdot \text{FFT}(N_{\text{freq}})$
Memory consumption	$OK^2 + MKI + JM^2 + 2J(L + M)M$	$(2I - 1)(MK)^2 + KMLI$	$N_{\text{freq}}(4MK + 2LP)$

A graph of the memory consumption is shown in Fig. 4.3. This figure shows that the memory consumption of the FD-RMFE and CC-CG algorithms is similar.

[1]The cost of this algorithm is shown by assuming that $\boldsymbol{T}_B$ and $\boldsymbol{b}$ as described in Sec. 4.3 are already available.

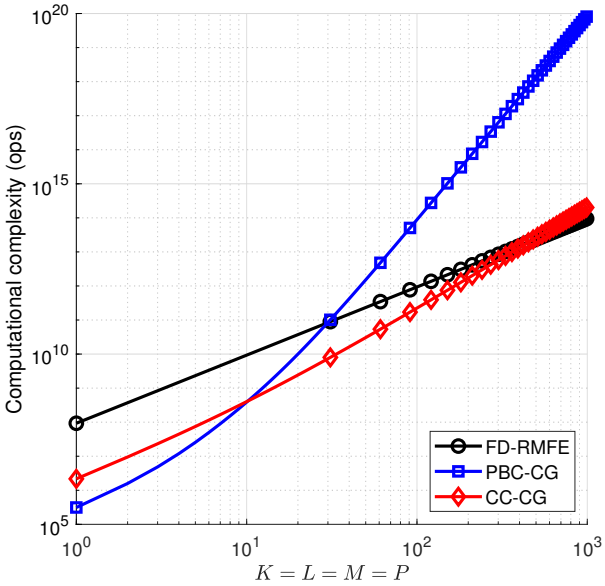

Figure 4.2: Computational complexity of the FD-RMFE algorithm (circles) compared to the PBC-CG algorithm (squares) and the CC-CG algorithm (diamonds). It is assumed that the solution is obtained within $n_{\text{FD-RMFE}} = 4e4$, $n_{\text{PBC-CG}} = 100$ and $n_{\text{CC-CG}} = 100$ iterations. Furthermore, it is assumed that $N_{\text{freq}} = 512$, $I = J = O = N_{\text{freq}}/2$ and an FFT cost of $n\log(n)$.

However, it can be seen that the PBC-CG algorithm has higher memory consumption than the other two algorithms. This is due mainly to the fact that the PBC-CG algorithm is computed in the time domain.

The computational complexity and memory consumption of the algorithms are, among other things, expressed in terms of the number of error sensors L, to have consistency with the literature. However, if the KHI is used, the number of error sensors L should be substituted by the number of performance sensors L_{perf}.

In general, the algorithm that is the easiest to work with is the PBC-CG algorithm. Although this is not the most efficient algorithm in terms of computational complexity and memory consumption, the fact that it is fully computed in the time domain relaxes some requirements in comparison with the algorithms that apply frequency domain computations. The FD-RMFE and the CC-CG algorithms compute at least a few operations in the frequency domain. Although this is favourable in terms of computational complexity and often also memory consumption, filters computed in the frequency domain may contain non-causal parts or frequency domain effects, due to wrap-around effects, truncation effects or ringing artifacts. Several factors influence the severity of these effects, for example the use of low-and high-pass filters including their corresponding order, the length of the impulse responses or the

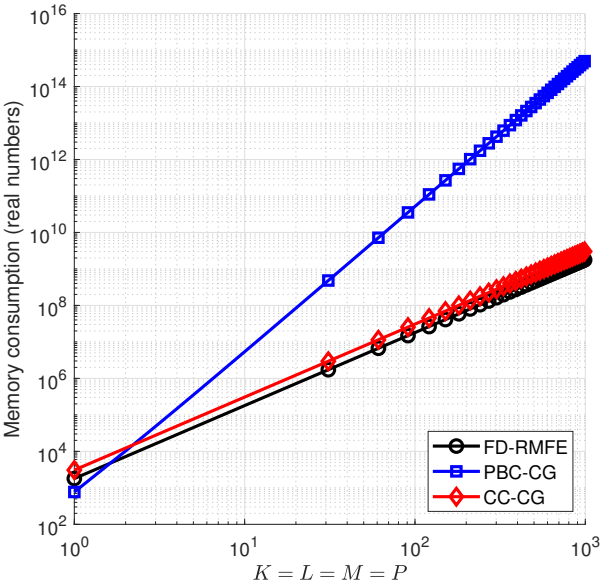

Figure 4.3: Memory consumption of the FD-RMFE algorithm (circles) compared to the PBC-CG algorithm (squares) and the CC-CG algorithm (diamonds).

amount of regularization [44]. Furthermore, especially the FD-RMFE algorithm requires some user-defined parameters such as the delays for each frequency domain derived filter. Therefore, the use of these two algorithms might not be as trivial as the PBC-CG algorithm.

4.6 Summary

This chapter describes three different algorithms with the objective of computing a set of control filters with a reduced computational complexity. In Sec. 4.2 the regularized modified filtered-error scheme (FD-RMFE) is derived, in which preconditioning and prewhitening filters are applied that are computed in the frequency domain. In Sec. 4.3 a regularized time domain conjugate gradient algorithm (PBC-CG) is derived in which block-circulant preconditioning is applied. In Sec. 4.4 a frequency domain conjugate gradient algorithm (CC-CG) is derived, which computes causal control coefficient updates. Lastly, in Sec. 4.5 the algorithms are compared in terms of computational complexity and memory consumption.

Chapter 5

Numerical results

5.1 Introduction

This chapter shows the numerical results of the developed methods as described in previous chapters. In Sec. 5.2 the KHI is verified for different source positions, the influence of the particle velocity approximation is studied and the effect of noise at the microphone is shown. The procedure for computing the reflected sound field with the finite element method (FEM) is shown, with an example, in Appendix A.1. In Sec. 5.3 a small-scale numerical study is shown in which the KHI is used to compute the reflected sound field, and the FD-RMFE algorithm (Sec. 4.2) is used to compute the control filter coefficients. Lastly, in Sec. 5.4 a large-scale numerical study is shown in which the KHI is used to compute the reflected sound field, and the CC-CG algorithm (Sec. 4.4) is used to compute the control filter coefficients.

5.2 Verification of the Kirchhoff-Helmholtz integral

In this section the results of the Kirchhoff-Helmholtz integral are verified. A comparison is made with the results computed with the FEM on two examples, one with a source within the contour and the other with a source outside the contour. Thereafter, an indication of the error introduced by the particle velocity estimation is given. Lastly, the effect of noise at the microphones on the contour is shown.

5.2.1 The Kirchhoff-Helmholtz integral with a source inside the contour

In this section the output of the KHI is compared with the reflected sound field computed with the FEM while an acoustic source is present within the contour. A two-dimensional configuration of dimensions 0.84-by-0.84 m^2 is used, to represent a small-scale AAC. The walls have an impedance of $z = 10\rho c$, with $\rho = 1.2$ $\mathrm{kg/m}^3$ and $c = 343$ $\mathrm{m/s}$. The monopole point source is located at $(x, y) = (0.05, -0.05)$. As described in Ch. 3, with a source located within the contour, the output of the KHI is the reflected sound field due to this source. The output of the KHI is therefore compared with the reflected sound field computed with the FEM. An example of

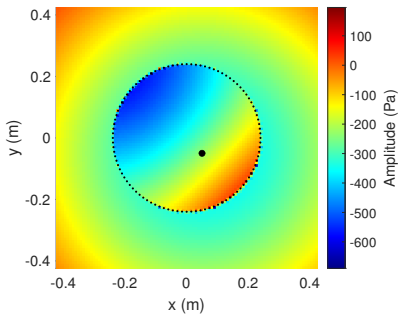

Figure 5.1: Real part of the output of the KHI at 201 Hz for a source inside the circle. The location of the source is indicated by the black dot. The result is valid only within the contour.

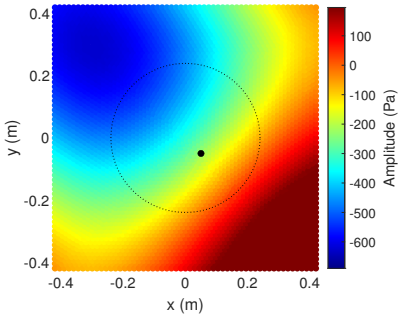

Figure 5.2: Real part of the reflected sound field computed with the FEM at 201 Hz. The location of the source is indicated by the black dot. The contour is shown for reference.

how to compute the reflected sound field with the FEM is shown in Appendix A.1. The reflected sound field is computed with the FEM, using a perfectly matched layer with a thickness of 0.33 m at the edges of the acoustic domain. The results of the FEM are obtained in COMSOL 6.2 with the Acoustics Module, using at least four quadratic elements per wavelength. The KHI is computed with Eq. (3.26), using the acoustic pressure and particle velocity computed with the FEM at 100 points on the circle with $r = 0.24$ m at the corresponding frequency.

The output of the KHI at 201 Hz is shown in Fig. 5.1. The result of the reflected sound field computed with the FEM at 201 Hz is shown in Fig. 5.2. Both figures show the acoustic pressure in Pa. It can be seen from these figures that within the contour the sound fields match, while outside the contour the sound fields differ, as the KHI is not valid outside the contour. The error between the output of the KHI and the reflected sound field computed with the FEM is computed as

$$\mathcal{E}(\mathbf{x},\omega) = 20\log_{10}\left(\frac{|p^{(2)}_{\mathrm{KHI}}(\mathbf{x},\omega) - p_{\mathrm{FEM}}(\mathbf{x},\omega)|}{|p^{(2)}_{\mathrm{KHI}}(\mathbf{x},\omega)|}\right), \tag{5.1}$$

in which $p^{(2)}_{\mathrm{KHI}}(\mathbf{x},\omega)$ is the output of the KHI, according to Eq. (3.26), and $p_{\mathrm{FEM}}(\mathbf{x},\omega)$ is the result computed with the FEM. The error at 201 Hz in dB between the output of the KHI and the reflected sound field as computed with the FEM is shown in Fig. 5.3. This figure shows the error, which is between about -80 to -60 dB through the whole region within the contour. The error figure also shows that the error does not change with position, but remains at the same level anywhere within the contour, although an increase in error close to the source is noticeable. Small artifacts that are visible are due to the coarseness of the sampling grid.

Similarly, the results at 501 Hz have been computed with the KHI method, shown in Fig. 5.4 and with the FEM, shown in Fig. 5.5. It can be concluded from these

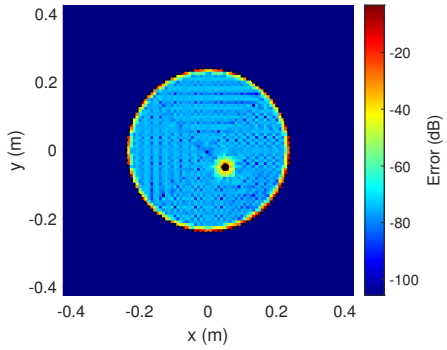

Figure 5.3: Error at 201 Hz between the output of the KHI (Fig. 5.1) and the reflected sound field computed with the FEM (Fig. 5.2) within the contour. Although Fig. 5.1 and Fig. 5.2 do not show the imaginary parts but only the real parts, the error shown in this figure is computed using both the real and imaginary parts. The error outside the contour is not shown. The location of the source is indicated by the black dot.

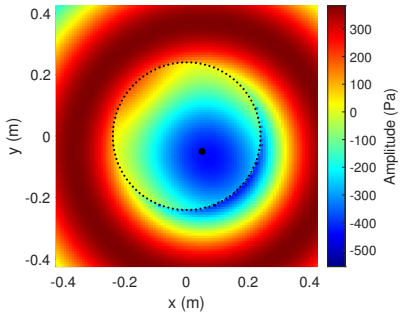

Figure 5.4: Real part of the output of the KHI at 501 Hz for a source inside the circle. The location of the source is indicated by the black dot. The result is valid only within the contour.

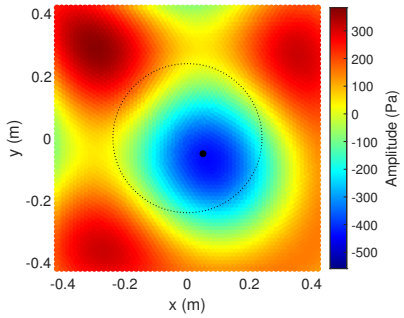

Figure 5.5: Real part of the reflected sound field computed with the FEM at 501 Hz. The location of the source is indicated by the black dot. The contour is shown for reference.

figures that the KHI method and the reflected sound field computed with the FEM are in agreement within the contour.

Using Eq. (5.1), the error between the output of the KHI and the reflected sound field computed with the FEM is computed at 501 Hz and shown in Fig. 5.6. This figure shows that the error is about -50 dB through the whole region within the contour, although an increase in error close to the source is noticeable. In general, an increase in error compared with the results at 201 Hz is noticeable, which might be due to the shorter wavelengths while maintaining the same sampling grid.

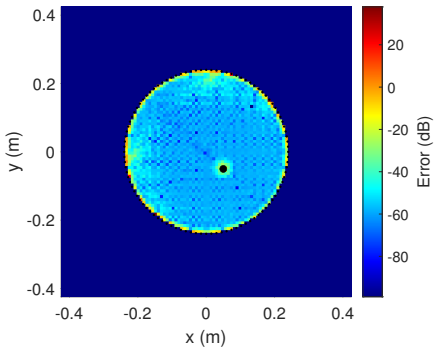

Figure 5.6: Error at 501 Hz between the output of the KHI (Fig. 5.4) and the reflected sound field computed with the FEM (Fig. 5.5) within the contour. Although Fig. 5.4 and Fig. 5.5 do not show the imaginary parts, but only the real parts, the error shown in this figure is computed using both the real and imaginary parts. The error outside the contour is not shown. The location of the source is indicated by the black dot.

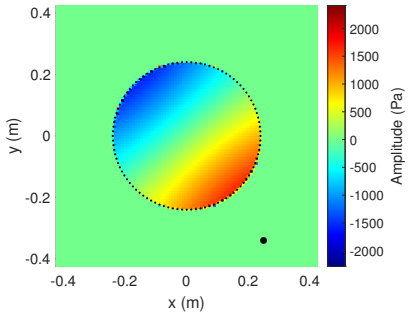

Figure 5.7: Real part of the output of the KHI at 201 Hz for a source outside the circle. The location of the source is indicated by the black dot. The result is valid only within the contour.

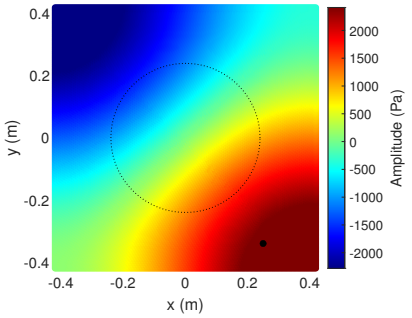

Figure 5.8: Real part of the total sound field computed with the FEM at 201 Hz. The location of the source is indicated by the black dot. The contour is shown for reference.

5.2.2 The Kirchhoff-Helmholtz integral with a source outside the contour

A similar comparison is made for the situation where the source is located outside the contour. The same model with identical parameters as presented in the previous section (Sec. 5.2.1) is used, but in this case the monopole point source is placed at $(x, y) = (0.25, -0.34)$. As described in Ch. 3, with a source located outside the contour, the output of the KHI is the total sound field due to this source. Therefore, the output of the KHI is compared with the total sound field computed with the FEM. The result of the KHI at 201 Hz is shown in Fig. 5.7 and the result computed with the FEM is shown in Fig. 5.8. Both figures show the acoustic pressure in Pa.

Similar to the results in Sec. 5.2.1, the output of the KHI and the total sound field computed with the FEM are in agreement within the contour. Outside the contour the KHI is not valid, and in the situation of a source being outside the contour, its output is around zero. The error at 201 Hz in dB between the output of the KHI and the reflected sound field as computed with the FEM is computed with Eq. (5.1) and shown in Fig. 5.9. This figure shows the error within the contour, which is between -100 to -80 dB through the whole region.

The results at 501 Hz have been computed with the KHI method, shown in Fig. 5.10, and with the FEM, shown in Fig. 5.11. Both figures show the acoustic pressure in Pa. It can be concluded from the figures that the result of the KHI method and the total sound field computed with the FEM are in agreement within the contour. The error at 501 Hz in dB between the output of the KHI and the total sound field as computed with the FEM is computed with Eq. (5.1) and shown in Fig. 5.12. This figure shows the error within the contour, which is between approximately -80 and -60 dB through the whole region. Again, the error seems to increase with the frequency, as was found in Sec. 5.2.1.

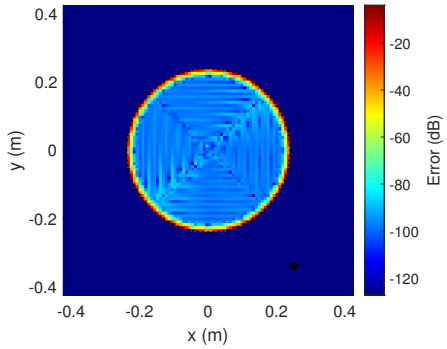

Figure 5.9: Error at 201 Hz between the output of the KHI (Fig. 5.7) and the total sound field computed with the FEM (Fig. 5.8) within the contour. Although Fig. 5.7 and Fig. 5.8 do not show the imaginary parts but only the real parts, the error shown in this figure is computed using both the real and imaginary parts. The error outside the contour is not shown. The location of the source is indicated by the black dot.

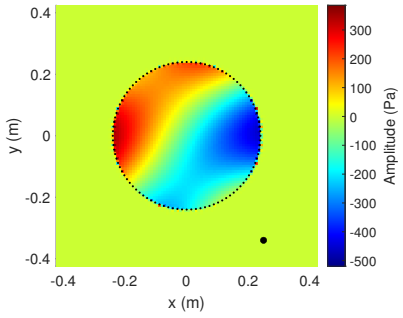

Figure 5.10: Real part of the output of the KHI at 501 Hz for a source outside the circle. The location of the source is indicated by the black dot. The result is valid only within the contour.

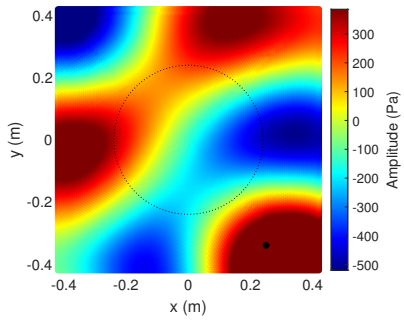

Figure 5.11: Real part of the total sound field computed with the FEM at 501 Hz. The location of the source is indicated by the black dot. The contour is shown for reference.

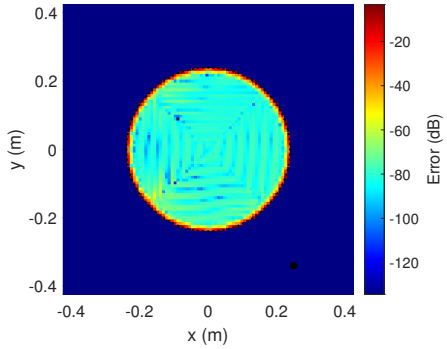

Figure 5.12: Error at 501 Hz between the output of the KHI (Fig. 5.10) and the total sound field computed with the FEM (Fig. 5.11) within the contour. Although Fig. 5.10 and Fig. 5.11 do not show the imaginary parts, but only the real parts, the error shown in this figure is computed using both the real and imaginary parts. The error outside the contour is not shown. The location of the source is indicated by the black dot.

5.2.3 Error introduced by particle velocity estimation

In Sec. 5.2.1 and Sec. 5.2.2 the particle velocity is computed directly with the FEM. However, in reality it must either be measured or approximated. As introduced in Eq. (3.27), the particle velocity in the radial outward direction can be obtained by a difference quotient between the sound pressure levels at the inner and outer microphones. Using the same model as described in Sec. 5.2.1, a comparison is made between the output of the KHI using particle velocity measurements computed with the FEM, and the output of the KHI in which the particle velocity is approximated using Eq. (3.27). The error is computed as

$$\mathcal{E}(\mathbf{x},\omega) = 20\log_{10}\left(\frac{|p^{(2)}(\mathbf{x},\omega) - \hat{p}^{(2)}(\mathbf{x},\omega)|}{|p^{(2)}(\mathbf{x},\omega)|}\right), \tag{5.2}$$

in which $p^{(2)}(\mathbf{x},\omega)$ is the result of the KHI with the particle velocity computed with the FEM, and $\hat{p}^{(2)}(\mathbf{x},\omega)$ is the result of the KHI with the approximated normal particle velocity computed with Eq. (3.27) using $h = 1.6$ cm.

The error is shown in Fig. 5.13 at 201 Hz, which shows that the largest error is about -45 dB. Similarly, the error at 501 Hz is shown in Fig. 5.14, the largest error being about -10 dB. As can be seen, the error is not constant through the domain, but varies with position at both frequencies. Therefore, Fig. 5.15 and Fig. 5.16 show the magnitude of $p^{(2)}(\mathbf{x},\omega)$ at 201 Hz and 501 Hz, respectively. By comparing the figures, at both frequencies the largest error is found at the locations with the smallest magnitude. This indicates that the error is among other things dependent on the magnitude of the output of the KHI through the domain. Furthermore, the error increases with the frequency, which has been noted in the previous sections as well.

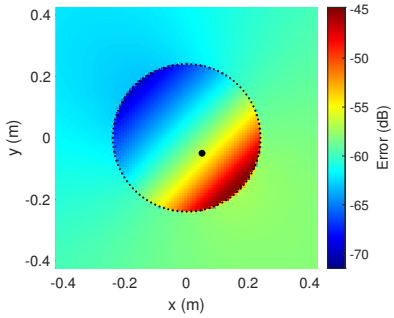

Figure 5.13: Error plot of the KHI results at 201 Hz with the true particle velocity and with the approximated particle velocity, using both the real and imaginary parts. The location of the source is indicated by the black dot.

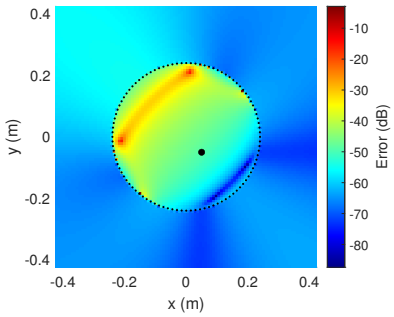

Figure 5.14: Error plot of the KHI results at 501 Hz with the true particle velocity and with the approximated particle velocity, using both the real and imaginary parts. The location of the source is indicated by the black dot.

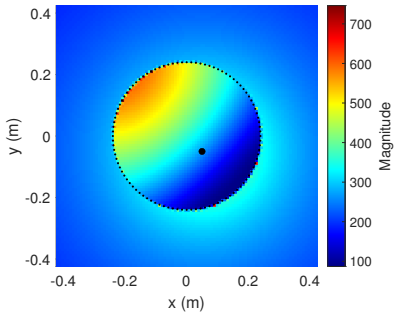

Figure 5.15: Magnitude plot of $|p^{(2)}(\mathbf{x}, \omega)|$ computed using both the real and imaginary parts at 201 Hz. The location of the source is indicated by the black dot.

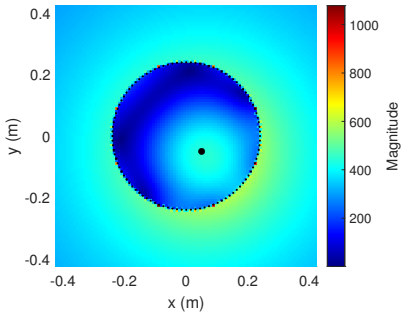

Figure 5.16: Magnitude plot of $|p^{(2)}(\mathbf{x}, \omega)|$ computed using both the real and imaginary parts at 501 Hz. The location of the source is indicated by the black dot.

5.2.4 Noise at the microphones

THe KHI method requires multiple microphones on a contour. As the number of microphones increases, the likelihood of inaccurate measurements rises. Inaccuracies might be due to calibration issues, external noise influences, instrument drift or sensitivity degradation due to wear and tear, hardware malfunction, etc. This section shows the error of the KHI in the event that some microphones are measuring inaccurate pressure levels. To see the effect on the output of the KHI, the measured pressure at some microphones is altered. The error is computed using

$$\mathcal{E}(\mathbf{x},\omega) = 20\log_{10}\left(\frac{|\hat{p}^{(2)}(\mathbf{x},\omega) - \tilde{p}^{(2)}(\mathbf{x},\omega)|}{|\hat{p}^{(2)}(\mathbf{x},\omega)|}\right), \tag{5.3}$$

in which $\hat{p}^{(2)}(\mathbf{x},\omega)$ is the result of the KHI with the estimated particle velocity using Eq. (3.27) with $h = 1.6$ cm, and $\tilde{p}^{(2)}(\mathbf{x},\omega)$ is the result of the KHI with the estimated particle velocity using Eq. (3.27) with $h = 1.6$ cm, while the measured pressure of selected microphones at the surface is modelled as

$$\tilde{p}(\mathbf{x}_s,\omega) = (1+\eta\kappa)p(\mathbf{x}_s,\omega), \tag{5.4}$$

in which κ is a scaling factor and η is the noise, defined as

$$\eta = a + \mathrm{j}b, \tag{5.5}$$

in which $a \sim \mathcal{U}_{(-1,1)}$, $b \sim \mathcal{U}_{(-1,1)}$ and $\mathcal{U}_{(a,b)}$ denotes a uniform distribution with an interval between a and b.

Starting with $\kappa = 10\%$ and every 10^{th} sensor triplet, with a sensor triplet referring to a set of three microphones in radial direction that have noisy measurements, the error is shown at 201 Hz in Fig. 5.17 and at 501 Hz in Fig. 5.18. For simplicity, a single dot on the measuring surface is shown, but three microphones in radial direction are used. The microphone triplets that have added noise are indicated with the red enlarged squares. All the results through this section are obtained by averaging over five realizations.

The maximum error at 201 Hz is about -20 dB, while the maximum error at 501 Hz is about 10 dB, although the average error is -40.5 dB. Using the same approach, but now with the first 25 microphone triplets measuring altered pressures with $\kappa = 10\%$, Fig. 5.19 shows the error at 201 Hz, and Fig. 5.20 shows the error at 501 Hz. At 201 Hz the maximum error is about -20 dB, while at 501 Hz the maximum error is about 20 dB, although the average error is -34.4 dB. Again, for increasing frequencies the error increases as well, which was found in previous sections.

Lastly, the error is shown for the situation in which all the microphones measure altered pressures using $\kappa = 10\%$, at 201 Hz in Fig. 5.21 and at 501 Hz in Fig. 5.22. The maximum error at 201 Hz is about -20 dB and the maximum error at 501 Hz is about 20 dB, although the average error is -24.8 dB. The results show that an increase in the number of microphones with altered pressure measurements results in an increase of the error at both frequencies. Furthermore, the error also increases with higher frequencies, which can be seen with any number of microphones with

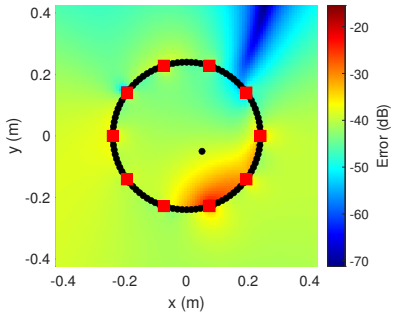

Figure 5.17: Error plot of the KHI results at 201 Hz averaged over five realizations, while noise is added to the microphones indicated by the red enlarged squares, using both the real and imaginary parts. The average error is -40.7 dB. The location of the source is indicated by the black dot.

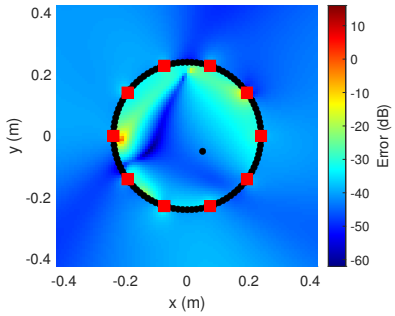

Figure 5.18: Error plot of the KHI results at 501 Hz averaged over five realizations, while noise is added to the microphones indicated by the red enlarged squares, using both the real and imaginary parts. The average error is -40.5 dB. The location of the source is indicated by the black dot.

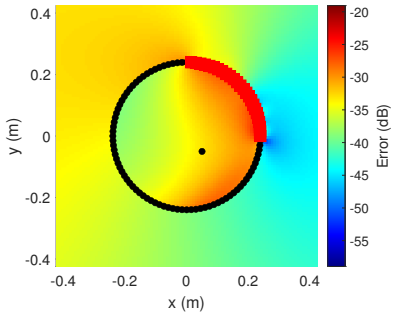

Figure 5.19: Error plot of the KHI results at 201 Hz averaged over five realizations, while noise is added to the microphones indicated by the red enlarged squares, using both the real and imaginary parts. The average error is -34.9 dB. The location of the source is indicated by the black dot.

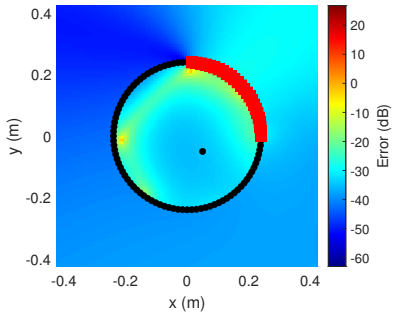

Figure 5.20: Error plot of the KHI results at 501 Hz averaged over five realizations, while noise is added to the microphones indicated by the red enlarged squares, using both the real and imaginary parts. The average error is -34.4 dB. The location of the source is indicated by the black dot.

altered pressure measurements. With increasing frequencies, the wavelengths decrease and the sound field becomes more complex, which may be a reason why the error increases. In order for the error at 501 Hz to have a maximum of 0 dB, with altered measurements at every 10^{th} sensor triplet, the noise scaling factor must be

reduced to $\kappa = 2\%$. Similarly, with altered measurements at all microphones, the noise scaling factor must be reduced to $\kappa = 1\%$ to have a maximum error of 0 dB at 501 Hz. In general, the error is not the largest close to the sensors with altered pressure measurements. Although the maximum error at 501 Hz is larger than the maximum error at 201 Hz, the average errors at both frequencies are very similar in each situation. Fig. 5.23 and Fig. 5.24 show the magnitude of $\hat{p}^{(2)}(\mathbf{x}, \omega)$ at 201 Hz and 501 Hz, respectively. Similar to the results of Sec. 5.2.3, in general the error tends to be the largest at the locations of the smallest magnitudes, especially at 501 Hz.

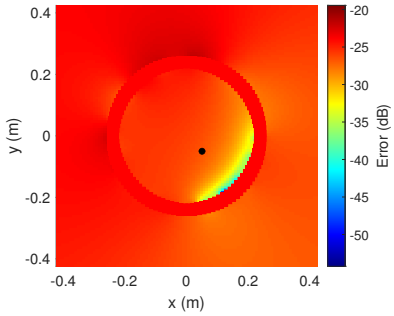

Figure 5.21: Error plot of the KHI results at 201 Hz averaged over five realizations, while noise is added to the microphones indicated by the red enlarged squares, using both the real and imaginary parts. The average error is -25.3 dB. The location of the source is indicated by the black dot.

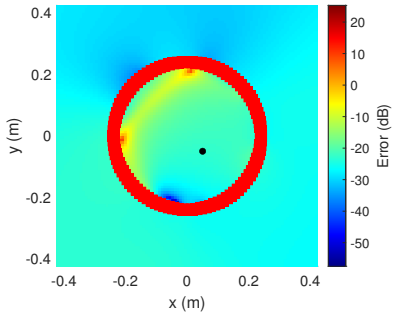

Figure 5.22: Error plot of the KHI results at 501 Hz averaged over five realizations, while noise is added to the microphones indicated by the red enlarged squares, using both the real and imaginary parts. The average error is -24.8 dB. The location of the source is indicated by the black dot.

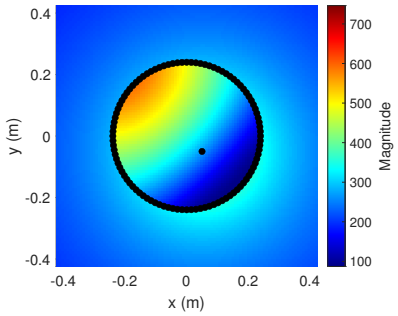

Figure 5.23: Magnitude plot of $|\hat{p}^{(2)}(\mathbf{x}, \omega)|$ computed using both the real and imaginary parts at 201 Hz. The location of the source is indicated by the black dot.

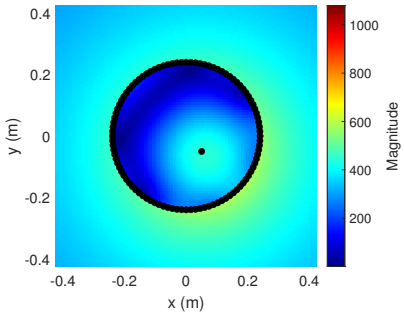

Figure 5.24: Magnitude plot of $|\hat{p}^{(2)}(\mathbf{x}, \omega)|$ computed using both the real and imaginary parts at 501 Hz. The location of the source is indicated by the black dot.

5.3 The suppression of the reflected sound field in a small-scale two-dimensional configuration

A numerical study is performed for a multichannel system in which $K = L = M = P = 12$, where all sources are independent. The control coefficients are computed with the FD-RMFE algorithm, as presented in Sec. 4.2. The choice was made to use an equal number of sources and sensors, but the numbers do not need to be equal. The number of performance sensors is $L_{\text{perf}} = 37$, which are spatially distributed within the microphone contour with a distance of 0.06 m from each other, starting from the origin. The configuration of the system is shown in Fig. 5.25, with the objective of attenuating the reflected sound field. Because this numerical study and, especially, this algorithm involve the use of a lot of parameters, a summary of the involved parameters is given in Table 5.1. The dimensions of the chamber and the number of sources and sensors in this numerical study are based on a small-scale active anechoic chamber which is shown in Sec. 6.2. If, instead of using reference microphones, it is possible to place sensors directly on a sound radiating object in the room, this is favourable in terms of time-advantage and probably results in a stronger correlation with the noise signal.

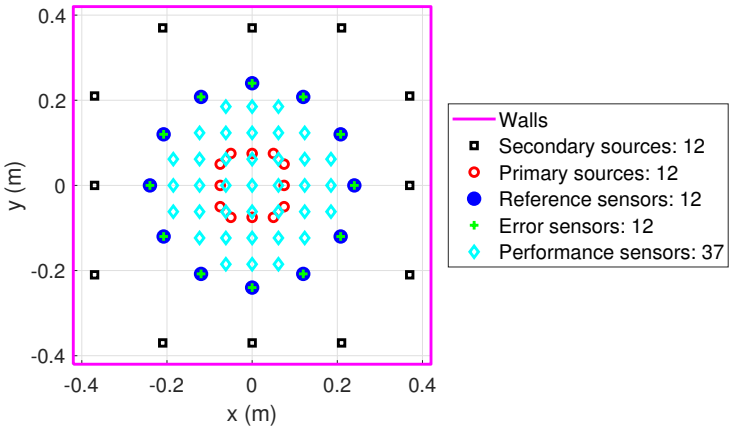

Figure 5.25: Two-dimensional system configuration of the 12-channel active noise control setup to attenuate acoustic reflections from the walls.

Following Fig. 5.25, a feedforward control system is implemented according to the procedure described in Sec. 2.2.2, to suppress the reflections. Each of the 12 error sensors is equipped with three microphones aligned in radial direction, which are the input of the KHI; the middle microphone is shown in Fig. 5.25. The middle error microphones and the reference microphones occupy the same positions, and could function as a single microphones in real-time. With reference to Fig. 2.2, the primary

The results presented in this section are published in [148].

noise signal is then the output of the KHI with the primary sources active measured at the performance sensors, denoted by $\mathbf{d}(n)$. The objective of the system is to minimize $\mathbf{e}(n) = \mathbf{d}(n) + \mathbf{y}(n)$, in which $\mathbf{e}(n)$ is the performance signal measured at the performance sensors and $\mathbf{y}(n)$ is the secondary signal which is the output of the KHI due to the secondary sources measured at the performance sensors.

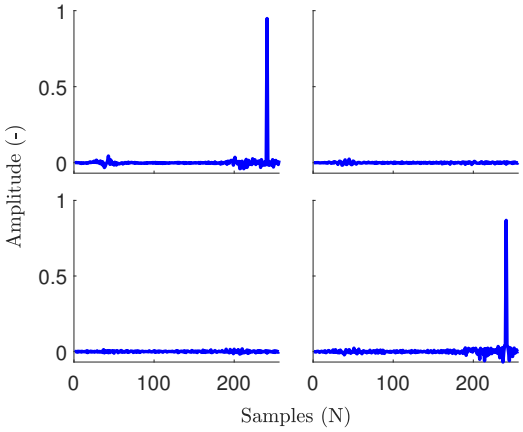

Figure 5.26: The decoupled plant impulse response matrix $\hat{\bar{\boldsymbol{G}}}_{\mathrm{ai}}(z)\bar{\boldsymbol{G}}(z)\hat{\bar{\boldsymbol{G}}}_{\mathrm{mi}}(z)$. The other channels are similar and thus omitted.

The speed of sound is $c = 343$ m/s and the density of the air is $\rho = 1.21$ kg/m^3. The walls have the dimensions of 0.84 m square, modelled using an impedance of $Z = 10\rho c$. The primary and secondary sources are modelled by monopole sources. The distance between the secondary sources is 0.21 m and the primary sources is 0.075 m. The secondary sources are placed with a spacing of 0.05 m from the walls. The primary sources are placed at 0.12 m from the origin. The sensors are placed on a circle around the origin with a radius of $r = 0.24$ m. The reference sensors measure the pressure at the reference sensor locations. The performance sensors are the locations at which the KHI is evaluated, resulting in the performance signals. In order to prevent spatial aliasing, according to the Nyquist sampling [159] criterion, the maximal distance between any of the microphones is $d_{\max} = \frac{c}{2f_{\max}} = \frac{343}{1200} = 0.286$ m. This condition is satisfied for the performance sensors with a distance of 0.06 m and the error and reference sensors with a distance of 0.126 m. Furthermore, for accurate reconstruction of the secondary sound field, the secondary sources need to satisfy this condition as well [50, 92], which they do with a distance of 0.21 m.

The transfer functions between the source-sensor pairs are computed with the FEM in COMSOL 6.0 with the Acoustics module, using at least four quadratic elements per wavelength. The reference sensor transfer function matrix $\boldsymbol{X}(\mathrm{e}^{\mathrm{j}\omega})$ is obtained by sampling in the frequency domain from 1 Hz to 600 Hz with a frequency resolution of 1 Hz, using vanishing frequency bins at 0 Hz and the Nyquist frequency of 600 Hz. The acoustic pressure at the error sensors is obtained by sampling in the frequency domain from 1 Hz to 600 Hz with a frequency resolution of 1 Hz, us-

Table 5.1: Summary of the parameters.

Parameter	Quantity	Unit	Description
$K = L = M = P$	12	-	Number of sources and sensors
L_{perf}	37	-	Number of performance sensors
c	343	m/s	Speed of sound
ρ	1.21	kg/m3	Density of air
Room size	0.84 x 0.84	m	Length x width
Z	$10\rho c$	pa·s/m	Impedance at the walls
d_{ss}	0.21	m	distance between secondary sources
d_{ps}	0.075	m	distance between primary sources
$d_{\text{ss-wall}}$	0.05	m	distance between secondary sources and the wall
r_{sens}	0.24	m	Radius of the circle on the origin at which the sensors are placed
f_{start}	0	Hz	Start of range for frequency domain sampling
f_{step}	1	Hz	Frequency resolution
f_{end}	600	Hz	End of range for frequency domain sampling
f_s	1200	Hz	Sampling rate
$\sqrt{\beta_G}$	20	dB	Regularization factor for secondary path
J	256	samples	Length of plant model
N_{FFT}	512	samples	Number of samples used in the Fourier transform
Δ_{mi}	200	samples	Delay in the $\hat{\tilde{\boldsymbol{G}}}_{\text{mi}}(z)$ filter
Δ_{mi}^{-}	-200	samples	Delay in the $\hat{\tilde{\boldsymbol{G}}}_{\text{ai}}(z)$ filter
Δ_{ai}	240	samples	Delay in the $\hat{\tilde{\boldsymbol{G}}}_{\text{ai}}(z)$ filter
n_{iter}	2e4	samples	Number of iterations in the algorithm
$\sqrt{\beta_F}$	60	dB	Regularization factor of the prewhitening filter
Δ_F	257	samples	Delay in the $\hat{\tilde{\boldsymbol{F}}}_w(z)$ filter
Δ_{art}	50	samples	Delay of the noise signal
I	64	samples	Control filter length
O	512	samples	Length of the prewhitening filter
α_0	4	-	Step size of the algorithm
n_{pwf}	2e4	-	Length of the reference signals to compute $\hat{\tilde{\boldsymbol{F}}}_w(z)$
n_{window}	80	-	Length of the Hamming window to compute $\hat{\tilde{\boldsymbol{F}}}_w(z)$
n_{overlap}	50%	-	Overlap between windows to compute $\hat{\tilde{\boldsymbol{F}}}_w(z)$
f_{clp}	480	Hz	Cutoff frequency of the low-pass filter applied to $\boldsymbol{P}(\mathrm{e}^{\mathrm{j}\omega})$ and $\boldsymbol{G}(\mathrm{e}^{\mathrm{j}\omega})$.
f_{chp}	120	Hz	Cutoff frequency of the high-pass filter applied to $\boldsymbol{P}(\mathrm{e}^{\mathrm{j}\omega})$ and $\boldsymbol{G}(\mathrm{e}^{\mathrm{j}\omega})$.
h	0.01	m	Distance between microphones in radial direction.

ing vanishing frequency bins at 0 Hz and the Nyquist frequency of 600 Hz, resulting in a sampling frequency of $f_s = 1200$ Hz. Following Eq. (3.27), the normal particle velocity is computed at the error sensors using $h = 0.01$ m. Using the acoustic pressure and the normal particle velocity at the error sensors, the Kirchhoff-Helmholtz integral is computed, from which the primary- and secondary-path transfer function matrices $\boldsymbol{P}(\mathrm{e}^{\mathrm{j}\omega})$ and $\boldsymbol{G}(\mathrm{e}^{\mathrm{j}\omega})$ are computed. The matrix $\boldsymbol{P}(\mathrm{e}^{\mathrm{j}\omega})$ is the transfer function matrix from the primary sources to the performance sensors, and the matrix $\boldsymbol{G}(\mathrm{e}^{\mathrm{j}\omega})$ is the transfer function matrix from the secondary sources to the performance sensors. Both $\boldsymbol{P}(\mathrm{e}^{\mathrm{j}\omega})$ and $\boldsymbol{G}(\mathrm{e}^{\mathrm{j}\omega})$ are filtered with 1) a second-order low-pass filter [160] having a cut off frequency at 480 Hz and 2) a second-order high-pass filter [160] having a cut off frequency at 120 Hz. These two filters are applied to minimize frequency domain artifacts that occur when transforming a pass-band with sharp cut offs from the frequency domain to the time domain. The primary path transfer function matrix is converted from the frequency domain to the time domain using the Fourier transform resulting in the matrix of impulse responses $\boldsymbol{P}(z)$.

The secondary path is regularized using $\beta_G = 3.48 \times 10^4$, such that $\sqrt{\beta_G}$ is at 20 dB below the largest frequency domain peak of $\boldsymbol{G}(\mathrm{e}^{\mathrm{j}\omega})$, and truncated after $J = 256$

samples such that $\bar{\boldsymbol{G}}(z)$ is obtained. The preconditioning and decoupling filters are computed using $N_{FFT} = 512$ Fourier Transform samples, resulting in $\bar{\boldsymbol{G}}_{\text{mi}}(z)$ and $\bar{\boldsymbol{G}}_{\text{ai}}(z)$. Adding a delay of $\Delta_{\text{mi}} = 200$ samples to $\bar{\boldsymbol{G}}_{\text{mi}}(z)$ results in $\tilde{\bar{\boldsymbol{G}}}_{\text{mi}}(z)$, which, after truncation to length J, results in $\hat{\bar{\boldsymbol{G}}}_{\text{mi}}(z)$. Similarly, $\bar{\boldsymbol{G}}_{\text{ai}}(z)$ is delayed by $\Delta_{\text{mi}}^{-} = -200$ samples, followed by a delay of $\Delta_{\text{ai}} = 240$ samples, resulting in $\tilde{\bar{\boldsymbol{G}}}_{\text{ai}}(z)$. Truncation of $\tilde{\bar{\boldsymbol{G}}}_{\text{ai}}(z)$ to length J results in $\hat{\bar{\boldsymbol{G}}}_{\text{ai}}(z)$. The decoupling of the plant is shown in Fig. 5.26, from which it can be seen that the plant is effectively decoupled, having a diagonal response with a pure delay that corresponds to Δ_{ai} delay samples. The delays Δ_{mi} and Δ_{ai} correspond to the length of the secondary path impulse response J. In general, choosing $\Delta_{\text{mi}} \approx 0.8J$ and $\Delta_{\text{ai}} \approx 0.95J$ seems to be a good starting point, but this is dependent on the application. If those numbers differ too greatly from what they should be, the decoupling of the system is reduced.

The prewhitening and decorrelation filter is shown in Fig. 5.27. The filter is computed from the reference signals of length $n = 20000$ using Welch's method [161] with a Hamming window length of 80 samples having an overlap of 50%. A regularization using $\beta_F = 3.1 \times 10^2$ is applied, such that $\sqrt{\beta_F}$ is at 60dB below the largest eigenvalue of $\boldsymbol{D}(\mathrm{e}^{\mathrm{j}\omega})$ in the frequency domain, resulting in $\bar{\boldsymbol{F}}_w(z)$. Because the PSD matrix is positive semi-definite symmetric, a delay of $\Delta_F = \frac{512}{2} + 1 = 257$ samples is added, resulting in $\tilde{\bar{\boldsymbol{F}}}_w(z)$, followed by truncation to a length of 512 samples, resulting in $\hat{\bar{\boldsymbol{F}}}_w(z)$.

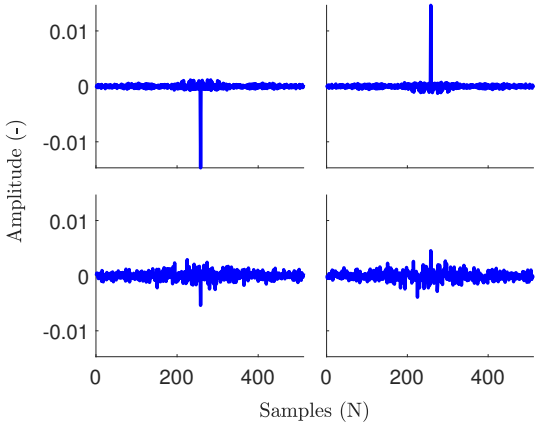

Figure 5.27: Prewhitening filter $\hat{\bar{\boldsymbol{F}}}_w(z)$ corresponding to the inputs 1, 2 and outputs 1, 2. The other channels are similar and thus omitted.

The coherence between the reference signals is shown in Fig. 5.28, showing that the signals are properly decorrelated after filtering with the prewhitening filter.

The noise signal is a Gaussian white noise signal convolved with the primary path, which is filtered with an anti-aliasing filter having a cut off frequency at $f_{\text{Nyq}} = 600$ Hz. Upon running the FD-RMFE algorithm, the noise signal is delayed by $\Delta_d = \Delta_F + \Delta_{\text{mi}} + \Delta_{\text{art}}$ samples, with $\Delta_{\text{art}} = 50$ artificial delay samples. The choice

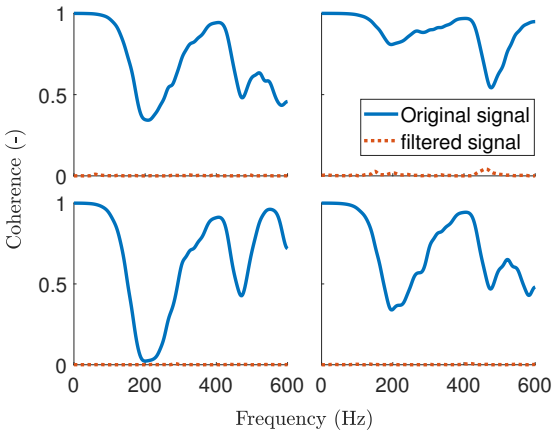

Figure 5.28: Coherence between a selected subset of reference signals. Blue shows the original reference signals. Red shows the reference signals after filtering with $\hat{\boldsymbol{F}}_w(z)$. Left upper figure: reference sensors 1 and 3. Right upper figure: reference sensors 2 and 3. Left lower figure: reference sensors 1 and 4. Right lower figure: reference sensors 2 and 4. The other channels show similar results and are therefore omitted.

of the number of Δ_{art} samples should be large enough that the reference signal has sufficient time-advance compared to the disturbance signal. However, increasing Δ_{art} also increases computational complexity, because while running the algorithm, the length of the filter coefficients is extended with Δ_{art} samples. The system is simulated using $n = 2e4$ time samples, with a desired filter length of $I = 64$ samples, requiring 12.2 seconds on a laptop with an Intel Core i7-10750H @ 2.60 GHz CPU and 16 GB of RAM. The FD-RMFE algorithm converged to a reduction of 12.8 dB, averaged over all performance sensors, as is shown in Fig. 5.29. A step-size of $\alpha_0 = 4$ is used, which is the maximum allowable value for which the algorithm converges, found in a heuristic manner. Using the same settings, the normalized FeLMS algorithm converged to 3.3 dB averaged over all sensors. The normalized FeLMS algorithm required over $2e5$ iterations to obtain the same performance of 12.8 dB reduction averaged over all performance sensors, as was the case with the FD-RMFE algorithm. This shows that the preconditioning filters, changes in the adaptation loop and regularization reduce the number of iterations by about a factor 10 for this numerical study with these parameters. Exporting the particle velocity directly from the FEM, without approximation using Eq. (3.27), allows for higher reduction levels. This shows that the approximation of Eq. (3.27) introduces a small error (as shown in Sec. 5.2.3), but allows the use of microphones.

After running the FD-RMFE algorithm, the last updated set of filter coefficients $\boldsymbol{C}(z)$ is converted to $\boldsymbol{W}_\Delta(z)$ using Eq. (4.8), where subscript Δ is used to indicate that this controller includes a delay. The delays Δ_{mi} and Δ_F are truncated from the filter coefficients and are shown in Fig. 5.30, still having a delay corresponding to Δ_{art}.

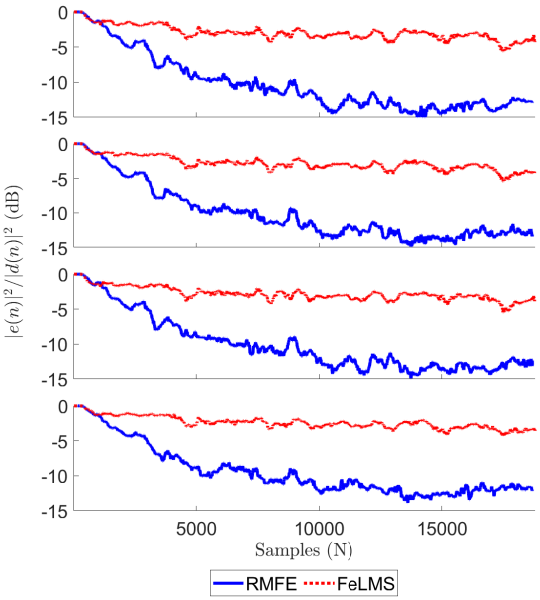

Figure 5.29: Convergence at the first four performance sensors with the FD-RMFE algorithm and the normalized FeLMS algorithm. The average reduction of the FD-RMFE algorithm is 12.8 dB, while the average reduction of the normalized FeLMS algorithm is 3.3 dB. The signals are averaged using a window of 500 samples.

For the system to be applicable in the real world, Δ_{art} is truncated from the set of filter coefficients $\boldsymbol{W}_{\Delta}(z)$, resulting in the desired set of filter coefficients $\boldsymbol{W}(z)$ with length I, which is shown in Fig. 5.31.

Both sets of control filter coefficients $\boldsymbol{W}_{\Delta}(z)$ and $\boldsymbol{W}(z)$ are simulated with the configuration shown in Fig. 2.2. The primary noise signal is the output of the KHI with the primary sources active, which is denoted by $\mathbf{d}(n)$. The objective of the system is to minimize $\mathbf{e}(n) = \mathbf{d}(n) + \mathbf{y}(n)$, in which $\mathbf{e}(n)$ is the output of the KHI, named the performance signal, and $\mathbf{y}(n)$ is the secondary signal which is the output of the KHI due to the secondary sources. The frequency domain spectral densities are shown in Fig. 5.32. Running the controller with the set of filter coefficients $\boldsymbol{W}_{\Delta}(z)$ with a primary noise signal that is delayed by Δ_{art} samples shows an average performance of 15.4 dB. Running the controller with the set of filter coefficients $\boldsymbol{W}(z)$ with a primary noise signal without any delay shows an average performance of 13.8 dB. Removal of the delay from the filter coefficients shows an average loss in reduction of 1.6 dB averaged at the performance sensors.

The Kirchhoff-Helmholtz integral is computed throughout the domain, and the results are shown at $f = 56.2$ Hz (Fig. 5.33 till Fig. 5.35), $f = 161.7$ Hz (Fig. 5.36 till Fig. 5.38) and $f = 396.1$ Hz (Fig. 5.39 till Fig. 5.41). It can be seen that at these frequencies the sound field due to the secondary sources approaches the inverse

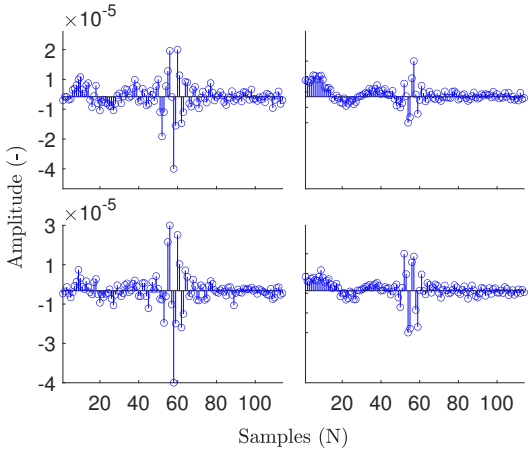

Figure 5.30: Delayed controller filter coefficients $\boldsymbol{W}_{\Delta}(z)$ of length $\bar{I} = \Delta_{\text{art}} + I$ which correspond to reference sensors $1, 2$ and secondary sources $1, 2$. The other channels show a similar delay, although the response could be different. The other channels are omitted for the sake of readability.

of the reflected sound field due to the primary sources, such that the sum of both fields is minimized by the controller. These figures also show that global control is achieved within the microphone area, which can be seen from the acoustic pressure in the field surrounded by the microphones. It should be noted that the results of the Kirchhoff-Helmholtz integral are not valid outside of the contour, but the full domain is shown for completeness.

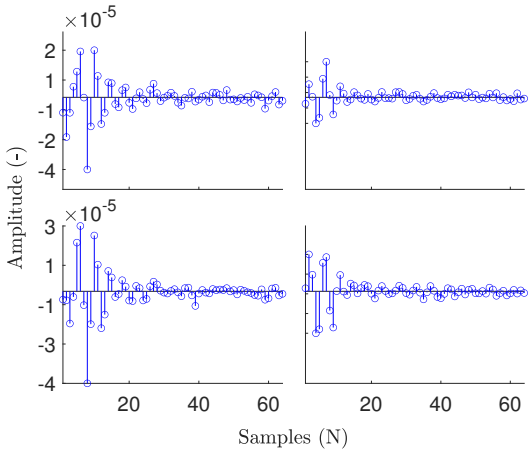

Figure 5.31: Controller filter coefficients $\boldsymbol{W}(z)$ truncated to length I which correspond to reference sensors $1, 2$ and secondary sources $1, 2$. The other channels are omitted for the sake of readability.

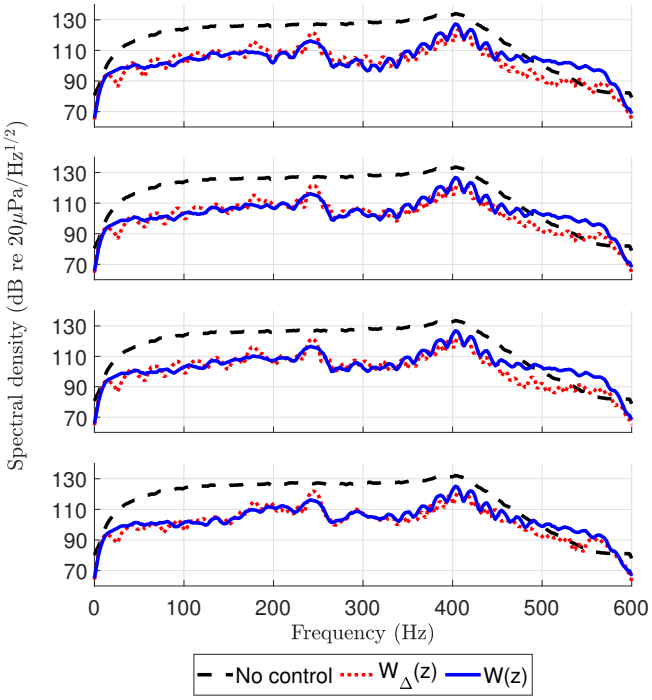

Figure 5.32: Spectral densities of the first four performance sensors. These results are obtained after running the configuration as shown in Fig. 2.2 using the delayed controller $\boldsymbol{W}_\Delta(z)$ with the noise signal that is delayed by Δ_{art} samples, as opposed to the controller $\boldsymbol{W}(z)$ which has a noise signal that is not delayed. The average reduction over all performance sensors is 15.4 dB, using the filter coefficients $\boldsymbol{W}_\Delta(z)$. The average reduction over all performance sensors with the filter coefficients $\boldsymbol{W}(z)$ is 13.8 dB. The signals are averaged using a window of 500 samples.

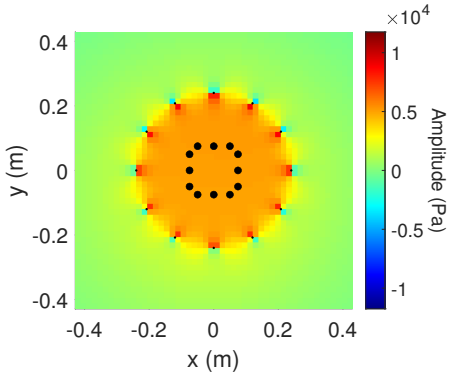

Figure 5.33: Real part of the output of the Kirchhoff-Helmholtz integral at 56.2 Hz, with the primary sources active, which are located at the black dots. The result is valid only inside the contour.

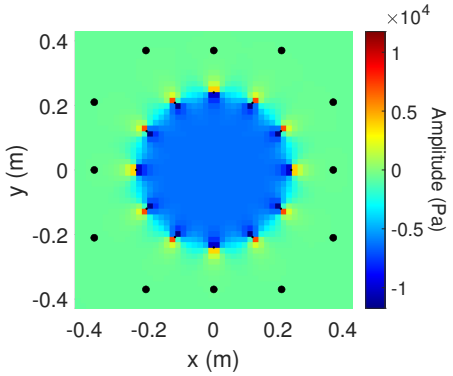

Figure 5.34: As Fig. 5.33, but with the secondary sources active.

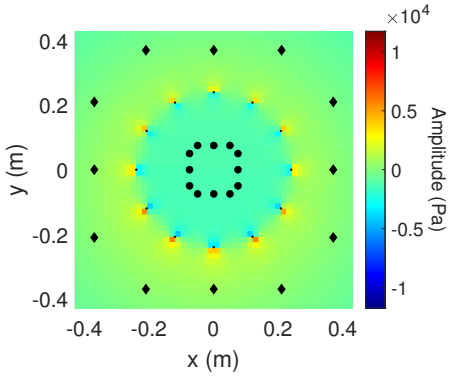

Figure 5.35: Sum of Fig. 5.33 and Fig. 5.34.

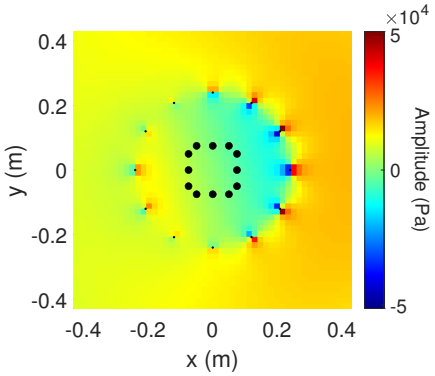

Figure 5.36: As Fig. 5.33, but at 161.7 Hz.

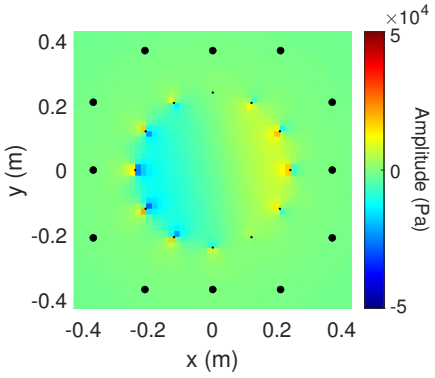

Figure 5.37: As Fig. 5.33, but with the secondary sources active, at 161.7 Hz.

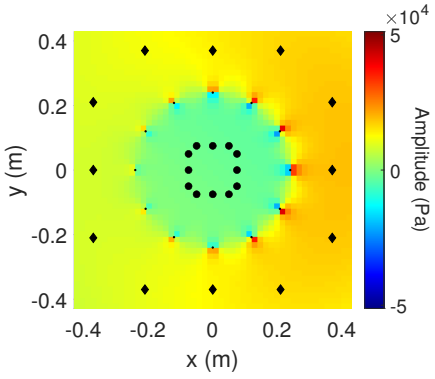

Figure 5.38: Sum of Fig. 5.36 and Fig. 5.37.

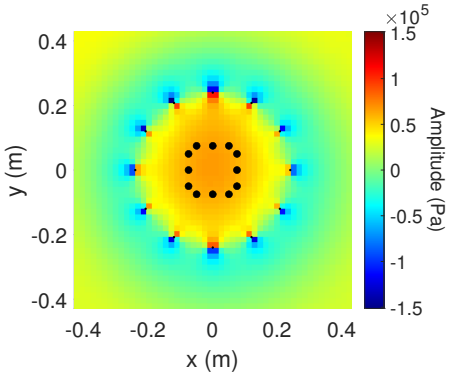

Figure 5.39: As Fig. 5.33, but at 396.1 Hz.

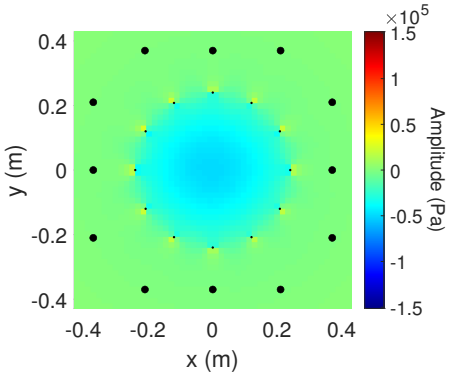

Figure 5.40: As Fig. 5.33, but with the secondary sources active, at 396.1 Hz.

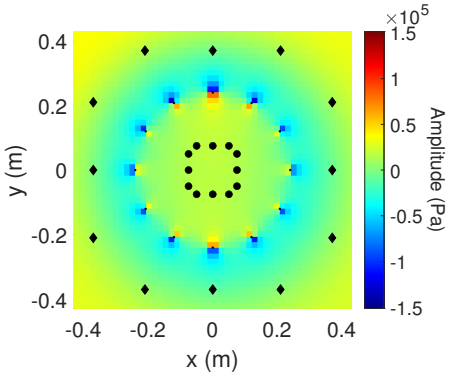

Figure 5.41: Sum of Fig. 5.39 and Fig. 5.40.

5.4 The suppression of the reflected sound field in a large-scale two-dimensional configuration

The numerical study of a two-dimensional multichannel system in which $K = L = M = P = 200$, where all sources are independent is shown in this section. For convenience, the choice was made to use an equal number of sources and sensors, but the numbers do not need to be equal. The configuration of the system is shown in Fig. 5.42, with the objective of suppressing the reflected sound field.

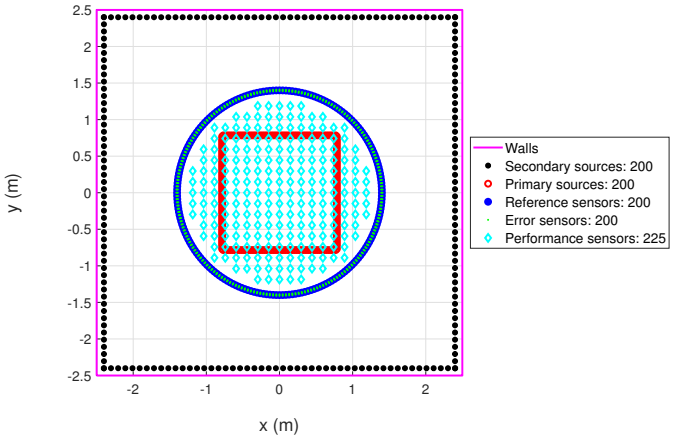

Figure 5.42: Two-dimensional system configuration of the active noise control setup with 200 sources, 200 reference sensors and 225 performance sensors to suppress acoustic reflections from the walls. The reference sensors and the error sensors have the same positions

With reference to Fig. 5.42, a feedforward control system is implemented according to the procedure described in Sec. 2.2.2, to suppress the reflections. In this case, each of the 200 error sensors is equipped with three microphones aligned in radial direction, which is the input of the KHI. With reference to Fig. 2.2, the primary noise signal is then the output of the KHI with the primary sources active measured at the performance sensors, denoted by $\mathbf{d}(n)$. The objective of the system is to minimize $\mathbf{e}(n) = \mathbf{d}(n) + \mathbf{y}(n)$, in which $\mathbf{e}(n)$ is the performance signal measured at the performance sensors and $\mathbf{y}(n)$ is the secondary signal which is the output of the KHI due to the secondary sources measured at the performance sensors.

The room is of dimensions 5-by-5 m^2, with the walls having an impedance of $Z = 10\rho c$, in which $c = 343$ m/s denotes the speed of sound and $\rho = 1.21$ kg/m^3 is the density of the air. The primary and secondary sources are modelled as monopole sources. The distance between the secondary sources is 0.098 m, with a spacing from the wall of 0.1 m. The distance between the primary sources is 0.031 m, with

The results presented in this section are submitted in [150].

a spacing from the centre of the room of 0.8 m. The reference sensors are placed at the coordinates $(x_r, y_r) = (r_s \cos\theta_r, r_s \sin\theta_r)$, in which $r_s = 1.4$ m and $\theta_r = 2\pi i,\ i = 0, \ldots, K-1$. The reference sensors measure the acoustic pressure at the reference sensor locations. Each error sensor is equipped with three pressure microphones in radial direction. The error microphones are placed at the coordinates $(x_e, y_e) = (\{r_s, r_s \pm h\} \cos\theta_e, \{r_s, r_s \pm h\} \sin\theta_e)$, in which $\theta_e = 2\pi i,\ i = 0, \ldots, L-1$ and $h = 0.01$ m. Using the inner and outer error microphones at $r_s \pm h$, the particle velocity is estimated, following Eq. (3.27). With the middle error microphones at r_s, the acoustic pressure is measured. With the particle velocity and acoustic pressure, the KHI is computed, resulting in the performance sensors within the circle. The performance sensors are spatially distributed within the microphone surface with a distance of 0.1482 m from each other, starting from the centre of the room.

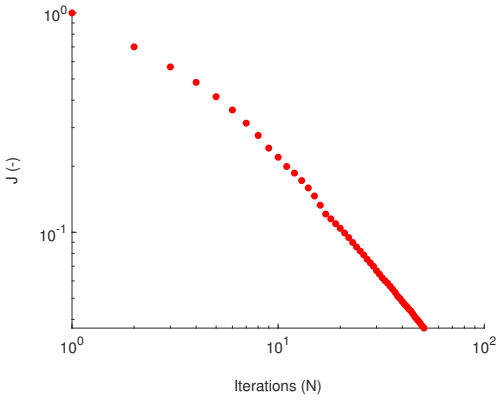

Figure 5.43: Convergence of the cost function while running the CG algorithm. Total elapsed time is 317 seconds.

The transfer functions between all the source-sensor pairs are computed with the FEM in COMSOL 6.0 with the Acoustics module, using at least four quadratic elements per wavelength. A frequency domain study from 5 Hz to 595 Hz with a frequency resolution of 5 Hz is computed, using vanishing frequency bins at 0 Hz and the Nyquist frequency of 600 Hz, resulting in a sampling frequency of $f_s = 1200$ Hz. The transfer function matrix from the primary sources to the reference sensors $\mathbf{X}(e^{j\omega})$ is exported. Similarly, the transfer function matrices from the primary and secondary sources to the error sensors are obtained. With these transfer functions, the KHI is evaluated at $L_{\text{perf}} = 225$ performance sensor locations, resulting in the transfer function matrices from the primary and the secondary sources to the performance sensors $\mathbf{P}(e^{j\omega})$ and $\mathbf{G}(e^{j\omega})$, respectively. Both transfer function matrices $\mathbf{P}(e^{j\omega})$ and $\mathbf{G}(e^{j\omega})$ are filtered with 1) a second-order high-pass filter having a cut off frequency at 20 Hz, and 2) a second-order low-pass filter having a cut off frequency at 590 Hz. These filters are applied to prevent aliasing and to minimize time domain artifacts that occur when transforming from the frequency domain to the time domain. The reference path, secondary path and primary path are modelled by FIR filters of 512 samples.

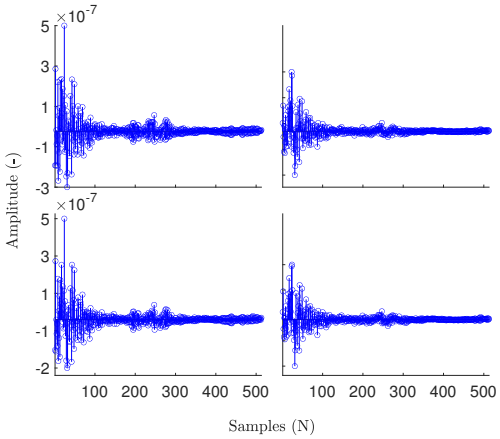

Figure 5.44: Control filter coefficients $\mathbf{W}(z)$, obtained after running the proposed algorithm. The filter coefficients correspond to reference sensors 1,2 and secondary sources 1,2. The other channels are omitted.

The CC-CG algorithm is used to find a set of control coefficients, within a maximum of 50 iterations, using a regularization parameter of $\beta = 1 \times 10^{-2}$ as shown in [162], and $N_{\text{FFT}} = 1024$ Fourier Transform samples. The algorithm takes 317 seconds to do the 50 iterations on a laptop with an Intel Core i7 $-$ 10750H CPU @ 2.60 GHz with 16 GB of RAM. The convergence of the cost function is shown in Fig. 5.43. The algorithm computes the control filter coefficients $\mathbf{W}(z)$ with a length of $I = N_{\text{FFT}}/2 + 1$. However, if desired, the coefficients can be truncated. The filter coefficients corresponding to the first two reference sensors and the first two secondary sources are shown in Fig. 5.44.

The control coefficients $\mathbf{W}(z)$ are used to simulate the performance of the system following the configuration as shown in Fig. 2.2. The first sample of the driving signals of all primary sources is set to 1, to approximate a Dirac delta impulse. The spectral density of the first four performance signals is shown in Fig. 5.45, showing an average reduction of 13.4 dB.

5.5 Conclusion

In this chapter the numerical studies of the developed methods are shown. The KHI is verified with the FEM, which results in the reflected sound field if the source is located within the contour, and results in the total sound field if the source is located outside the contour. The error introduced by the particle velocity estimation is shown to be related to the pressure amplitude. The influence of noise at the microphones is shown for several situations. It is found that an increase in the number of microphones with altered pressure measurements results in an increase in the error. In all cases, the error is found to be proportional to the frequency. In addition to the studies to verify the KHI, a small-scale two-dimensional numerical study is shown of a control system with the objective of suppressing the reflections from the

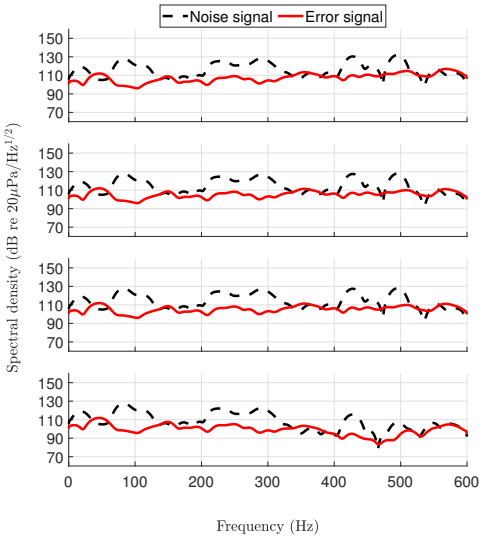

Figure 5.45: Spectral densities of the first four performance sensors using the control coefficients $\mathbf{W}(z)$ with the feedforward scheme of Fig. 2.2. The reduction levels are 13.0, 13.6, 13.6 and 13.4 dB, respectively, from top to bottom.

walls. The reflected sound field is computed with the KHI and the control system, in which the filter coefficients are computed with the FD-RMFE algorithm, and is able to effectively attenuate the reflections. Lastly, a large-scale two-dimensional numerical study is shown of a control system with the objective of suppressing the reflections from the walls. Similarly, the KHI is used to compute the reflected sound field, which is suppressed using a control system in which the control coefficients have been computed with the CC-CG algorithm. This numerical study shows that the CC-CG algorithm is effective to obtain the control coefficients with a large number of sources and sensors. With the small-scale and large-scale numerical studies is shown that the reflections are effectively suppressed.

Chapter 6

Experimental results

6.1 Introduction

In the previous chapter numerical studies are shown in which the developed methods are implemented. Although numerical studies allow for scaled-up versions of the system in terms of sources and sensors, this is under ideal circumstances without sensor noise, hardware constraints or environmental influences. Therefore, this chapter shows the real-time experiments using the developed methods as described in previous chapters. In Sec. 6.2 the experimental setup and its configuration are elaborated. In Sec. 6.3 a real-time experiment is shown in which the reflected sound field is computed with the KHI, and a control system is used to suppress the reflected sound field. The control coefficients in this experiment are computed using the PBC-CG algorithm (Sec. 4.3). Lastly, in Sec. 6.4 a similar real-time experiment is shown, but now the control coefficients are computed with the CC-CG algorithm (Sec. 4.4). Relevant additional material is shown in the Appendices A.2 till A.4. A real-time experiment in which the control coefficients have been computed with the FD-RMFE algorithm (Sec. 4.2) is not shown, because it was found that this algorithm requires additional time advance on the reference signals due to the delays in the preconditioning filters of the direct path. The additional time advance is not available due to the smaller dimensions of the setup.

6.2 The experimental setup

The experimental setup being used is shown in Fig. 6.1. The general idea of the setup is that the primary noise signal is generated in the middle of the setup, surrounded by a ring of microphones. This allows computation of the reflected sound field due to the primary sources within the ring of microphones. On the edges of the setup the secondary sources are located, which generate the secondary signal, to cancel the reflected sound field due to the primary sources. The height of the setup is limited to 20 cm, so the sound field is considered two-dimensional up to about 850 Hz, which is above the frequency range of interest. Both the width and the length are

0.92 m. The setup is equipped with twelve independent secondary sources (Visaton W130X) placed at the edges. Each side has three secondary sources, with a spacing of 0.3 m in which the middle one is centred. The top of the setup is covered by a plate of glass with a thickness of 1.2 cm. The setup is equipped with twelve external independent primary sources (Visaton W130X). Each primary source is placed in a box with outer-dimensions of $(w, l, h) = (0.24, 0.24, 0, 29)$ m, being its width, length and height, respectively. Each primary source box is connected to the centre of the setup with a tube of length 1 m, as shown in Fig. 6.2.

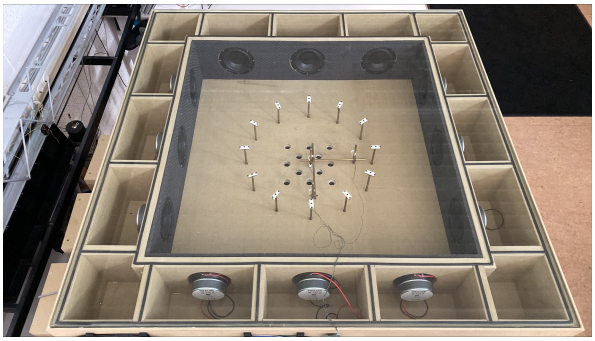

Figure 6.1: Top view showing the sensor configuration and the secondary sources of the experimental setup.

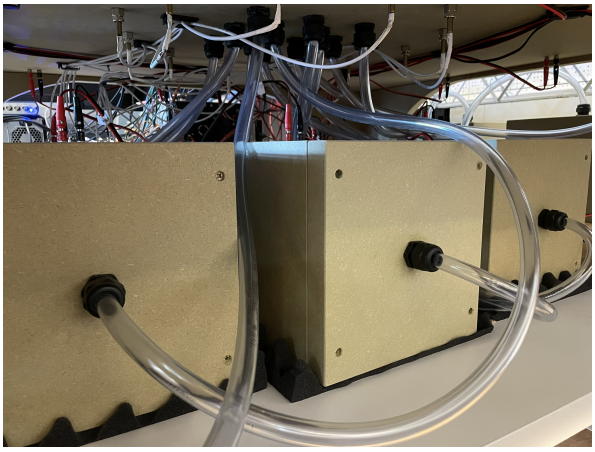

Figure 6.2: The external primary sources connected to the bottom of the experimental setup using tubes.

To obtain the desired enclosure volume for each driver, an analysis with the use of Thiele/Small parameters for the source enclosures is made. By assuming 1) a low-frequency range in which the driver acts as a piston and 2) small signals so that the driver is considered linear, a speaker analysis can be made using basic system

parameters following [163, 164]. This method allows computation of the system response function, diaphragm displacement function and transient responses. In an open enclosure, the driver response function [163] is given by

$$G(s) = \frac{s^2 T_o^2}{s^2 T_o^2 + \frac{sT_o}{Q_{TS}} + 1}, \tag{6.1}$$

in which $T_o^2 = \frac{1}{\omega_o^2}$ with $f_o = \frac{\omega_0}{2\pi}$ as the resonance frequency of the driver in Hz. The variables T_o, f_o are named T_s and f_s respectively in literature, but those variables are already in use in this thesis. The parameter Q_{TS} is defined as the total Q of the system at f_o, given by

$$Q_{TS} = \frac{Q_{MS} Q_{ES}}{Q_{MS} + Q_{ES}}, \tag{6.2}$$

in which Q_{MS} is the Q of the driver at f_o considering driver non-electronical resistances only and Q_{ES} is the Q of the driver at f_o considering electrical resistances only. The displacement function is given by

$$X(s) = \frac{1}{s^2 T_o^2 + \frac{sT_o}{Q_{TS}} + 1}, \tag{6.3}$$

which behaves like a second-order low-pass filter.

If the driver is placed in a completely closed and air-tight box, the air in the box will act like a spring, and affect the system response. The system compliance ratio is given by $\alpha = \frac{V_{AS}}{V_{AB}}$ in which $V_{AS} = \rho c^2 C_{AS}$ is the equivalent air volume of the driver suspension and $V_{AB} = \rho c^2 C_{AB}$ equals the net air volume in the enclosure if the enclosure is not filled with any absorption material. With the system compliance ratio, the new resonance frequency is computed as

$$f_c = f_o(\alpha + 1)^{1/2}, \tag{6.4}$$

the electrical quality factor is written as

$$Q_{EC} = Q_{ES}(\alpha + 1)^{1/2}, \tag{6.5}$$

and the mechanical quality factor is written as

$$Q_{MC} = Q_{MS}(\alpha + 1)^{1/2}, \tag{6.6}$$

so that the total Q is written as

$$Q_{TC} = Q_{TS}(\alpha + 1)^{1/2}. \tag{6.7}$$

The system response function is given by [164]

$$G(s) = \frac{s^2 T_c^2}{s^2 T_c^2 + \frac{sT_c}{Q_{TC}} + 1}, \tag{6.8}$$

in which $T_c^2 = \frac{1}{\omega_c^2} = \frac{1}{(2\pi f_c)^2}$. Using the parameters of the Visaton W130X speaker from the manufacturer with $f_o = 40$ Hz, $Q_{\text{MS}} = 4.39$, $Q_{\text{ES}} = 0.41$ and $V_{\text{AS}} = 5.64$ l the transfer function without and with enclosure having a volume of $V_{\text{AB}} = 7.1$ l is shown in Fig. 6.3. It can be seen from this figure that the resonance frequency increased, being approximately -5 dB, so this still is a critically-damped system. The cone displacement function is given by

$$X(s) = \frac{1}{s^2 T_c^2 + \frac{sT_c}{Q_{\text{TC}}} + 1}. \tag{6.9}$$

The cone displacement functions are shown in Fig. 6.4. A benefit of the extra stiffness of the air within the enclosure is that it keeps the diaphragm closer to its rest position, offering protection from exceeding the maximum cone displacement.

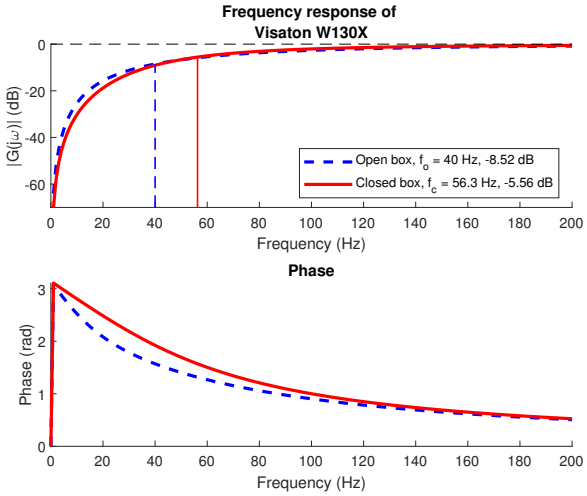

Figure 6.3: Frequency response functions of the Visaton W130X driver estimated with Thiele/Small parameters

.

The volume $V_{AB} = 7.1$ l has been applied at the primary sources; the volume $V_{AB} = 7.6$ l has been applied at the secondary sources. With respect to the enclosure volume, a description of the design approach of the primary source enclosure, the influence of the tube length and the addition of absorption to flatten the frequency spectrum are studied. The experimental setup is designed to allow up to twelve independent primary sources. Due to spatial limitations, external sources are used which are connected via tubes. Ideally, the SPL obtained from the primary sources is as high as possible within the experimental setup, mainly because this improves the signal to noise ratio, which is beneficial for the identification of the transfer functions. Furthermore, a flat frequency response is desired, to allow for broadband experiments. In order to connect the external primary sources via tubes to the experimental setup, each driver is placed in an enclosure.

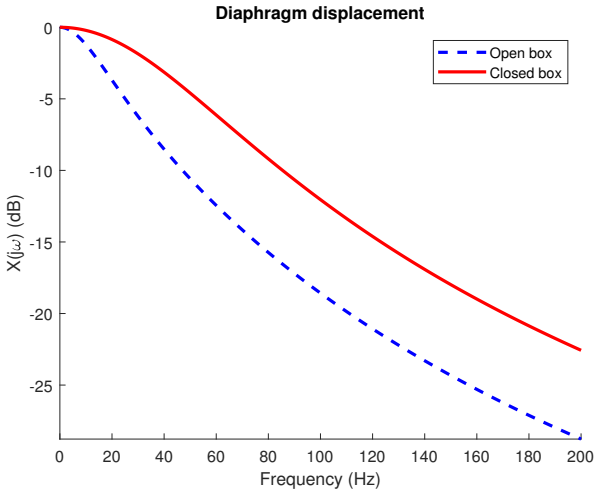

Figure 6.4: Cone displacement functions

.

Two driver enclosures have been tested, to see the effect of the volume size in front of the driver, not to be confused with the volume behind the driver, which is computed with the Thiele/Small parameters. The first design is shown in Fig. 6.5 and the second design is shown in Fig. 6.6. For this comparison the volume behind the driver would ideally have been kept constant, but has been changed due to a design update.

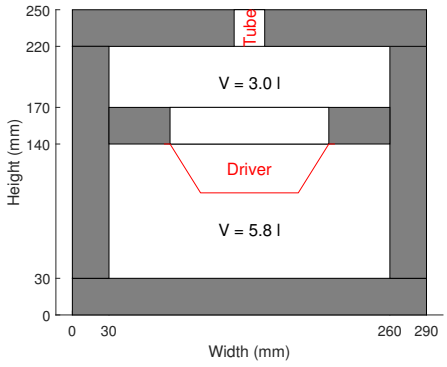

Figure 6.5: Primary source enclosure design 1, in which the tube and driver locations have been indicated in red.

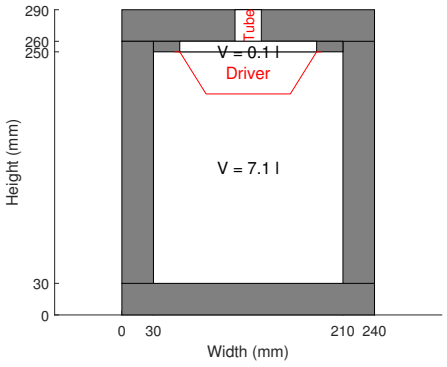

Figure 6.6: Primary source enclosure design 2, in which the tube and driver locations have been indicated in red.

In design 1, the volume in front of the driver is about 3.0 l, while in design 2 the volume in front of the driver is about 0.1 l. The FRF of both enclosures is shown in

Fig. 6.7. This measurement is conducted with a tube of 1 m connected to the enclosures, while a microphone is placed at the other end of the tube. The figure shows that design 2, with a small volume in front of the driver, achieves a higher SPL. Furthermore, it can be seen that the FRF of design 1 contains more noise, especially at the lower amplitudes. Due to the higher SPLs and better signal to noise ratio, design 2 has been chosen.

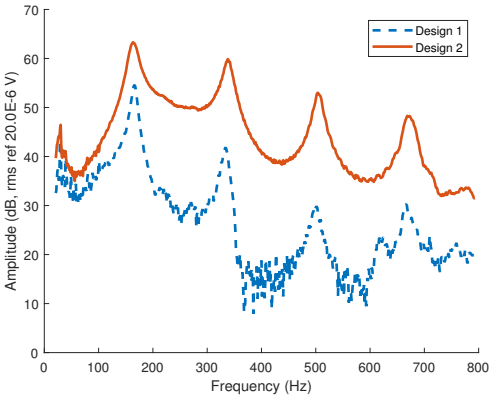

Figure 6.7: The frequency response functions of both primary source enclosures, connected to a tube of 1 m.

Now that the design with the highest sound pressure levels has been chosen, a flat frequency spectrum is required. Therefore, several measurements have been conducted with absorption material (melamine foam Basotect) at the end of the tube. The results of the measurements are shown in Fig. 6.8. A measurement without a tube is shown, of which the configuration is given in Fig. 6.9; a measurement with a tube but without any absorption is shown and measurements with the tube in combination with different absorption thickness added to the end of the tube are shown, an example of which is given in Fig. 6.10. A comparison of the measurement without a tube and the measurement with the tube without absorption shows the effect of the tube on the FRF. Furthermore, the figure shows that the addition of the absorption results in a flatter frequency spectrum. However, with increasing absorption thickness, the SPL decreases. Therefore, the absorption thickness of 1 cm is used in the experimental setup.

The locations of the tubes connected to the setup are shown in Fig. 6.11. The setup is equipped with a total of 39 KECG2240PBJ condenser microphones, of which $K = 12$ reference sensors, which are located at the coordinates $(x_r, y_r) = (\{r_s - h\}\cos\theta_r, \{r_s - h\}\sin\theta_r)$, in which $r_s = 0.24$ m, $\theta_r = 2\pi i/K$, $i = 0, \ldots, K-1$ and $h = 1.6$ cm. The 36 error microphones are placed at the coordinates $(x_e, y_e) = (\{r_s, r_s \pm h\}\cos\theta_e, \{r_s, r_s \pm h\}\sin\theta_e)$, in which $\theta_e = 2\pi i/L$, $i = 0, \ldots, L-1$, resulting in $L = 12$ error sensors on a circle with each three microphones aligned in radial direction. The inner error sensors and the reference sensors are the same physical microphones. With all the inner and outer microphones at the circle, the particle velocity is estimated using Eq. (3.27). With the middle microphones the acoustic pressure

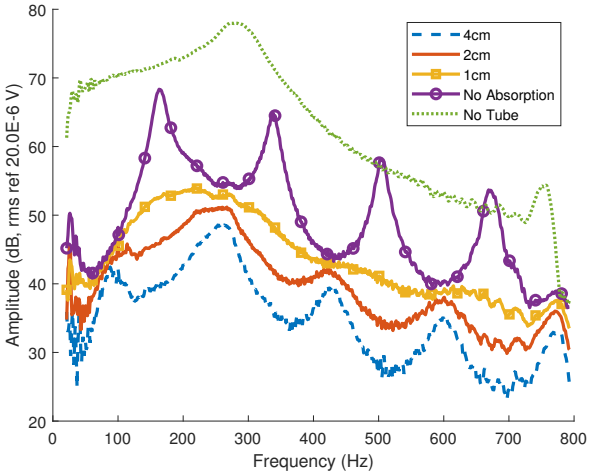

Figure 6.8: The frequency response functions of design 2 with a tube of length 1 m in combination with different absorption thickness at the end of the tube.

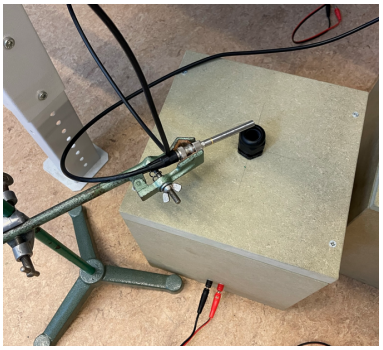

Figure 6.9: Primary source enclosure design 2, without a tube connected.

Figure 6.10: Primary source enclosure design 2, with a tube connected having 1 cm thick melamine foam at its end.

is measured. The particle velocity and acoustic pressure at the circle are the input for the KHI, with $\rho = 1.21$ kg/m^3 and $c = 343$ m/s, to compute the primary path $\mathbf{P}(z)$ and the secondary path $\mathbf{G}(z)$ at $L_{\text{perf}} = 21$ performance sensor locations, which are equally distributed within the ring of microphones with a distance of 0.0865 m from each other, as shown in Fig. 6.11. Similar to the configuration in Sec. 5.3, in order to prevent spatial aliasing, according to the Nyquist sampling [159] criterion, the maximal distance between any of the microphones is $d_{\max} = \frac{c}{2f_{\max}} = \frac{343}{1200} = 0.286$ m. This condition is satisfied for the performance sensors with a distance of 0.087 m and the error and reference sensors with a distance of 0.126 m. Furthermore, for accurate reconstruction of the secondary sound field, the secondary sources need to

satisfy this condition as well [50, 92], which is not perfectly met with a distance of 0.3 m owing to spatial limitations of the physical loudspeakers. Therefore, the maximum frequency for accurate secondary sound field generation lies at 570 Hz, rather than 600 Hz. However, it should be noted that the secondary sound field must be accurate within the circle, while it does not necessarily need to be accurate outside of the circle. This relaxes the spatial requirement, so that with $d_{\max} = 0.286$ m, six secondary sources would already be able to accurately generate the secondary sound field within the contour.

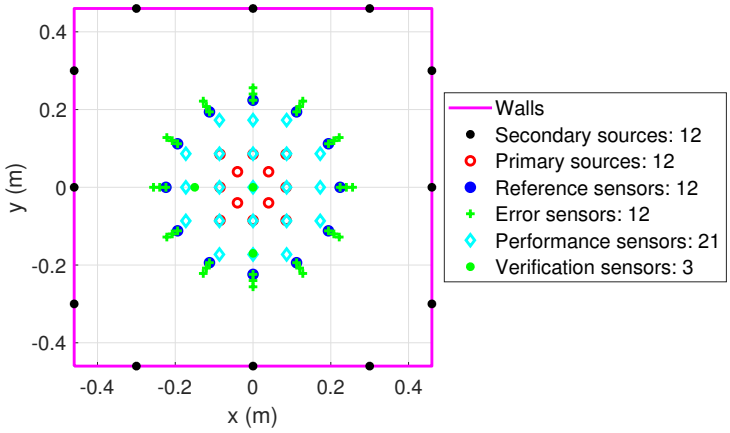

Figure 6.11: Two-dimensional schematic view of the experimental setup.

Out of the 39 microphones, the last three are the verification sensors, at $(x, y) = (-0.15, 0)$ m, $(0, 0)$ m and $(0, -0.17)$ m for sensors 1 to 3, respectively. The placement of the verification sensors is indicated in Fig. 6.11. The verification sensors measure the total acoustic pressure and are used to estimate the reverberation time (RT). All the physical microphones are individually calibrated using an Acoustical Calibrator B&K Type 4231, at 1 kHz with 94 dB sound pressure level re 20μPa. The calibration procedure is described in Appendix A.2. An overview of the system configuration is shown in Fig. 6.12, in which the 12 microphones at the inner ring are also used as reference microphones to measure the reference signals. The control system is a Speedgoat real-time target machine with an Intel Xeon 6-core CPU at 4 GHz and 128 GB of RAM. The machine is equipped with multiple IO135 modules, interconnected via their digital ports for synchronization. The microphones are connected to custom-made pre-amplifiers, of which the electrical scheme is shown in Appendix A.3, and which are connected to the control system. All the primary sources are connected to a Dayton Audio MA1240a multizone amplifier, which is connected to the control system. Similarly, all the secondary sources are connected to a second Dayton Audio MA1240a multizone amplifier, which is connected to the control system.

The Simulink scheme used for identification purposes is shown in Fig. 6.13. One after another, each source, both primary and secondary, is excited with a frequency

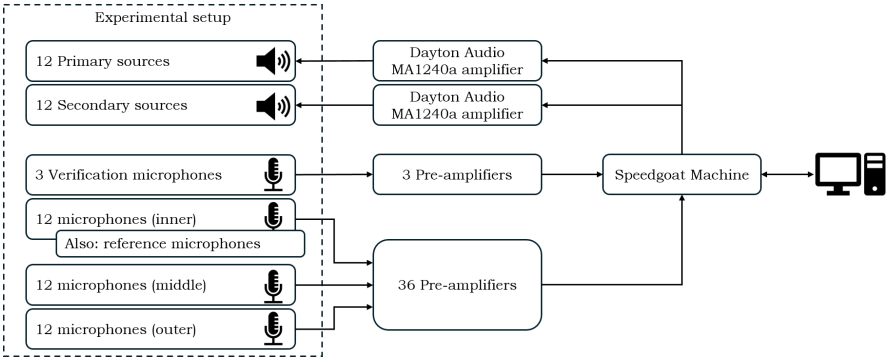

Figure 6.12: Active noise control system overview.

sweep. The details of the identification procedures are specified with each experiment in Sec. 6.3 and Sec. 6.4, because they differ per experiment. The excitation signals (inputs) and the measured acoustic pressures at all the microphones (outputs) are saved. With the recorded time history of both the inputs and outputs the impulse responses are computed. After the identification procedure, the KHI is evaluated. This results in the primary noise signal $\mathbf{d}(n) \in \mathbb{R}^{L_{\text{perf}} \times P}$, which is the output of the KHI with the primary sources active and the secondary signal $\mathbf{y}(n) \in \mathbb{R}^{L_{\text{perf}} \times P}$, which is the output of the KHI with the secondary sources active. With these signals, the control coefficients are computed following the configuration of Fig. 2.2.

The scheme used to do real-time control is shown in Fig. 6.16. The control coefficients are the input of block w, and the feedback path is modelled with block f, which was used to apply IMC. The subsystem 'Controller output' is shown in Fig. 6.19 and the subsystem 'Feedback path' is shown in Fig. 6.20. As can be seen, a delay of 1 sample has been added in the 'Feedback path', so as to prevent an algebraic loop. In order to compensate for this delay, the first sample of the FIR filter f has been removed, so this filter is time-advanced by 1 sample.

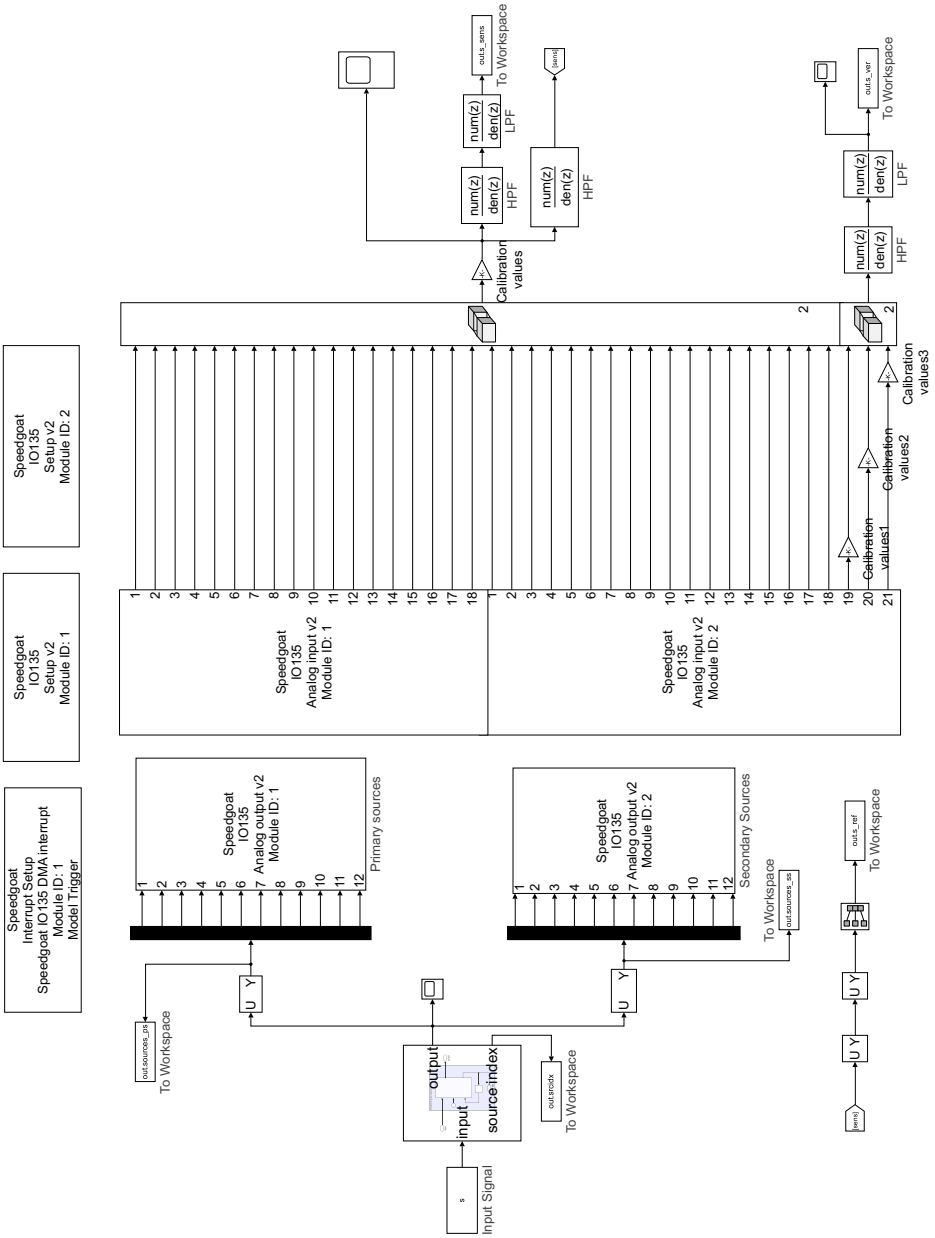

Figure 6.13: Simulink scheme of the system identification procedure. A zoom of the left side is shown in Fig. 6.14, a zoom of the right side is shown in Fig. 6.15.

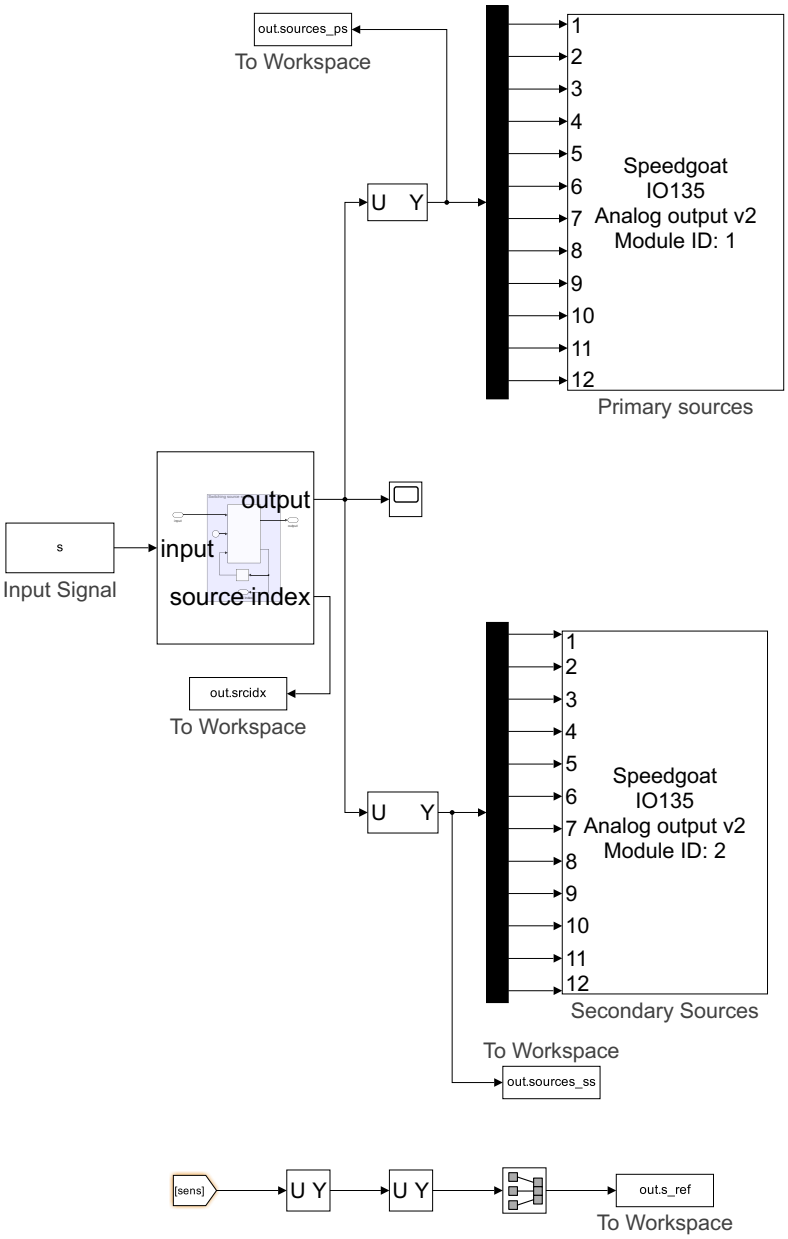

Figure 6.14: Zoom in on the left side of Fig. 6.13.

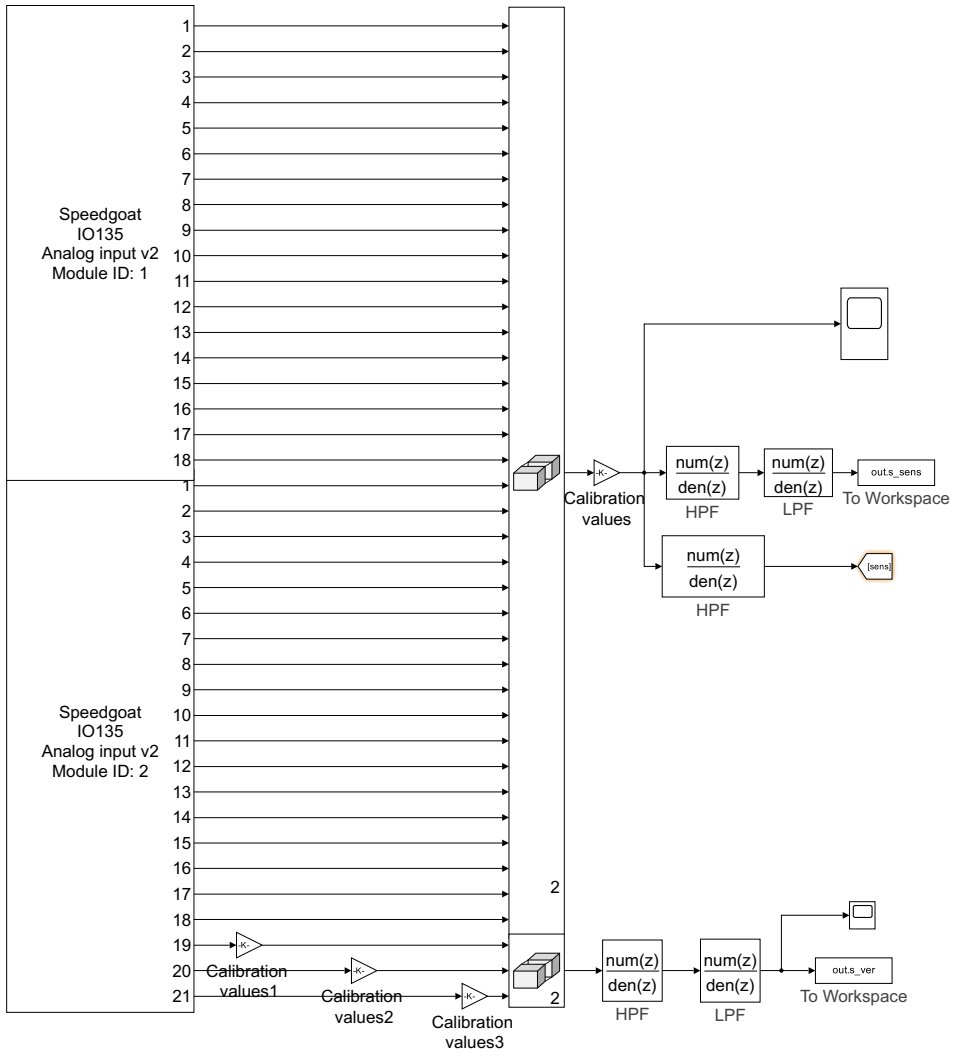

Figure 6.15: Zoom in on the right side of Fig. 6.13.

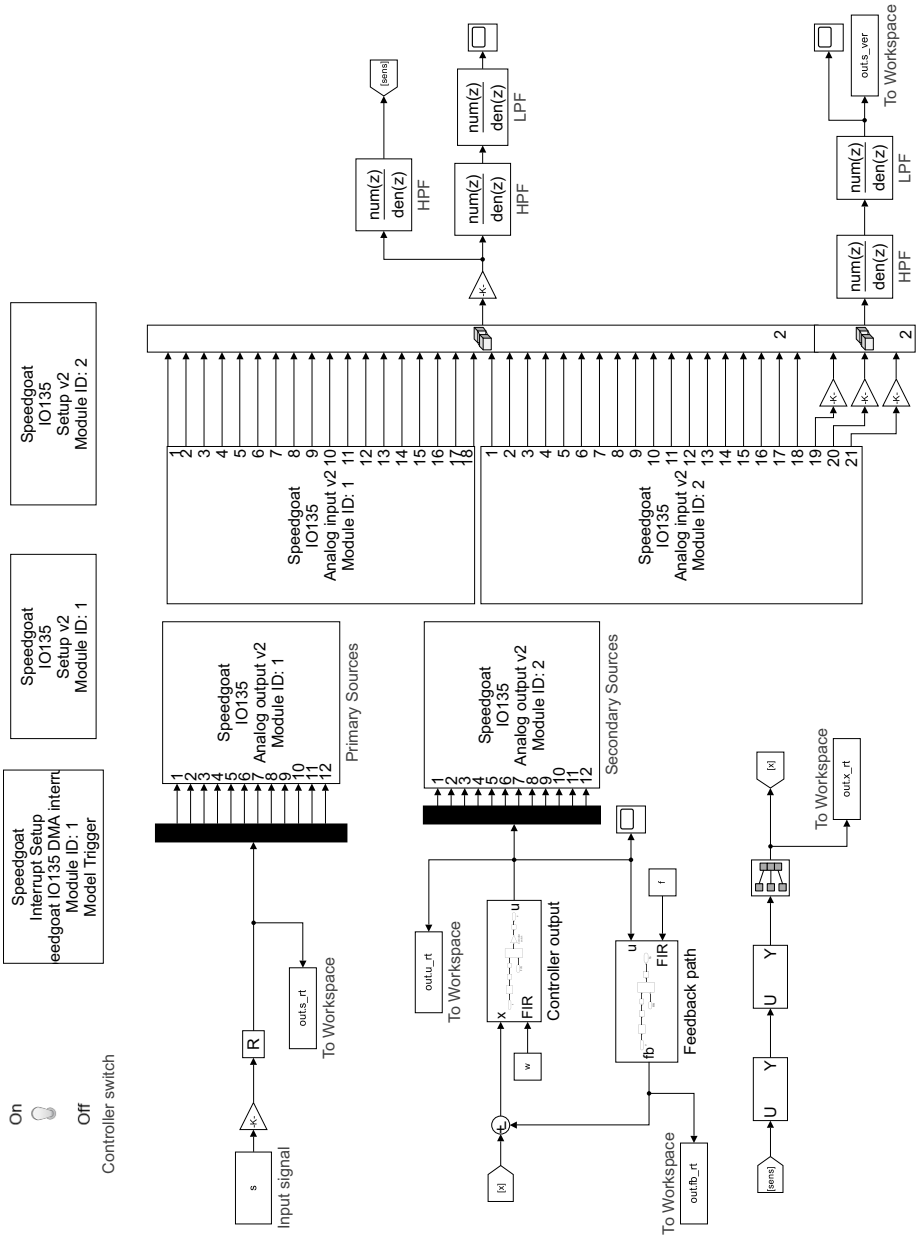

Figure 6.16: Simulink scheme of the real-time control. A zoom of the left side is shown in Fig. 6.17, a zoom of the right side is shown in Fig. 6.18. The subsystem 'Controller output' is shown in Fig. 6.19 and the subsystem 'Feedback path' is shown in Fig. 6.20.

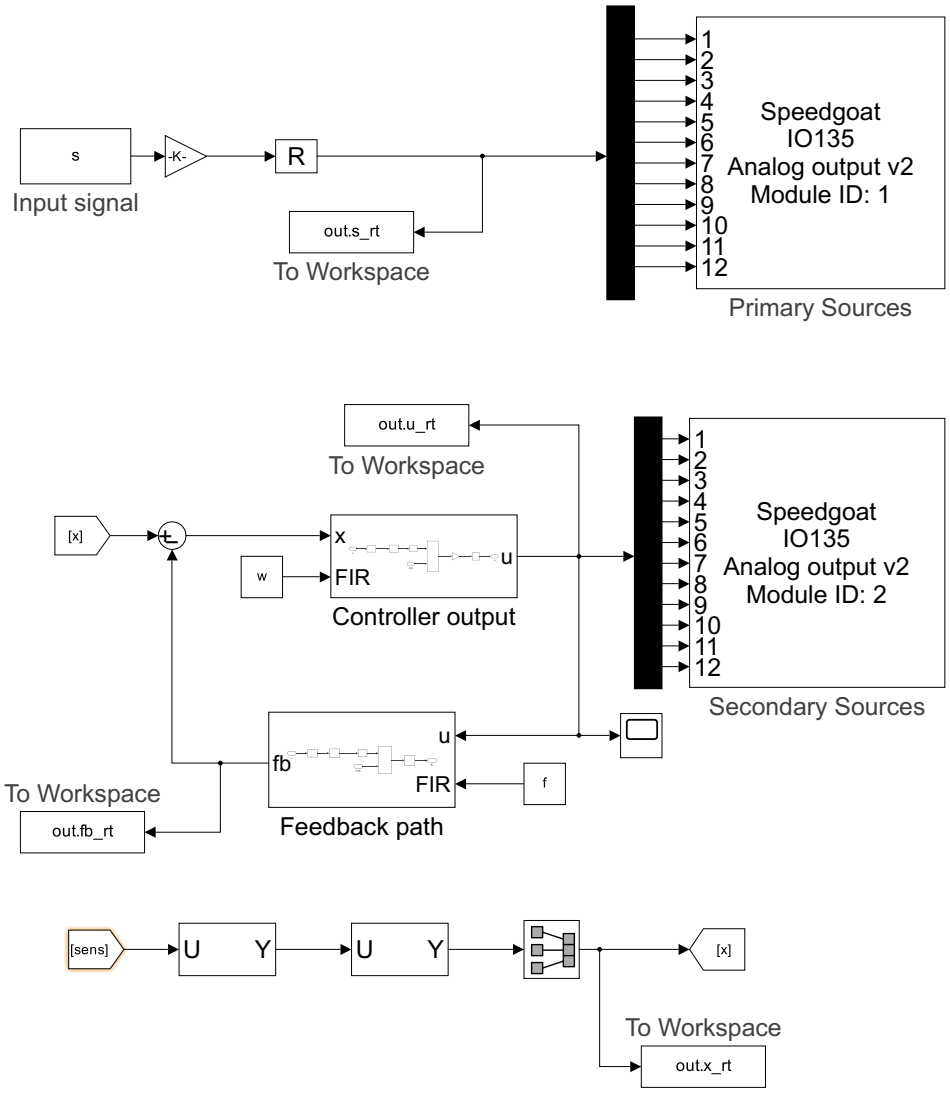

Figure 6.17: Zoom in on the left side of Fig. 6.16.

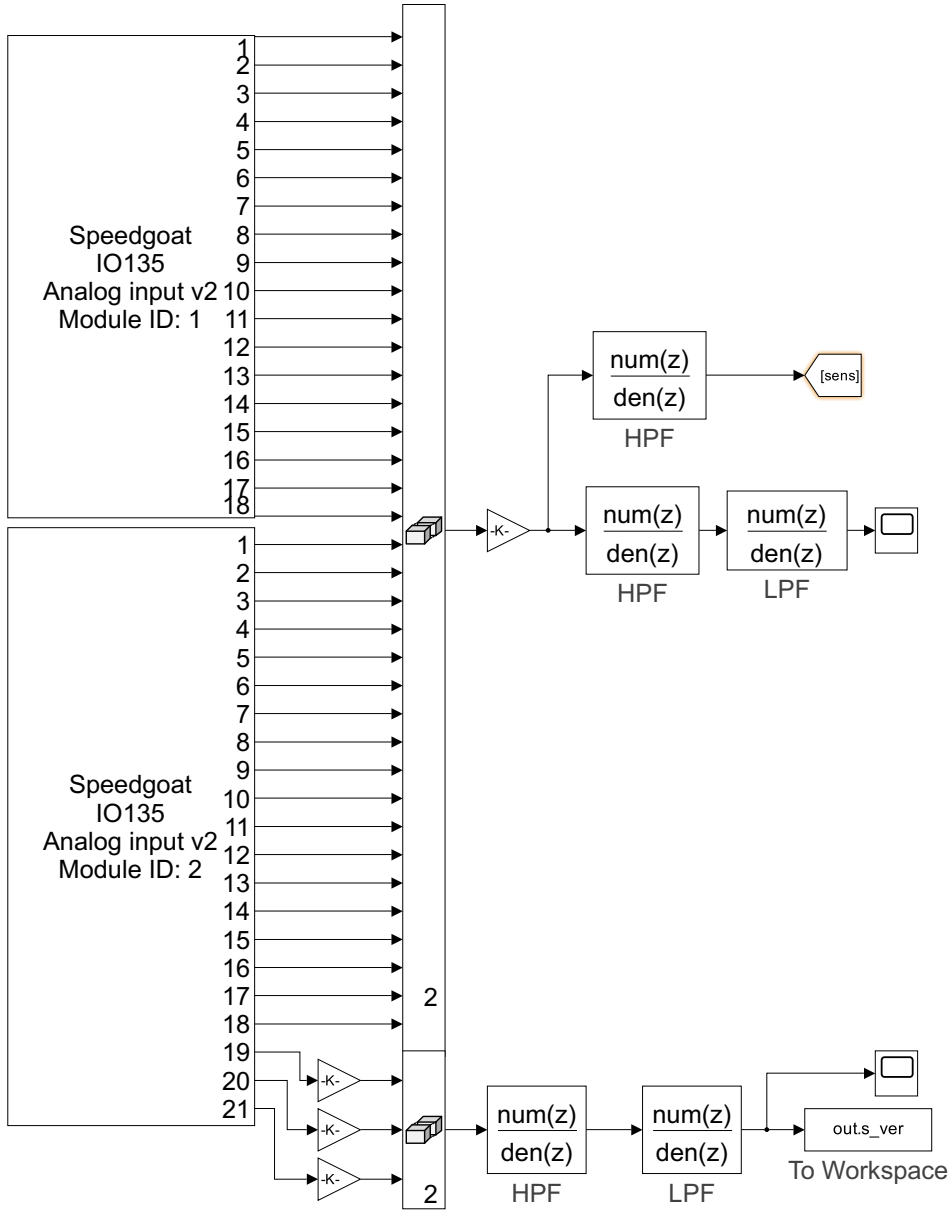

Figure 6.18: Zoom in on the right side of Fig. 6.16.

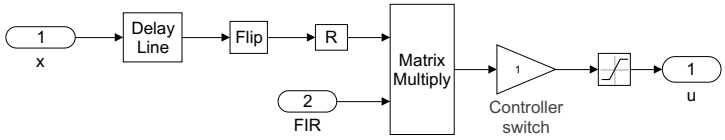

Figure 6.19: Subsystem 'Controller output' of the real-time control scheme.

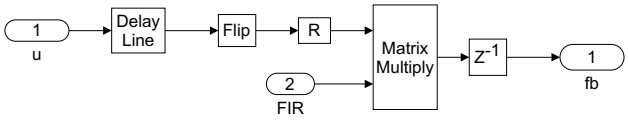

Figure 6.20: Subsystem 'Feedback path' of the real-time control scheme.

6.3 Real-time suppression of the reflected sound field with the PBC-CG algorithm

In this real-time experiment, the system runs at a sampling frequency of $f_s = 5$ kHz. The reference signals are filtered by a third-order high-pass filter having a cutoff frequency at 20 Hz. The error signals and verification signals are filtered by a third-order low-pass filter having a cutoff frequency at 600 Hz and a third-order high-pass filter with a cutoff frequency at 60 Hz. All individual sources generate a logarithmic sweep from 20 to 600 Hz for a duration of 10 s to identify the system. The impulse responses of the system are shown in Fig. 6.21. The left figure shows the primary path, from the primary sources to the error sensors, truncated to $P = 1024$ samples. The middle figure shows the secondary path, from the secondary sources to the error sensors, truncated to $J = 400$ samples. The right figure shows the feedback path, from the secondary sources to the reference sensors, truncated to $F = 700$ samples. The feedback path is used to apply IMC [44], the principle of which is explained in Sec. 2.2.3. The obtained impulse responses are transformed to the FRFs with the Fourier transform, which are shown in Appendix A.4.

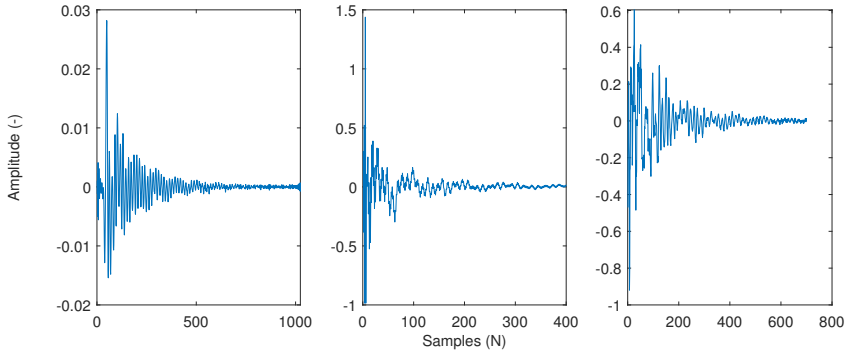

Figure 6.21: Impulse responses of the system. The left figure shows the impulse response of the primary path, from the first primary source to the first performance sensor. The middle figure shows the impulse response of the secondary path, from the first secondary source to the first performance sensor. The right figure shows the feedback path, from the first secondary source to the first reference sensor.

A set of control filter coefficients of length $I = 250$ samples is obtained after running the PBC-CG algorithm with 148 iterations, using a relative tolerance of $\epsilon = 1 \times 10^{-6}$, with the regularization parameter $\beta = 1 \times 10^{-1}$, which was found to be the smallest value for which the system remained stable. By setting the regularization parameter at this value, a stable system is maintained in combination with IMC. The regularization parameter was found in a heuristic manner. A physical interpretation of the regularization procedure is that uncorrelated white noise signals of mean-square value β are added to each of the reference signals [44]. Therefore,

The results presented in this section are published in [149].

increasing the regularization parameter reduces the performance. However, if the regularization parameter is not large enough in combination with IMC, the system is not stable because of the imperfections of the internal model. The PBC-CG algorithm required 102.5 s on a desktop computer with an Intel core i7 − 8700 @ 3.20 GHz CPU and 64 GB of RAM. The obtained filter coefficients are shown in Fig. 6.22, which shows that the filter coefficients have decayed after I samples.

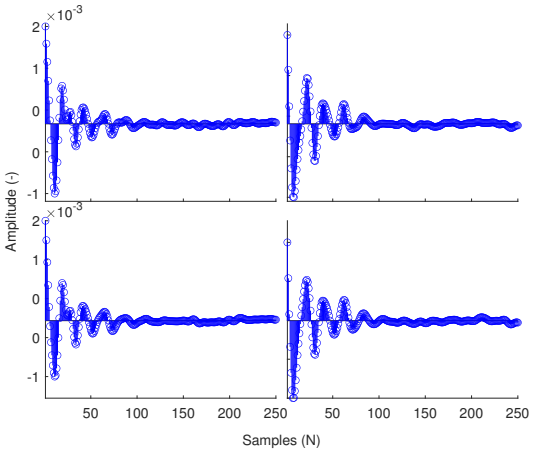

Figure 6.22: The control filter coefficients $\boldsymbol{W}(z)$ of length $I = 250$ samples. The filter coefficients correspond to reference sensors 1, 2 and secondary sources 1, 2. The other channels are omitted for the sake of readability.

During real-time control, each primary source generates an independent logarithmic sweep from 20 to 600 Hz, which is randomly varied in duration and starting time for each primary source.

The spectral density of the first four performance signals measured at the performance sensor locations is shown in Fig. 6.23. This shows that the controller reduces the signals, as computed by the KHI up to about 600 Hz, by an average of 9.6 dB. The spectral density of the signals measured by the verification sensors is shown in Fig. 6.24, which shows that the spectral density becomes increasingly flat. The impulse response from the primary sources to the verification sensors with and without control is shown in Fig. 6.25. The figures show that the amplitude of the impulse response is reduced with the controller turned on, although the active control system increases the noise floor, as can be seen when the impulse response has decayed.

The RT is estimated using the envelope of the impulse response, after which a moving average filter is applied using a window of ten samples, followed by the Schroeder integration method [111], using a time limit of 500 samples. To obtain the decay rate T10, which describes the time it takes for the sound pressure level to reduce by 10 dB [165], a linear regression is made from -5 dB to -15 dB. The regression starts at -5 dB in order to avoid the influence of direct sound or strong early reflections [166]. The decay rate T10 is shown in Fig. 6.26. Using the slope (A)

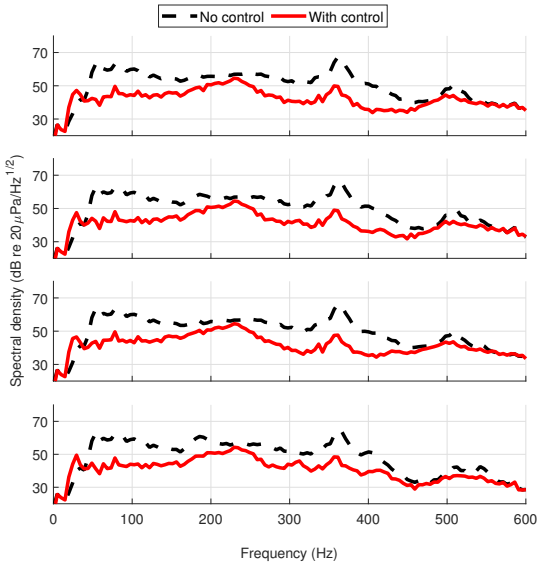

Figure 6.23: Spectral densities of the signals at the first four performance sensors. The reduction levels from top to bottom are 8.9, 10.2, 9.7 and 9.7 dB, respectively.

of the regression line, the RT is estimated following

$$RT = \frac{-60}{A}. \tag{6.10}$$

The RT has been reduced from 0.036 s to 0.022 s, 0.037 s to 0.016 s and 0.036 s to 0.020 s at verification sensors 1 to 3, respectively. The result of the KHI at $f = 215$ Hz is shown in Fig. 6.27 with the primary sources active and Fig. 6.28 with the secondary sources active, and the sum of both is shown in Fig. 6.29. From the sum of both fields it can be seen that global control of the area within the circle of microphones is achieved. It should be noted that the results of the KHI are not valid outside the contour, but the full domain is shown for completeness.

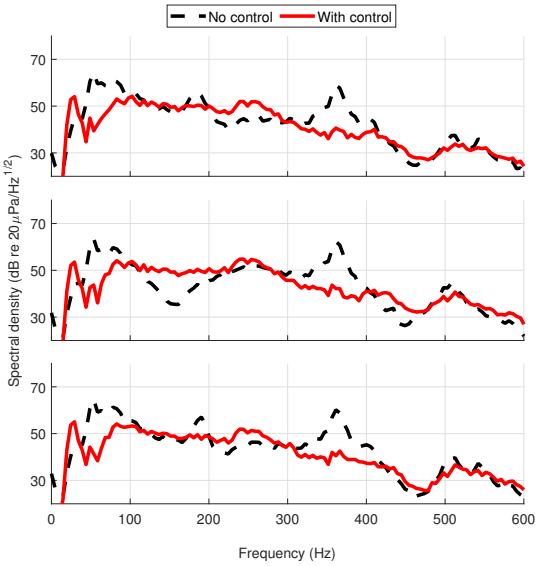

Figure 6.24: Spectral density of the signals measured by the verification sensors.

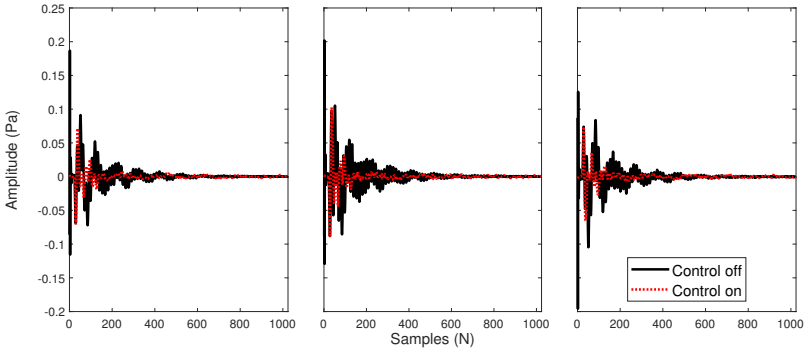

Figure 6.25: The impulse response from the primary sources to the verification sensors with the controller turned off and with the controller turned on.

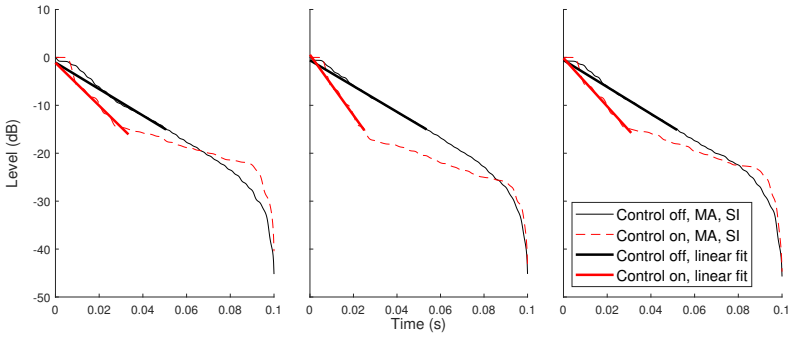

Figure 6.26: An estimation of the RT (T10) using a smoothed envelope of the impulse response. The left figure is the first verification sensor; without control the RT is 0.036 s and with control the RT is 0.022 s. The middle figure is the second verification sensor; without control the RT is 0.037 s and with control the RT is 0.016 s. The right figure is the third verification sensor; without control the RT is 0.036 s and with control the RT is 0.020 s.

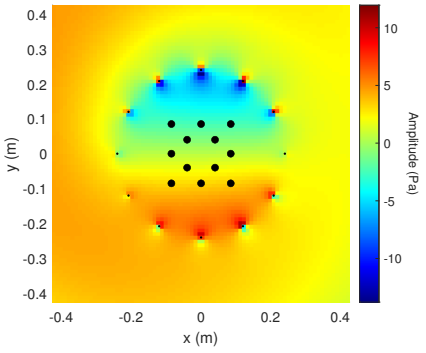

Figure 6.27: Real part of the output of the KHI at 215 Hz, with the primary sources active, located at the black dots. The result is valid only inside the contour.

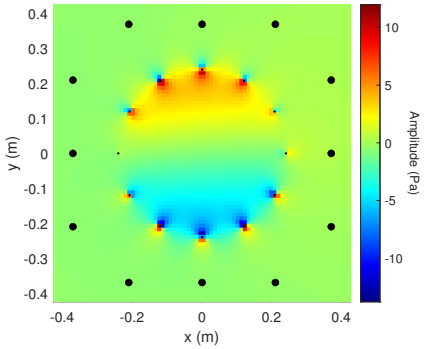

Figure 6.28: Real part of the output of the KHI at 215 Hz, with the secondary sources active, located at the black dots. The result is valid only inside the contour.

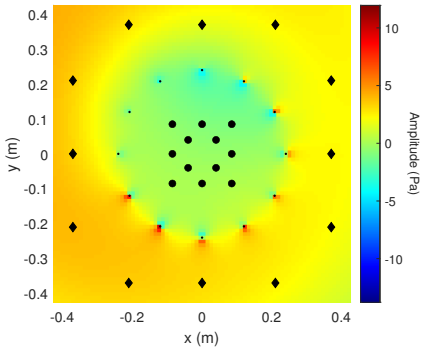

Figure 6.29: Sum of Figs. 6.27 and 6.28.

6.4 Real-time suppression of the reflected sound field with the CC-CG algorithm

In this real-time experiment the system runs at a sampling frequency of $f_s = 4$ kHz. The reference signals are filtered by a first-order high-pass filter with a cutoff frequency at 60 Hz. The performance signals and verification signals are filtered by a first-order low-pass filter with a cutoff frequency at 600 Hz and a first-order high-pass filter with a cutoff frequency at 60 Hz. During identification, all sources individually generate a logarithmic sweep from 60 to 2000 Hz for a duration of 10 s. The feedback path, secondary path and primary path are modelled with FIR filters, having lengths of 700, 1200 and 2000 samples, respectively. The model of the feedback path is used to apply internal model control [44].

With the CC-CG algorithm, using a regularization parameter $\beta = 1 \times 10^{-2}$ as shown in [162], and $N_{\text{FFT}} = 2048$ Fourier Transform samples, the set of control filters $\mathbf{W}(z)$ is computed, which is subsequently truncated to a length of $I = 500$ samples. The algorithm required 45 seconds on a desktop computer with an Intel Core i7 − 8700 @ 3.20 GHz CPU and 64 GB of RAM, to do 300 iterations. The convergence of the cost function is shown in Fig. 6.30.

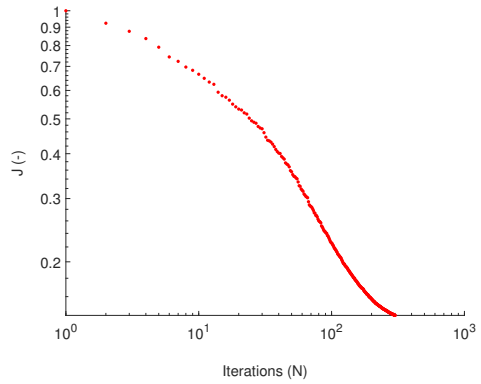

Figure 6.30: Convergence of the cost function while running the CG algorithm. Total elapsed time is 45 seconds.

During real-time control, each primary source generates an independent logarithmic sweep from 60 to 600 Hz, which is randomly varied in duration and starting time for each primary source. The spectral densities of the first four performance signals are shown in Fig. 6.31, which shows an average reduction of 9.4 dB.

The spectral densities of the signals measured by the verification sensors is shown in Fig. 6.32, which shows that resonances have been suppressed, resulting in a flatter spectrum.

The impulse response from the primary sources to the verification sensors with- and without control is shown in Fig. 6.33. The figures show that with the controller

The results presented in this section are submitted in [150].

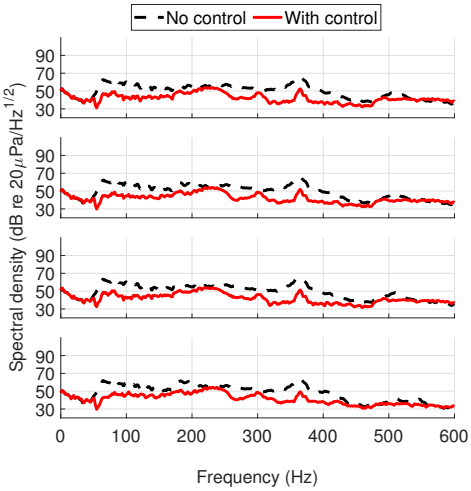

Figure 6.31: Spectral densities of the signals at the first four performance sensors. From top to bottom, the reduction levels are 9.7, 9.6, 9.3 and 9.0 dB, respectively.

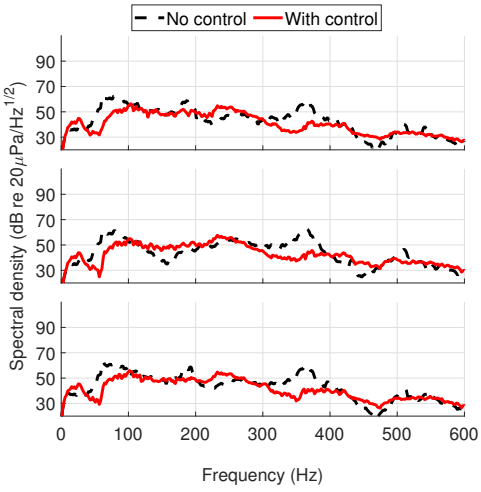

Figure 6.32: Spectral densities of the signals measured by the verification sensors.

turned on, the amplitude of the impulse response is reduced and the speed of decay is increased. Using the envelope of the impulse response, the RT is estimated. A moving average (MA) filter with a window of 20 samples is applied, followed by the Schroeder integration (SI) method [111], using a time limit of 500 samples. A first-order fit is made from -5 dB to -15 dB, resulting in an estimation of T10, as shown in Fig. 6.34. Similar to the procedure in Sec. 6.3, by using Eq. (6.10), the RT is estimated. The RT has been reduced from 0.037 s to 0.026 s, 0.036 s to 0.017 s and

0.036 s to 0.023 s at verification sensors 1 to 3, respectively.

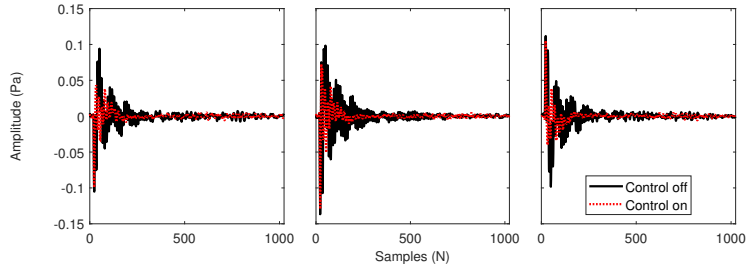

Figure 6.33: The impulse response from the primary sources to the verification sensors.

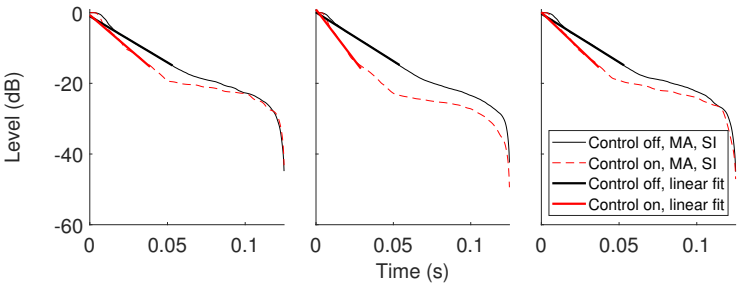

Figure 6.34: An estimation of the RT (T10) using a smoothed envelope of the impulse response. The left figure is the first verification sensor; without control the RT is 0.037 s and with control the RT is 0.026 s. The middle figure is the second verification sensor; without control the RT is 0.036 s and with control the RT is 0.017 s. The right figure is the third verification sensor; without control the RT is 0.036 s and with control the RT is 0.023 s.

6.5 Conclusion

In this chapter the real-time experiments of the developed methods are shown. First, the design process of the two-dimensional experimental setup is shown. Thereafter, the results of real-time control to suppress the reflections from the walls are shown. The reflected sound field due to the primary sources is computed with the KHI method, using microphones on a circle. The control coefficients have been computed with the PBC-CG algorithm and with the CC-CG algorithm. Despite small differences between the procedures used with each of the algorithms, it has been

shown that the reverberation time has effectively been reduced using the control coefficients computed with each of the algorithms.

Chapter 7

Conclusion

The primary goal of this work is to extend the operable frequency range of an acoustic anechoic chamber using an active control system that takes care of the lower frequency reflections. To achieve this, the first research objective is to develop a technique to compute the reflected sound field, a quantity that is not directly measurable. Given the geometric positioning of objects in a typical acoustic anechoic chamber, the Kirchhoff-Helmholtz integral is found to be the solution to the computation of the reflected sound field. This integral computes the sound field within a surface from measurements on that surface. If the sound-generating object is positioned inside this surface, the integral yields the reflected sound field, while for sources positioned outside the surface, it computes the total sound field. This property makes the Kirchhoff-Helmholtz integral well-suited for integration with typical feedforward control systems.

As the dimensions of the acoustic anechoic chamber increase and the wavelengths shorten, the number of sources and sensors required for effective active noise control grows rapidly. This results in an increase in computational complexity and memory consumption to compute the set of control filter coefficients. Therefore, the second research objective is to develop a method to compute a set of causal FIR control coefficients with reduced computational complexity and memory requirements. In this thesis three different algorithms are derived with a focus on reducing computational complexity and memory requirements. Each of these three algorithms have their pros and cons, listed as:

- The FD-RMFE algorithm applies -offline- least mean squares updates to converge to a set of control filters. To improve convergence speed, prewhitening, preconditioning and decoupling filters are applied. These filters are computed in the frequency domain and subsequently transformed to the time domain. However, the resulting filters are not necessarily causal, so a delay is required. Every filter is delayed by an appropriate number of samples, to ensure its causality. Although the delays can be truncated from the filter coefficients, it was found that this algorithm requires more time advance on the reference signals than the other two algorithms.

- The PBC-CG algorithm is a preconditioned conjugate gradient scheme, which applies block-circulant preconditioning to improve convergence speed. The algorithm is computed in the time domain, such that causality and frequency domain artifacts do not play a role. In comparison with the other two algorithms, this relaxes some conditions on the identification and implementation of the involved systems. However, this algorithm has been shown to have the highest computational complexity and memory requirements.

- The CC-CG algorithm is computed in the frequency domain, but causally constrained such that a set of causal control coefficients is obtained. Conjugate gradient iterations are applied, and in each iteration, the causal part of the gradient is preserved to update the set of control filter coefficients. This results in an algorithm with low computational complexity, without any artificial delays as compared with the FD-RMFE algorithm.

The third research objective is to conduct numerical studies to evaluate the effectiveness of the developed methods. The Kirchhoff-Helmholtz integral and the algorithms are used in numerical studies, in which the objective of the control system is to suppress the reflections from the walls. A small-scale numerical study with the FD-RMFE algorithm and a large-scale numerical study with the CC-CG algorithm are shown, in which the control system has been shown to effectively suppress the reflected sound field as computed with the Kirchhoff-Helmholtz integral.

The fourth and final research objective is to implement the developed techniques on an experimental setup so that real-time tests can be conducted. A small-scale experimental setup is built to test the developed methods in a two-dimensional configuration. Two separate real-time experiments are conducted in which the PBC-CG and CC-CG algorithms have been used to compute the control coefficients, with the objective of suppressing the reflections from the walls. The reflected sound field is computed with the Kirchhoff-Helmholtz integral, using a set of sensors on a circle. Each sensor is equipped with three microphones in radial direction. The outer two microphones are used to approximate the particle velocity. The results show that the reverberation time has been reduced significantly in both experiments.

While significant progress has been made, the journey towards a fully functional active acoustic anechoic chamber is not finished. The thesis is entitled 'Towards an active acoustic anechoic chamber', which reflects the substantial advancements made, but further work is necessary. To do so, future research could be oriented to the following non-exhaustive list of topics:

- The most important point is the extension towards real-time applications in three dimensions, to allow implementation in full-scale existing acoustic anechoic chambers. The three-dimensional Kirchhoff-Helmholtz integral equation is given in Sec. 3.4, which should be discretized to allow practical implementation.

- The effect of the presence of the secondary sources in the higher frequency range is not studied in this work. Because the control system is operating in the low frequency range, the presence of the secondary sources may lead to increased reflections at higher frequencies.

- In this work only microphones are considered. Therefore a particle velocity approximation method is required and used in this work. However, particle velocity sensors [99] and acoustic vector sensors [98] are commercially available, which may allow for more accurate low-frequency measurements and may allow the lower frequency limit to be decreased even further.
- The optimal source and sensor placement [167] is not considered in this work. In most applications, sources and sensors have an optimal placement which might allow the number of required sources and sensors to be reduced without any reduction in performance.
- Related to the previous point, in this work a procedure to minimize the number of sources and sensors [168] is not considered. In general, a minimal number of sources and sensors is required based on the wavelength, dimensions, etc. However, in some cases a smaller number of sources and sensors can be used, for example if they are placed at optimal positions. The benefit of this is that by reducing the number of sources and sensors the real-time computational complexity is reduced as well.
- The algorithms derived in this thesis are designed to compute a set of control filters for centralized architectures. However, a distributed control approach [47] may be worth exploring to reduce the number of connections, as shown in [162].
- It might be interesting to consider the application of virtual sensors [169, 170] in situations where the placement of a physical microphone is not possible or is not desired. If, for example, it is not possible to place physical microphones on a surface within the chamber, virtual sensors might be a solution to determining the particle velocity and the acoustic pressure at the desired locations.
- Instead of using the Kirchhoff-Helmholtz integral to compute the reflected sound field due to the primary sources, it might be possible to apply a multidimensional deconvolution method [80] to compute the Green's function of the reflected sound field. However, this Green's function may need to be recomputed when changing or repositioning the object to be studied.
- Optimizing the stability and performance trade-off, in particular regarding uncertainty and the feedback loop.

Finally, improvements to the algorithms might broaden their applicability, which could be in the following directions:

- The FD-RMFE algorithm uses prewhitening and preconditioning filters that are derived in the frequency domain. Currently, a delay is introduced in each filter to ensure its causality, which is possible in offline applications, because the noise signal can be delayed by an arbitrary number of samples. However, if a causal constraint is applied on the filters or on the control coefficient updates, delays might be unnecessary. In that case, the algorithm might be applicable in an online approach.

- The algorithms in this thesis have been applied with the objective of suppressing reflections from the walls. However, the algorithms could be used in a broader application range. An interesting direction might be the implementation of disturbance dependent weighting [153], which could be relevant in certain applications such as room acoustics.

Appendix A

Appendices

A.1 Computing the reflected sound field with the finite element method

This part of the appendix shows an example of how the reflected sound field is computed with the finite element method (FEM). The results of the FEM are obtained in COMSOL 6.2 with the Acoustics Module, using at least four quadratic elements per wavelength. The reflected sound field $p_{\text{scat}}(\mathbf{x}, \omega)$ due to an acoustic source in the domain is computed with the FEM as

$$p_{\text{scat}}(\mathbf{x}, \omega) = p_{\text{tot}}(\mathbf{x}, \omega) - p_{\text{dir}}(\mathbf{x}, \omega), \tag{A.1}$$

in which $p_{\text{tot}}(\mathbf{x}, \omega)$ is the total acoustic pressure and $p_{\text{dir}}(\mathbf{x}, \omega)$ is the acoustic pressure due to the direct field at radial frequency ω. An example of computing $p_{\text{scat}}(\mathbf{x}, \omega)$ is shown with the following figures. Fig. A.1 shows the total sound field, Fig. A.2 shows the direct sound field, which is computed with a perfectly matched layer at the edges of the domain, and Fig. A.3 is $p_{\text{scat}}(\mathbf{x}, \omega)$, computed following Eq. (A.1).

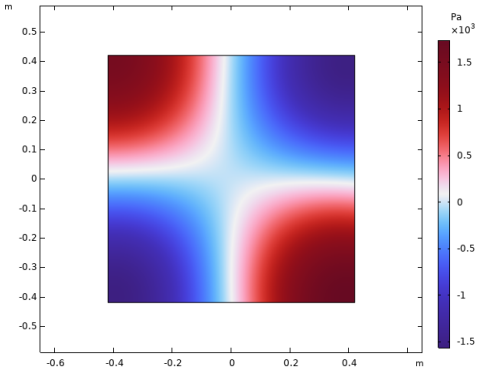

Figure A.1: Real part of the total sound field ($p_{\text{tot}}(\mathbf{x}, \omega)$) computed with the FEM at 301 Hz.

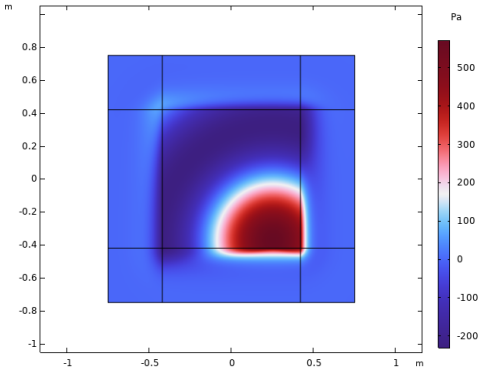

Figure A.2: Real part of the direct sound field ($p_{\text{dir}}(\mathbf{x}, \omega)$) computed with the FEM at 301 Hz.

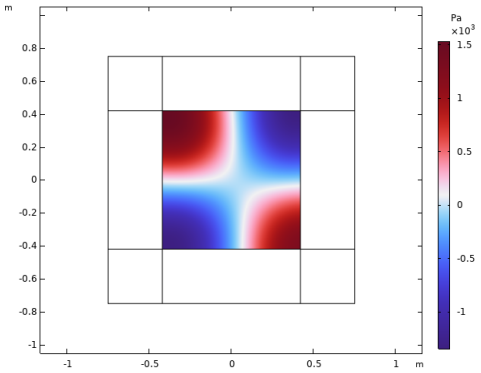

Figure A.3: Real part of the reflected sound field ($p_{\text{scat}}(\mathbf{x}, \omega)$) computed with the FEM at 301 Hz.

A.2 Calibration procedure for the microphones

The calibration of the microphones in the experimental setup has been done individually for each microphone. A guide is used which places the calibration device (Acoustical Calibrator B&K Type 4231) on a single microphone, as shown in Fig. A.4. The microphone is calibrated at 1000 Hz at 94 dB sound pressure level re 20μPa. This procedure is repeated for each microphone.

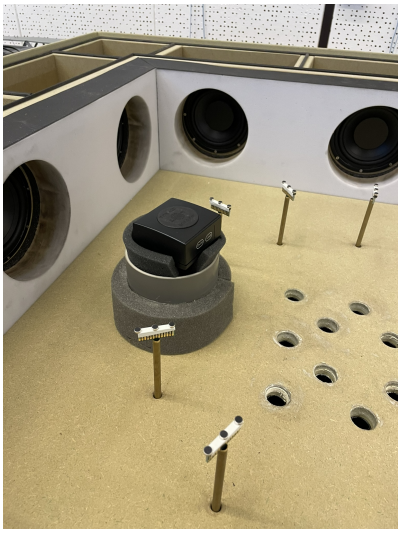

Figure A.4: Calibration procedure for all individual microphones.

The microphones are connected to a desktop running Sound and Vibration Measurement System v4.2 (see Fig. A.5), which determines the calibration values in mV/Pa.

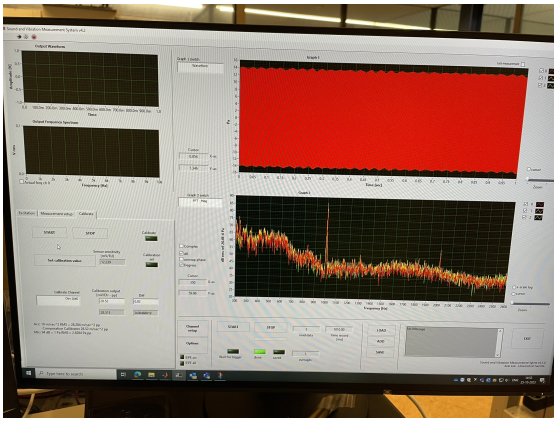

Figure A.5: Software used to determine the calibration values.

A.3 Custom microphone pre-amplifiers

This section shows the electrical scheme of the microphone pre-amplifiers in Fig. A.6. Each pre-amplifier allows up to three microphones to be connected, which together form one sensor on the contour to compute the KHI. Every sensor on the contour in the setup therefore has its own pre-amplifier.

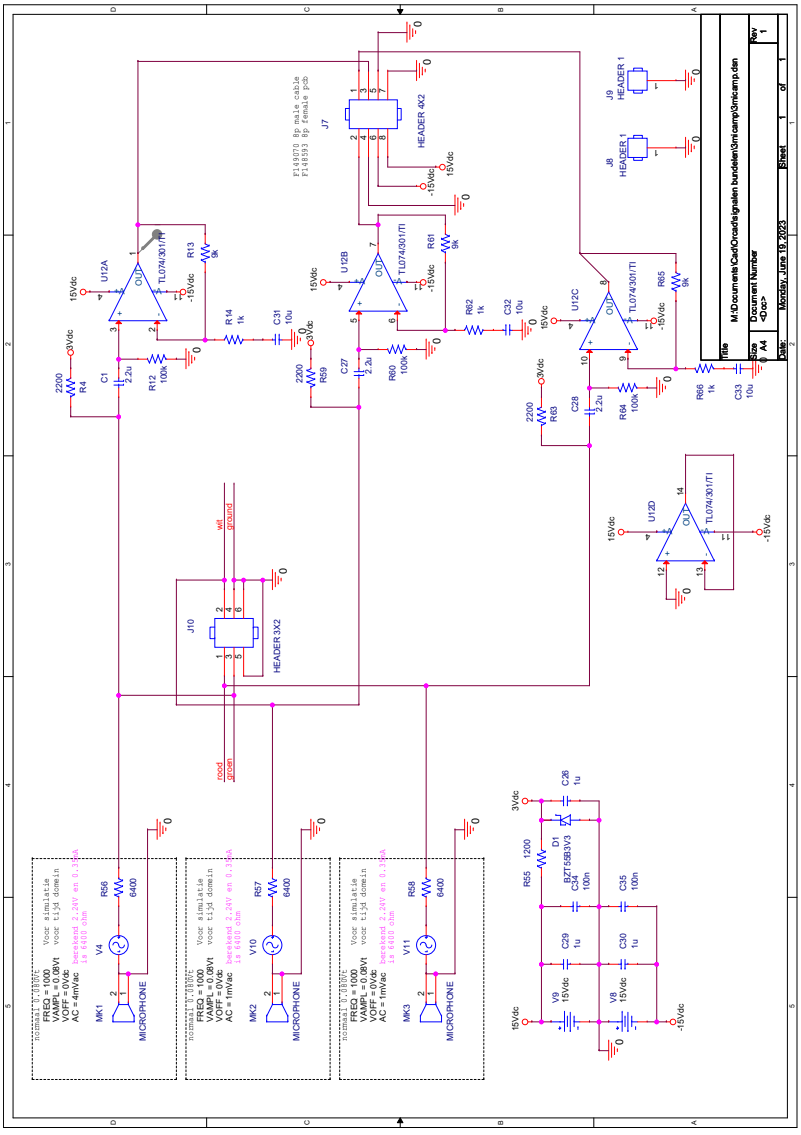

Figure A.6: Electrical scheme of the microphone pre-amplifiers.

A picture of all pre-amplifiers connected to the setup is shown in Fig. A.7, for a total of 12 pre-amplifiers, connected to 12 sensors on the contour, with each sensor

having 3 microphones in radial direction.

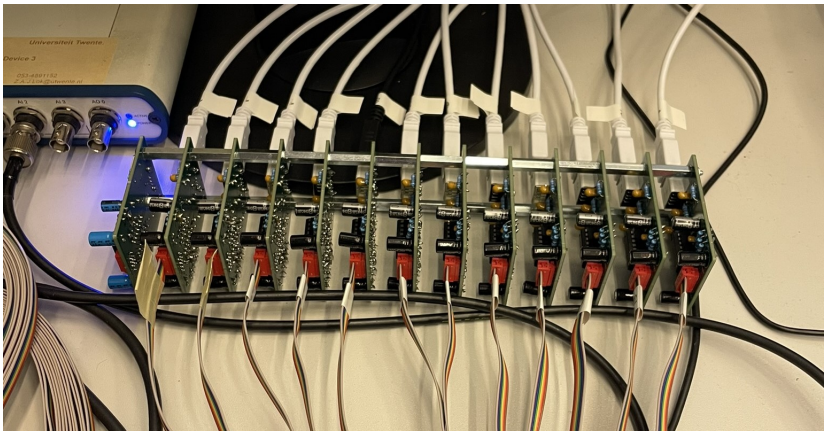

Figure A.7: The microphone pre-amplifier printed circuit boards.

A.4 Frequency response functions of the experimental setup

After the system identification procedure in Sec. 6.3, the frequency response functions (FRFs) of the setup are computed, which are shown in this section of the appendix. The FRF of the first primary source to the microphones at the first sensor is shown in Fig. A.8. In this figure, p_1 is the inner microphone at $\{x, y\} = (r_s - h)\{\cos 0, \sin 0\}$, p_2 is the middle microphone at $\{x, y\} = r_s\{\cos 0, \sin 0\}$ and p_3 is the outer microphone at $\{x, y\} = (r_s + h)\{\cos 0, \sin 0\}$, in which $r_s = 0.24$ m and $h = 1.6$ cm.

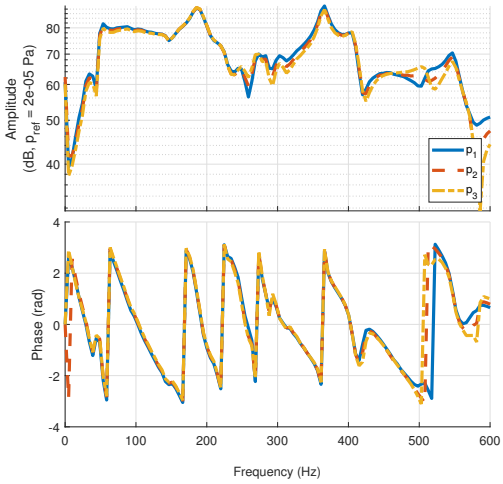

Figure A.8: Frequency response functions of the first primary source to the microphones at the first sensor.

With the pressure at all 36 microphones on the circle, the Kirchhoff-Helmholtz integral (KHI) is computed at the performance sensors. The FRF of the first primary source to the first performance sensor is shown in Fig. A.9.

Similarly, the FRF of the first secondary source to the microphones at the first sensor is shown in Fig. A.10. In this figure, p_1 is the inner microphone at $\{x, y\} = (r_s - h)\{\cos 0, \sin 0\}$, p_2 is the middle microphone at $\{x, y\} = r_s\{\cos 0, \sin 0\}$ and p_3 is the outer microphone at $\{x, y\} = (r_s + h)\{\cos 0, \sin 0\}$.

With the pressure at all 36 microphones on the circle, the KHI is computed at the performance sensors. The FRF of the first secondary source to the first performance sensor is shown in Fig. A.11.

The FRF of the first primary and first secondary source to the first reference sensor located at $\{x, y\} = (r_s - h)\{\cos 0, \sin 0\}$ is shown in Fig. A.12.

Lastly, the FRF of the first primary source to the first verification sensor located at $(x, y) = (-0.15, 0)$ is shown in Fig. A.13.

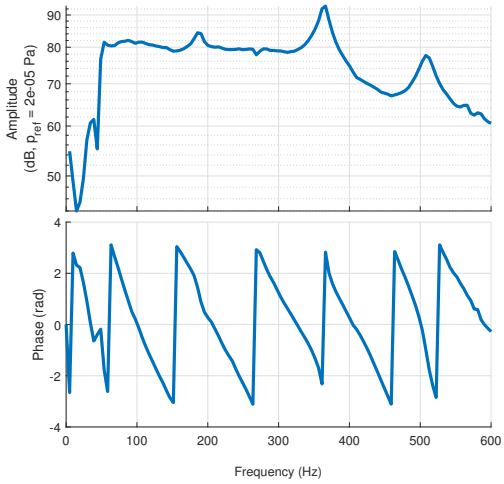

Figure A.9: Frequency response function of the first primary source to the first performance sensor.

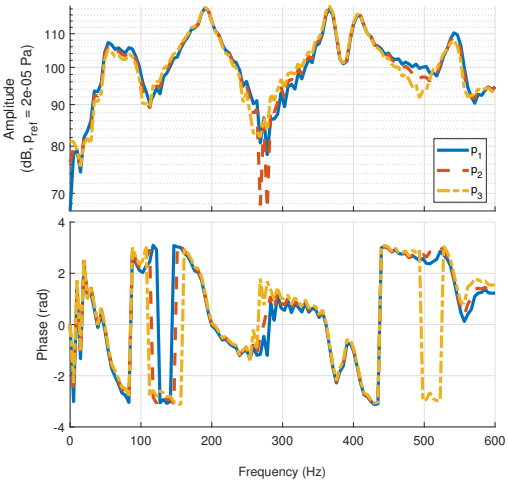

Figure A.10: Frequency response functions of the first secondary source to the microphones at the first sensor.

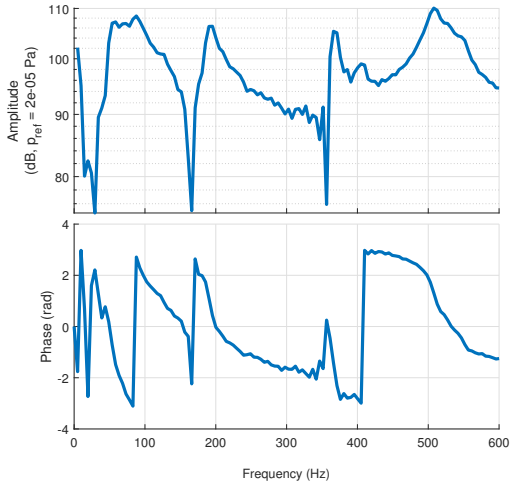

Figure A.11: Frequency response function of the first secondary source to the first performance sensor.

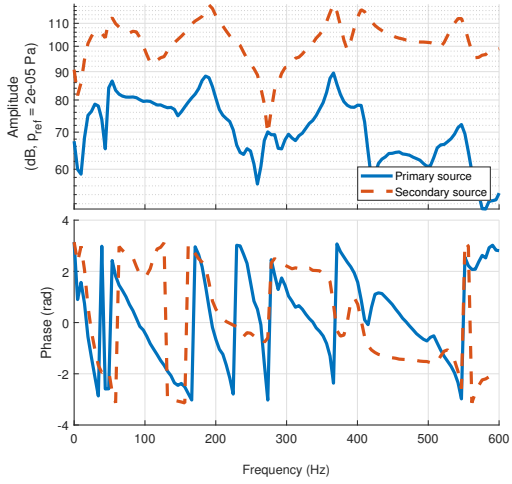

Figure A.12: Frequency response functions of the first primary and secondary source to the first reference sensor.

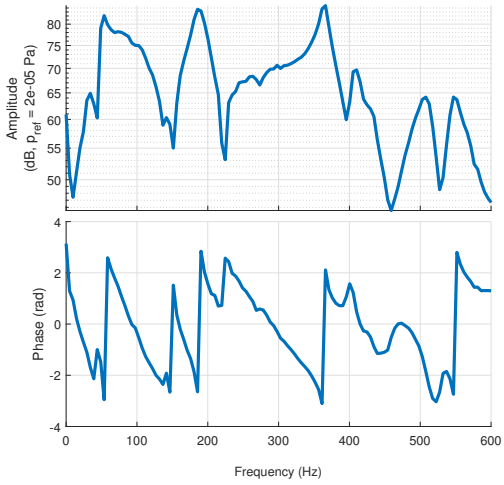

Figure A.13: Frequency response function of the first primary source to the first verification sensor.

Nomenclature

Abbreviations

dB	Decibel
AAC	Acoustic anechoic chamber
ANC	Active noise control
CC-CG	Causally constrained conjugate gradient algorithm
CG	Conjugate gradient
CNN	Convolutional neural network
EVD	Eigenvalue decomposition
FeLMS	Filtered-error least mean squares
FxLMS	Filtered-reference least mean squares
FD-RMFE	Frequency domain regularized modified filtered-error algorithm
FEM	Finite element method
FFT	Fast Fourier transform
FIR	Finite impulse response
FRF	Frequency response function
Hz	Hertz
IBC	Immersive boundary condition
IIR	Infinite impulse response
IMC	Internal model control
KHI	Kirchhoff-Helmholtz integral
LMS	Least mean squares
LTI	Linear time-invariant
MDD	Multidimensional deconvolution
MIMO	Multiple-input, multiple-output
PBC-CG	Preconditioned block-circulant conjugate gradient algorithm
PCG	Preconditioned conjugate gradient
PSD	Power spectral density
RLS	Recursive least squares

RT	Reverberation time
SISO	Single-input, single-output
SPL	Sound pressure level
SVD	Singular value decomposition

Mathematical notations

$\mathbb{C}$	Set of complex numbers
$\mathrm{E}[\cdot]$	Expectation operator
$\mathcal{F}(\cdot)$	Fourier transform
$\mathcal{F}^{-1}(\cdot)$	Inverse Fourier transform
$\mathcal{I}(\cdot)$	Imaginary part of $(\cdot)$
$\mathcal{J}$	Cost function
$\mathcal{J}_k$	Cost function at iteration k
$\mathcal{R}(\cdot)$	Real part of $(\cdot)$
$\mathbb{R}$	Set of real numbers
tr.	Trace operator
$\mathcal{U}_{(a,b)}$	Uniform distribution on the interval (a, b)
x	Scalar
$\mathbf{x}$	Vector
$\boldsymbol{x}, \boldsymbol{X}$	Matrix
∇	Gradient operator: $\nabla = \frac{\partial}{\partial x}\mathbf{i} + \frac{\partial}{\partial y}\mathbf{j} + \frac{\partial}{\partial z}\mathbf{k}$
∇^2	Laplace operator: $\nabla^2 = \frac{\partial^2}{\partial x^2} + \frac{\partial^2}{\partial y^2} + \frac{\partial^2}{\partial z^2}$
$\mathrm{diag}(x_1, x_2, \ldots, x_n)$	An n-by-n diagonal matrix with the elements $x_1, x_2, \ldots, x_n$ on its diagonal
∞	Infinity
∂	Partial derivative
$\in$	Belongs to
$\cdot$	Inner product
$(\cdot)^{-1}$	Matrix inverse
$(\cdot)^T$	Matrix transpose
$(\cdot)^*$	Complex conjugate
$(\cdot)^H$	Hermitian (complex conjugate) transpose
$(\cdot)_F$	Frobenius norm
$\{\cdot\}_+$	Causality constraint

Latin Letters

c	Speed of sound
$\boldsymbol{d}$	Disturbance signal
e	Euler's number
$\boldsymbol{e}$	Error signal
f	Frequency
f_c	Driver resonance frequency within an enclosure
f_o	Driver resonance frequency
f_s	Sampling frequency
h	Distance between two microphones in radial direction

j	Imaginary constant $\mathrm{j} = \sqrt{-1}$
k	Wave number
n	Sample moment
$\mathbf{n}$	Normal vector
p	Acoustic pressure
$\boldsymbol{p}_k$	Conjugate gradient directions at iteration k in PBC-CG algorithm
$\boldsymbol{r}$	Filtered reference signal
t	Time
$\boldsymbol{u}$	Control output signal
$\mathbf{v}$	Particle velocity
$\boldsymbol{x}$	Reference signal
$\boldsymbol{y}$	Secondary signal
z	forward shift operator
$\boldsymbol{F}$	Prewhitening filter
G	Green's function
$\boldsymbol{G}$	Secondary path transfer function matrix
$H_a^{(b)}$	Hankel function of kind b and order a
I	Number of FIR coefficients in the controller matrix
$\boldsymbol{I}$	Identity matrix
J	Number of FIR coefficients in secondary path matrix
J_a	Bessel function of the first kind of order a
K	Number of reference sensors
L	Number of error sensors
L_{perf}	Number of performance sensors
M	Number of secondary sources
O	Number of FIR coefficients in the prewhitening filter matrix
P	Number of primary sources
$\boldsymbol{P}$	Primary path transfer function matrix
R	Radius
$\boldsymbol{R}(n)$	Matrix of filtered reference signals at sample moment n
$\boldsymbol{R}_k$	Residual at iteration k in the PBC-CG algorithm
$\boldsymbol{S}$	Spectral density matrix
$\boldsymbol{T}$	Toeplitz matrix
$\boldsymbol{T}_B$	Toeplitz-block matrix
$\boldsymbol{U}$	Left singular vector matrix
V	Volume
V_n	Particle velocity in normal direction
$\boldsymbol{V}$	Right singular vector matrix
$\boldsymbol{W}$	Matrix of control coefficients
$\boldsymbol{X}$	Reference path transfer function matrix
Y_a	Bessel function of the second kind of order a

Greek letters

α	Step size in FD-RMFE algorithm

α_k	Steepest descent direction at iteration k in the PBC-CG algorithm
β	Regularization coefficient
δ	Dirac delta function
Δ	Delay operator
ϵ	Tolerance parameter
η	Noise parameter
η_k	Variational parameter at iteration k in the CC-CG algorithm
κ	Noise scaling factor
ξ	Discrete frequency bin number
π	Pi
ρ	Density of the acoustic medium
ω	Angular frequency
$\mathbf{\Sigma}$	Singular values matrix

Remark: The above list of most important symbols and letters is non-exhaustive. Throughout this thesis the meaning of newly introduced symbols is always given.

References

[1] Y. Osada. An overview of health effects on noise. *Journal of Sound and Vibration*, **127**(3):407–410, 1988.

[2] L. de Santana, M. P. Sanders, C. H. Venner, and H. W. Hoeijmakers. The UTwente aeroacoustic wind tunnel upgrade. In *2018 AIAA/CEAS Aeroacoustics Conference*, pp. 1–7, Atlanta, Georgia, 2018.

[3] F. A. Everest and K. Pohlmann. *Master Handbook of Acoustics*. McGraw-Hill Education, New York, 2009.

[4] Q. Xu and Y. Huang. *Anechoic and Reverberation Chambers: Theory, Design, and Measurements*. IEEE Press. Wiley, Chichester, West Sussex, 2019.

[5] Acoustics - Determination of sound power levels and sound energy levels of noise sources using sound pressure - Precision methods for anechoic rooms and hemi-anechoic rooms. ISO 3745:2012 standard, International Organization for Standardization, Geneva, CH, 2012.

[6] K. Sozanski and A. Sozanska. Low frequency loudspeaker measurements using an anechoic acoustic chamber. In *2018 Signal Processing: Algorithms, Architectures, Arrangements, and Applications (SPA)*, pp. 367–372, Poznan, Poland, 2018. IEEE.

[7] R. Bolejko, A. Dobrucki, and P. Plaskota. Design of acoustic chamber for loudspeaker measurements. In *2018 Joint Conference - Acoustics*, pp. 1–4, Ustka, Poland, 2018. IEEE.

[8] T. A. Ricketts. Directional hearing aids. *Trends in Amplification*, **5**(4):139–176, 2001.

[9] V. F. Kopiev, V. V. Palchikovskiy, I. V. Belyaev, Yu. V. Bersenev, S. Yu. Makashov, I. V. Khramtsov, I. A. Korin, E. V. Sorokin, and O. Yu. Kustov. Construction of an anechoic chamber for aeroacoustic experiments and examination of its acoustic parameters. *Acoustical Physics*, **63**(1):113 – 124, 2017.

[10] C. Sujatha. Fundamentals of acoustics. In *Vibration, Acoustics and Strain Measurement: Theory and Experiments*, pp. 161–217. Springer International Publishing, Cham, 2023.

[11] E. Frederiksen. Microphone calibration. In D. Havelock, S. Kuwano, and M. Vorländer, editors, *Handbook of Signal Processing in Acoustics*, pp. 1293–1312. Springer New York, New York, 2008.

[12] Z. Havránek, P. Beneš, and S. Klusacek. Free-field calibration of mems microphone array used for acoustic holography. *21st International Congress on Sound and Vibration 2014, ICSV 2014*, **6**:4513–4520, 2014.

[13] K. D. Pavate, J. D. Jain, and M. R. Kapoor. Acoustical environment for calibration of microphones. *IETE Journal of Research*, **8**(3):159–164, 1962.

[14] M. Melon, C. Langrenne, P. Herzog, and A. Garcia. Evaluation of a method for the measurement of subwoofers in usual rooms. *The Journal of the Acoustical Society of America*, **127**(1):256–263, 2010.

[15] C. Bellmann, W. Klippel, and D. Knobloch. Holographic loudspeaker measurement based on near field scanning. In *DAGA 2015 Nürnberg*, pp. 75–76, 2015.

[16] W. Klippel and C. Bellmann. Holographic nearfield measurement of loudspeaker directivity. In *AES 141 Convention*, number 9598, 2016.

[17] Sound system equipment - Part 5: Loudspeakers. IEC 60268-5:2003/AMD1:2007, International Electrotechnical Commision, Geneva, Switzerland, 2007.

[18] L. L. Beranek and H. P. Sleeper , Jr. The design and construction of anechoic sound chambers. *The Journal of the Acoustical Society of America*, **18**(1):140–150, 1946.

[19] A. Nash. Qualification of an anechoic chamber. In *Proceedings of the 23rd International Congress on Acoustics*, pp. 1343–1349, Aachen, Germany, 2019. Deutsche Gesellschaft für Akustik.

[20] V. F. Kopiev, V. V. Palchikovskiy, Yu. V. Bersenev, S. Y. Makashov, I. V. Belyaev, I. A. Korin, E. V. Sorokin, I. V. Khramtsov, and O. Y. Kustov. Design and qualification of an anechoic facility in PNRPU. *Procedia Engineering*, **176**:264–272, 2017. Proceedings of the 3rd International Conference on Dynamics and Vibroacoustics of Machines (DVM2016) June 29–July 01, 2016 Samara, Russia.

[21] C. Zwikker and C. W. Kosten. *Sound Absorbing Materials*. Elsevier Publishing Company, New York, 1949.

[22] C. Jiang, S. Zhang, and L. Huang. On the acoustic wedge design and simulation of anechoic chamber. *Journal of Sound and Vibration*, **381**:139–155, 2016.

[23] X. Duanqi, W. Zheng, and C. Jinjing. Acoustic design of an anechoic chamber. *Applied Acoustics*, **29**(2):139–149, 1990.

[24] M. E. T. Nejad, A. Loghmani, and S. Ziaei-Rad. The effects of wedge geometrical parameters and arrangement on the sound absorption coefficient – a numerical and experimental study. *Applied Acoustics*, **169**:107458, 2020.

[25] W. A. Davern and J. A. E. Hutchinson. Polyurethane ether foam wedges for anechoic chamber. *Applied Acoustics*, **4**(4):287–302, 1971.

[26] W. Koidan, G. R. Hruska, and M. A. Pickett. Wedge design for national bureau of standards anechoic chamber. *The Journal of the Acoustical Society of America*, **52**(4A):1071–1076, 1972.

[27] V. Mohanan, O. Sharma, and A. F. Chhapgar. Sound absorption by conical absorbers and glasswool layer combination. *Applied Acoustics*, **22**(2):91–101, 1987.

[28] I. V. Belyaev, A. Y. Golubev, A. Y. Zverev, S. Y. Makashov, V. V. Palchikovskiy, A. F. Sobolev, and V. V. Chernykh. Experimental investigation of sound absorption of acoustic wedges for anechoic chambers. *Acoustical Physics*, **61**(5):606 – 614, 2015.

[29] J. Spetzler and R. Snieder. The Fresnel volume and transmitted waves. *Geophysics*, **69**(3):653–663, 2004.

[30] T. S. Becker, D.-J. van Manen, C. M. Donahue, C. Bärlocher, N. Börsing, F. Broggini, T. Haag, J. O. A. Robertsson, D. R. Schmidt, S. A. Greenhalgh, and T. E. Blum. Immersive wave propagation experimentation: Physical implementation and one-dimensional acoustic results. *Physical Review X*, **8**(3):031011, 2018.

[31] S. Schneider and C. Kern. Acoustical behavior of the large anechoic chamber at the Laboratoire de Mécanique et d'Acoustique in the low frequency range. *Acta Acustica united with Acustica*, **94**:141–147, 2008.

[32] R. R. Boullosa and A. P. Lopez. Some acoustical properties of the anechoic chamber at the Centro de Instrumentos, Universidad Nacional Autonoma de Mexico. *Applied Acoustics*, **56**(3):199–207, 1999.

[33] B. Cuyx, W. Desmet, W. Buyens, and T. van Waterschoot. Design and validation of a low-cost acoustic anechoic chamber. *Journal of the Audio Engineering Society*, **149**:1–5, 2020.

[34] M. S. Ressl and P. E. Wundes. Design of an acoustic anechoic chamber for application in hearing aid research. In *Proceedings of the 11th WSEAS International Conference on Acoustics & Music: Theory & Applications*, p. 18–23, Iasi, Romania, 2010. World Scientific and Engineering Academy and Society (WSEAS).

[35] X. Duanqi, W. Zheng, and C. Jinjing. Acoustic design of an anechoic chamber. *Applied Acoustics*, **29**(2):139 – 149, 1990.

[36] S. J. Elliott and P. A. Nelson. Active noise control. *IEEE Signal Processing Magazine*, **10**(4):12–35, 1993.

[37] S. Rajappan, P. Bhaskaran, and R. Prasanth. An insight into the composite materials for passive sound absorption. *Journal of Applied Sciences*, **17**:339–356, 2017.

[38] ANC for crawler crane (masterteck 7090). `http://www.anc-labo.com/en/CrawlerCraneAncResult.pdf`. Accessed: 2024-04-08.

[39] J. Cheer and S. J. Elliott. Active noise control of a diesel generator in a luxury yacht. *Applied Acoustics*, **105**:209–214, 2016.

[40] Active noise control. `https://mediahub.merford.com/m/db2f4b7330fa0bd/original/Active-noise-control.pdf`. Accessed: 2024-04-08.

[41] J. Landaluze, I. Portilla, J.M. Pagalday, A. Martínez, and R. Reyero. Application of active noise control to an elevator cabin. *Control Engineering Practice*, **11**(12):1423–1431, 2003.

[42] Super noise-barrier. `https://www.ihi.co.jp/inc/laneng/catalog/pdf/ace.pdf`. Accessed: 2024-04-08.

[43] Y. Jiang, S. Chen, H. Meng, Z. Zhou, and W. Lv. A novel adaptive step-size hybrid active noise control system. *Applied Acoustics*, **182**:108285, 2021.

[44] S. J. Elliott. *Signal Processing for Active Control*. Signal Processing and its Applications. Academic Press, California, USA, 2001.

[45] P. Gardonio, E. Bianchi, and S. J. Elliott. Smart panel with multiple decentralized units for the control of sound transmission. Part I: Theoretical predictions. *Journal of Sound and Vibration*, **274**(1):163–192, 2004.

[46] C. Antoñanzas, M. Ferrer, A. Gonzalez, M. de Diego, and G. Piñero. Diffusion algorithm for active noise control in distributed networks. In *22nd International Congress on Sound and Vibration*, pp. 12–16, Florence, Italy, 2015.

[47] K. D. Frampton, O. N. Baumann, and P. Gardonio. A comparison of decentralized, distributed, and centralized vibro-acoustic control. *The Journal of the Acoustical Society of America*, **128**(5):2798–2806, 2010.

[48] G. Zhang, J. Tao, X. Qiu, and I. Burnett. Decentralized two-channel active noise control for single frequency by shaping matrix eigenvalues. *IEEE/ACM Transactions on Audio, Speech, and Language Processing*, **27**(1):44–52, 2019.

[49] C. Antoñanzas, M. Ferrer, M. de Diego, and A. Gonzalez. Blockwise frequency domain active noise controller over distributed networks. *Applied Sciences*, **6**:124, 2016.

[50] S. Spors and H. Buchner. Efficient massive multichannel active noise control using wave-domain adaptive filtering. In *Proceedings of 2008 3rd International Symposium on Communications, Control and Signal Processing*, pp. 1480–1485, 2008.

[51] S. W. Cho, H. Kim. Variable step-size normalized LMS algorithm by approximating correlation matrix of estimation error. *Signal Processing*, **90**(9):2792–2799, 2010.

[52] F. Lindström, C. Schüldt, and I. Claesson. Efficient multichannel NLMS implementation for acoustic echo cancellation. *EURASIP Journal on Audio Speech and Music Processing*, **2007**:1–6, 2007.

[53] M. R. Bai and S. J. Elliott. Preconditioning multichannel adaptive filtering algorithms using EVD- and SVD-based signal prewhitening and system decoupling. *Journal of Sound and Vibration*, **270**:639 – 655, 2004.

[54] A. P. Berkhoff and G. Nijsse. A rapidly converging filtered-error algorithm for multichannel active noise control. *Journal of Adaptive Control and Signal Processing*, **21**:556 – 569, 2007.

[55] A. H. Sayed. *Fundamentals of Adaptive Filtering*. Wiley, New York, USA, 2003.

[56] F. Yu and M. Bouchard. Recursive least-squares algorithms with good numerical stability for multichannel active noise control. In *2001 IEEE International Conference on Acoustics, Speech, and Signal Processing. Proceedings (Cat. No.01CH37221)*, volume 5, pp. 3221–3224, 2001.

[57] J. Cioffi and T. Kailath. Fast, recursive-least-squares transversal filters for adaptive filtering. *IEEE Transactions on Acoustics, Speech, and Signal Processing*, **32**(2):304–337, 1984.

[58] L. Rey Vega, H. Rey, J. Benesty, and S. Tressens. A fast robust recursive least-squares algorithm. *IEEE Transactions on Signal Processing*, **57**(3):1209–1216, 2009.

[59] S. Veres. Model-based control design for AVC. In O. Tokhi, editor, *Active Sound and Vibration Control: theory and applications*, pp. 135–158. Institution of Engineering and Technology, Stevenage, United Kingdom, 2002.

[60] P. A. Nelson and S. J. Elliott. *Active Control of Sound*. Academic Press, London, 1992.

[61] L. Litwin. FIR and IIR digital filters. *IEEE Potentials*, **19**(4):28–31, 2000.

[62] M. Verhaegen and V. Verdult. *Filtering and System Identification: A Least Squares Approach*. Cambridge University Press, Cambridge, United Kingdom, 2007.

[63] Z. Wu, V. K. Varadan, and V. V. Varadan. Time-domain analysis and synthesis of active noise control systems in ducts. *The Journal of the Acoustical Society of America*, **101**(3):1502–1511, 1997.

[64] S. Boyd, V. Balakrishnan, E. Feron, and L. ElGhaoui. Control system analysis and synthesis via linear matrix inequalities. In *1993 American Control Conference*, pp. 2147–2154, 1993.

[65] P. Van Overschee and B. De Moor. *Subspace Identification for Linear Systems*. Kluwer, Boston, 1996.

[66] M. Verhaegen. Identification of the deterministic part of MIMO state space models given in innovations form from input-output data. *Automatica*, **30**(1):61–74, 1994.

[67] M. Viberg. Subspace-based methods for the identification of linear time-invariant systems. *Automatica*, **31**(12):1835–1851, 1995.

[68] M. O. Tokhi and R. Wood. Active noise control using multi-layered perceptron neural networks. *Journal of Low Frequency Noise, Vibration and Active Control*, **16**(2):109–144, 1997.

[69] H. Zhang and D. Wang. A deep learning approach to active noise control. In *Proc. Interspeech 2020*, pp. 1141–1145, 2020.

[70] Y. Jang, J. Park, W. Lee, and H. Park. A convolution-neural-network feedforward active-noise-cancellation system on FPGA for in-ear headphone. *Applied Sciences*, **12**(11), 2022.

[71] N. Levinson. The Wiener (root mean square) error criterion in filter design and prediction. *Journal of Mathematics and Physics*, **25**(1-4):261–278, 1946.

[72] J.G. Proakis. *Algorithms for Statistical Signal Processing*. Prentice Hall, New Jersey, 2002.

[73] B. Raeisy and S. Golbahar Haghighi. Active noise controller with reinforcement learning. In *The 16th CSI International Symposium on Artificial Intelligence and Signal Processing (AISP 2012)*, pp. 074–079, 2012.

[74] S. A. Hoseini Sabzevari and M. Moavenian. Application of reinforcement learning for active noise control. *Turkish Journal of Electrical Engineering & Computer Sciences*, **25**:2606–2613, 2017.

[75] H. Zhu, R. Rajamani, and K. A. Stelson. Active control of acoustic reflection, absorption, and transmission using thin panel speakers. *The Journal of the Acoustical Society of America*, **113**(2):852–870, 2003.

[76] E. Friot and C. Bordier. Real-time active suppression of scattered acoustic radiation. *Journal of Sound and Vibration*, **278**(3):563 – 580, 2004.

[77] E. Friot, R. Guillermin, and M. Winninger. Active control of scattered acoustic radiation: a real-time implementation for a three-dimensional object. *Acta Acustica united with Acustica*, **92**:278–288, 2006.

[78] D. Habault, E. Friot, P. Herzog, and C. Pinhede. Active control in an anechoic room: Theory and first simulations. *Acta Acustica united with Acustica*, **103**:369–378, 2017.

[79] C. Pinhède and P. Herzog. Design and measurement of a reference source at lower frequencies. In *Proc. Forum Acusticum*, pp. 3365–3372, Lyon, France, 2020.

[80] X. Li, T. Becker, M. Ravasi, J. Robertsson, and D.-J. van Manen. Closed-aperture unbounded acoustics experimentation using multidimensional deconvolution. *The Journal of the Acoustical Society of America*, **149**(3):1813–1828, 2021.

[81] D. Guicking and E. Lorenz. An active sound absorber with porous plate. *Journal of Vibration, Acoustics, Stress, and Reliability in Design*, **106**(3):389–392, 1984.

[82] S. Beyene and R. A. Burdisso. A new hybrid passive–active noise absorption system. *The Journal of the Acoustical Society of America*, **101**(3):1512–1515, 1997.

[83] J. P. Smith, B. D. Johnson, and R. A. Burdisso. A broadband passive–active sound absorption system. *The Journal of the Acoustical Society of America*, **106**(5):2646–2652, 1999.

[84] D. Thenail, O. Lacour, M. A. Galland, and M. Furstoss. The active control of wall impedance. In *Acta Acustica united with Acustica*, volume 83, pp. 1039–1044, 2011.

[85] T. W. Leishman and J. Tichy. On the significance of reflection coefficients produced by active surfaces bounding one-dimensional sound fields. *The Journal of the Acoustical Society of America*, **113**(3):1475–1482, 2003.

[86] D. Guicking. Coherent active methods for applications in room acoustics. *The Journal of the Acoustical Society of America*, **74**(S1):S26–S26, 2005.

[87] O. Lacour, M. A. Galland, and D. Thenail. Preliminary experiments on noise reduction in cavities using active impedance changes. *Journal of Sound and Vibration*, **230**(1):69–99, 2000.

[88] E. Friot, A. Gintz, P. Herzog, and S. Schneider. Improving absorption of sound using active control. In H. Ulbrich and L. Ginzinger, editors, *Motion and Vibration Control*, pp. 83–91, Dordrecht, 2009. Springer Netherlands.

[89] N. Börsing, T. S. Becker, A. Curtis, D.-J. van Manen, T. Haag, and J. O.A. Robertsson. Cloaking and holography experiments using immersive boundary conditions. *Phys. Rev. Appl.*, **12**:024011, 2019.

[90] H. R. Thomsen, M. Molerón, T. Haag, D.-J. van Manen, and J. O. A. Robertsson. Elastic immersive wave experimentation: Theory and physical implementation. *Phys. Rev. Res.*, **1**:033203, 2019.

[91] X. Li, J. Robertsson, and D.-J. van Manen. Elastic immersive wave experimentation. *Geophysical Journal International*, **233**(1):724–739, 2022.

[92] J. Cheer. Active control of scattered acoustic fields: Cancellation, reproduction and cloaking. *Journal of Acoustical Society of America*, **140**:1502–1512, 2016.

[93] F. Fahy. Chapter 12 - reflection, scattering, diffraction and refraction. In F. Fahy, editor, *Foundations of Engineering Acoustics*, pp. 352–379. Academic Press, London, 2001.

[94] A. Weill. Acoustic waves, scattering. In E. G. Njoku, editor, *Encyclopedia of Remote Sensing*, pp. 13–16. Springer New York, New York, 2014.

[95] J. Piechowicz. Sound wave diffraction at the edge of a sound barrier. *Acta Physica Polonica Series A*, **119**:1040–1045, 2011.

[96] D. T. Blackstock. *Fundamentals of Physical Acoustics*. A Wiley-Interscience publication. John Wiley & Sons, New York, 2000.

[97] J. Lekner. *Introducing reflection*, pp. 1–32. Springer Netherlands, Dordrecht, 1987.

[98] J. Cao, J. Liu, J. Wang, and X. Lai. Acoustic vector sensor: reviews and future perspectives. *IET Signal Processing*, **11**(1):1–9, 2017.

[99] H. E. de Bree. The Microflown, an acoustic particle velocity sensor. *Acoustics Australia*, **31**(3):91–94, 2003.

[100] A. Schroeder and C. E. Willert. *Particle Image Velocimetry*. Springer Berlin, 2008.

[101] A. D. Pierce. *Acoustics: An Introduction to Its Physical Principles and Applications*. Acoustical Society of America, 1989.

[102] P. M. Morse and K. U. Ingard. *Theoretical Acoustics*. International series in pure and applied physics. McGraw-Hill, 1968.

[103] R. N. Bracewell. *The Fourier Transform and Its Applications*. Circuits and systems. McGraw-Hill, 2000.

[104] J.-C. Nédélec. The Helmholtz equation. In *Acoustic and Electromagnetic Equations: Integral Representations for Harmonic Problems*, pp. 9–109. Springer New York, New York, 2001.

[105] A. Sommerfeld. *Partial Differential Equations in Physics*. Elsevier Science, 1949.

[106] I. Pollack. Specification of sound-pressure levels. *The American Journal of Psychology*, **62**(3):412–417, 1949.

[107] H. Teutsch. *Modal Array Signal Processing: Principles and Applications of Acoustic Wavefield Decomposition*. Lecture Notes in Control and Information Sciences. Springer, Berlin, 2007.

[108] P. Peretti, S. Cecchi, L. Romoli, and F. Piazza. *Performance Evaluation of Adaptive Algorithms for Wave Field Analysis/Synthesis Using Sound Field Simulations*, chapter 25, pp. 543–560. IntechOpen, Rijeka, 2011.

[109] S. Marburg. Boundary element method for time-harmonic acoustic problems. In M. Kaltenbacher, editor, *Computational Acoustics*, pp. 69–158, Cham, 2018. Springer International Publishing.

[110] M. Abramowitz and I. A. Stegun. *Handbook of Mathematical Functions: With Formulas, Graphs, and Mathematical Tables*. Applied mathematics series. Dover Publications, 1965.

[111] M. R. Schroeder. New method of measuring reverberation time. *The Journal of the Acoustical Society of America*, **37**(3):409–412, 1965.

[112] T. Kailath. *Linear Systems*. Information and System Sciences Series. Prentice-Hall, 1980.

[113] B. Fang, A. G. Kelkar, S. M. Joshi, and H. R. Pota. Modelling, system identification, and control of acoustic–structure dynamics in 3-D enclosures. *Control Engineering Practice*, **12**(8):989–1004, 2004. Special Section on Emerging Technologies for Active Noise and Vibration Control Systems.

[114] L. Ljung. *System Identification: Theory for the User*. Prentice Hall information and System Sciences Series. Prentice Hall, New Jersey, 1999.

[115] B. D. O. Anderson and J. B. Moore. *Optimal Filtering*. Information and System Sciences series. Prentice-Hall, New Jersey, 1979.

[116] S. M. Kuo. *Active noise control systems*. John Wiley & Sons, New York, 1996.

[117] A. Fettweis. Wave digital filters: Theory and practice. *Proceedings of the IEEE*, **74**(2):270–327, 1986.

[118] L. Wanhammar and Y. Yu. Chapter 6 - Digital filter structures and their implementation. In Paulo S.R. Diniz, editor, *Signal Processing and Machine Learning Theory*, pp. 267–401. Academic Press, London, United Kingdom, 2024.

[119] S. Gudvangen and S. J. Flockton. Modelling of acoustic transfer functions for echo cancellers. *IEE Proceedings - Vision, Image and Signal Processing*, **142**:47–51(4), 1995.

[120] A. P. Liavas and P. A. Regalia. Acoustic echo cancellation: Do IIR models offer better modeling capabilities than their FIR counterparts? *Signal Processing, IEEE Transactions on*, **46**:2499 – 2504, 1998.

[121] D. Sundararajan. *Digital Signal Processing: An Introduction*. Springer International Publishing, Cham, 2024.

[122] Y. Zhuang and Y. Liu. A stable IIR filter design approach for high-order active noise control applications. *Acoustics*, **5**(3):746–758, 2023.

[123] L. S. H. Ngia and F. Gustafson. Using Kautz filter for adaptive acoustic echo cancellation. In *Conference Record of the Thirty-Third Asilomar Conference on Signals, Systems, and Computers*, volume 2, pp. 1110–1114, 1999.

[124] M. Benzi. *Exploiting Hidden Structure in Matrix Computations: Algorithms and Applications*. Springer International Publishing, Cham, 2016.

[125] H. Akaike. Block Toeplitz matrix inversion. *SIAM Journal on Applied Mathematics*, **24**(2):234–241, 1973.

[126] S. M. Kay. *Fundamentals of Statistical Signal Processing: Estimation theory*. Fundamentals of Statistical Signal Processing. PTR Prentice-Hall, New Jersey, 1993.

[127] R. Bitmead and B. Anderson. Asymptotically fast solution of Toeplitz and related systems of linear equations. *Linear Algebra and its Applications*, **34**:103 – 116, 1980.

[128] G. S. Ammar and W. B. Gragg. Superfast solution of real positive definite Toeplitz systems. *SIAM Journal on Matrix Analysis and Applications*, **9**(1):61–76, 1988.

[129] R. Brent, F. Gustavson, and D. Yun. Fast solution of Toeplitz systems of equations and computation of Padé approximants. *Journal of Algorithms*, **1**(3):259 – 295, 1980.

[130] F. Hoog. A new algorithm for solving Toeplitz systems of equations. *Linear Algebra and its Applications*, **88-89**:123 – 138, 1987.

[131] E. H. Bareiss. Numerical solution of linear equations with Toeplitz and vector Toeplitz matrices. *Numerische Mathematik*, **13**:404–424, 1969.

[132] T. Kailath, S. Kung, and M. Morf. Displacement ranks of matrices and linear equations. *Journal of Mathematical Analysis and Applications*, **68**(2):395–407, 1979.

[133] S. Chandrasekaran, N. Govindarajan, and A. Rajagopal. Fast algorithms for displacement and low-rank structured matrices. In *Proceedings of the 2018 ACM International Symposium on Symbolic and Algebraic Computation*, pp. 17–22. Association for Computing Machinery, 2018.

[134] Z. Sheng, P. Dewilde, and S. Chandrasekaran. *Algorithms to solve hierarchically semi-separable systems*, pp. 255–294. Birkhäuser Basel, Basel, 2007.

[135] J. Xia, S. Chandrasekaran, M. Gu, and X. S. Li. Fast algorithms for hierarchically semiseparable matrices. *Numerical Linear Algebra with Applications*, **17**(6):953–976, 2010.

[136] K. Lessel, M. Hartman, and S. Chandrasekaran. A fast memory efficient construction algorithm for hierarchically semi-separable representations. *SIAM Journal on Matrix Analysis and Applications*, **37**:338–353, 2016.

[137] J. Xia, Y. Xi, and M. Gu. A superfast structured solver for Toeplitz linear systems via randomized sampling. *SIAM Journal on Matrix Analysis and Applications*, **33**(3):837–858, 2012.

[138] R. H. Chan and M. K. Ng. Conjugate gradient methods for Toeplitz systems. *SIAM Review*, **38**(3):427–482, 1996.

[139] R. Chan and X. Jin. *An Introduction to Iterative Toeplitz Solvers*. Society for Industrial and Applied Mathematics, Philadelphia, 2007.

[140] T. F. Chan and J. A. Olkin. Circulant preconditioners for Toeplitz-block matrices. *Numberical Algorithms*, **6**:89 – 101, 1992.

[141] T. F. Chan. An optimal circulant preconditioner for Toeplitz systems. *SIAM Journal on Scientific and Statistical Computing*, **9**(4):766–771, 1988.

[142] M. Cai, X. Jin, and Y. Wei. A generalization of T. Chan's preconditioner. *Linear Algebra and its Applications*, **407**:11 – 18, 2005.

[143] X. Lv, T. Huang, and Z. Ren. A modified T. Chan's preconditioner for Toeplitz systems. *Computers & Mathematics with Applications*, **58**(4):693 – 699, 2009.

[144] M. Domínguez-Jiménez and P. Ferreira. A new preconditioner for Toeplitz matrices. *Signal Processing Letters, IEEE*, **16**:758 – 761, 2009.

[145] L. Wan, C. Yu, S. Pan, F. Gao, and Q. Wen. Quantum algorithm for the Toeplitz systems. *arXiv: Quantum Physics*, pp. 1–9, 2016.

[146] L. Wan, C. Yu, S. Pan, F. Gao, Q. Wen, and S. Qin. Asymptotic quantum algorithm for the Toeplitz systems. *Physical Review A*, **97**:062322, 2018.

[147] E. A. Wan. Adjoint LMS: an efficient alternative to the filtered-x LMS and multiple error LMS algorithms. In *1996 IEEE International Conference on Acoustics, Speech, and Signal Processing Conference Proceedings*, volume 3, pp. 1842–1845, 1996.

[148] R. Haasjes and A. P. Berkhoff. An efficient offline scheme to compute an FIR controller for active reduction of acoustic reflections in an anechoic chamber. *Journal of Sound and Vibration*, **573**:118198, 2024.

[149] R. Haasjes and A. P. Berkhoff. A small-scale active anechoic chamber. *Applied Acoustics*, **224**:110130, 2024.

[150] R. Haasjes and A. P. Berkhoff. A solution method for active suppression of reflections in anechoic chambers. *The Journal of the Acoustical Society of America*, 2024, submitted.

[151] S. Lang. Green's theorem. In *Calculus of Several Variables*, pp. 269–290. Springer New York, New York, 1987.

[152] E. Hulsebos, D. de Vries, and E. Bourdillat. Improved microphone array configurations for auralization of sound fields by wave-field synthesis. *J. Audio Eng. Soc*, **50**(10):779–790, 2002.

[153] A. P. Berkhoff. Fixed gain multichannel active noise control with disturbance dependent objectives and iterative solution. *The Journal of the Acoustical Society of America*, **149**(1):645–651, 2021.

[154] R. M. Howard. The power spectral density. In *Principles of Random Signal Analysis and Low Noise Design: The Power Spectral Density and its Applications*, pp. 59–91, New York, 2002. Wiley-Interscience.

[155] B. Noble and J. W. Daniel. *Applied Linear Algebra*. Prentice-Hall, New Jersey, 1988.

[156] S. J. Elliott. Optimal controllers and adaptive controllers for multichannel feedforward control of stochastic disturbances. *IEEE Transactions on Signal Processing*, **48**(4):1053–1060, 2000.

[157] G. H. Golub and C. F. Van Loan. *Matrix Computations*. Johns Hopkins University Press, Baltimore, 1989.

[158] A. P. Berkhoff, P. M. van den Berg, and J. M. Thijssen. Iterative calculation of reflected and transmitted acoustic waves at a rough interface. *IEEE Transactions on Ultrasonics, Ferroelectrics, and Frequency Control*, **42**(4):663–671, 1995.

[159] E. Por, M. van Kooten, and V. Sarkovic. Nyquist–shannon sampling theorem, 2019. `https://home.strw.leidenuniv.nl/~por/AOT2019/docs/AOT_2019_Ex13_NyquistTheorem.pdf`. Accessed: 2024-04-08.

[160] A. B. Williams and F. J. Taylor. *Electronic Filter Design Handbook, Fourth Edition*. McGraw-Hill Education, London, 2006.

[161] P. Welch. The use of fast Fourier transform for the estimation of power spectra: A method based on time averaging over short, modified periodograms. *IEEE Transactions on Audio and Electroacoustics*, **15**(2):70–73, 1967.

[162] A. P. Berkhoff. Decentralized feedback damping with distributed control applied to ducts and anechoic chambers. In *proc ISMA 2024*, pp. 40–54, Leuven, 2024.

[163] R. H. Small. Direct radiator loudspeaker system analysis. *J. Audio Eng. Soc*, **20**(5):383–395, 1972.

[164] R. H. Small. Closed-box loudspeaker systems-part 2: Synthesis. *J. Audio Eng. Soc*, **21**(1):11–18, 1973.

[165] A. Nowoświat. Determination of the reverberation time using the measurement of sound decay curves. *Applied Sciences*, **13**(8607):1–15, 2023.

[166] C. Hak, R. Wenmaekers, and L. Luxemburg. Measuring room impulse responses: Impact of the decay range on derived room acoustic parameters. *Acta Acustica united with Acustica*, **98**:907–915, 2012.

[167] T. Martin and A. Roure. Optimization of an active noise control system using spherical harmonics expansion of the primary field. *Journal of Sound and Vibration*, **201**(5):577–593, 1997.

[168] C. R. Duke, S. D. Sommerfeldt, K. L. Gee, and C. V. Duke. Optimization of control source locations in free-field active noise control using a genetic algorithm. *Noise Control Engineering Journal*, **57**(3):221–231, 2009.

[169] D. Moreau, B. S. Cazzolato, A. C. Zander, and C. D. Petersen. A review of virtual sensing algorithms for active noise control. *Algorithms*, **1**(2):69–99, 2008.

[170] C. D. Petersen, R. Fraanje, B. S. Cazzolato, A. C. Zander, and C. H. Hansen. A Kalman filter approach to virtual sensing for active noise control. *Mechanical Systems and Signal Processing*, **22**(2):490–508, 2008.

List of publications

Journal articles

- R. Haasjes and A.P. Berkhoff. An efficient offline scheme to compute an FIR controller for active reduction of acoustic reflections in an anechoic chamber. *Journal of Sound and Vibration*, **573**:118198, 2024.
- R. Haasjes and A.P. Berkhoff. A small-scale active anechoic chamber. *Applied Acoustics*, **224**:110130, 2024.
- R. Haasjes and A.P. Berkhoff. A solution method for active suppression of reflections in anechoic chambers. *The Journal of the Acoustical Society of America*, 2024, submitted.

Conference contributions

First author

- R. Haasjes, A.P. Berkhoff and B. Rosic. Scalable active noise reduction of acoustic reflections in an anechoic chamber. 24^{th} *Engineering Mechanics Symposium*, p. 46, Arnhem, 2021.
- R. Haasjes, A.P. Berkhoff and B. Rosic. Computing an FIR controller using an efficient iterative scheme. 41^{st} *Benelux Meeting on Systems and Control*, p. 156 Brussels, 2022.
- R. Haasjes and A.P. Berkhoff. Active noise control in anechoic chambers using an efficient scheme incorporating frequency-domain derived filters. 25^{th} *Engineering Mechanics Symposium*, p. 93, Arnhem, 2022.
- R. Haasjes and A.P. Berkhoff. An efficient iterative scheme to compute an FIR filter. $42^{\boldsymbol{nd}}$ *Benelux Meeting on Systems and Control*, p. 43, Elspeet, 2023.
- R. Haasjes and A.P. Berkhoff. Towards a small-scale active anechoic chamber. 26^{th} *Engineering Mechanics Symposium*, p. 91, Arnhem, 2023.

- R. Haasjes and A.P. Berkhoff. Realtime control of the reflected sound field in a small-scale active anechoic chamber. *Proceedings of the* 30^{th} *International Congress on Sound and Vibration*, number 684, Amsterdam, 2024.

Co-author

- A.P. Berkhoff and R. Haasjes. Active noise control using a modified filtered-error algorithm with frequency domain decoupling. *Proceedings of ISMA*2022 *International Conference on Noise and Vibration Engineering*, pp. 155–161, Leuven, 2022.

Dankwoord

De laatste pagina's van dit proefschrift wil ik gebruiken om iedereen die direct of indirect heeft bijgedragen aan dit promotieonderzoek te bedanken.

Bojana, thank you for your supportive and cheerful supervision, for giving me the opportunity to be a doctoral student in your group, for your feedback on my work, your enthusiasm, and the social gatherings with the team.

Arthur, mijn interesse in de akoestiek gecombineerd met signaalverwerking ontstond tijdens jouw vak *Signal processing for Acoustics and Vibration*, waarna ik vervolgens onder jouw begeleiding het afstudeeronderzoek *Active noise control with reduced-order vibro-acoustic models* heb mogen doen. Ik weet nog goed dat je tijdens het afstudeeronderzoek vroeg of ik interesse had in een PhD, terwijl ik daar tot op dat moment eigenlijk nooit goed over na had gedacht. Uiteindelijk heeft dit geleid tot dit proefschrift. Ik wil jou bedanken voor een ontzettend fijne begeleiding, je feedback, al je ideeën, het meedenken, de wandelingen in de pauzes, de laagdrempeligheid waarmee ik altijd bij jou terecht kon voor vragen of overleg, en natuurlijk voor het vertrouwen.

Ik wil TNO bedanken voor de financiering, ondersteuning en het mogelijk maken van dit onderzoek. Jan, bedankt voor jouw input en sturing in de beginfase van het onderzoek.

I would like to thank the defence committee members, prof. M.J. Bentum, prof. G.J.T. Leus, prof. P. Gardonio, prof. P.H. Veltink and prof. C.H. Venner for their feedback on my thesis and the assessment of my work.

Axel, jij hebt een enorme bijdrage geleverd aan het experimentele onderzoek. Bedankt voor je hulp bij het assembleren en klaarmaken van de opstelling, het solderen, het meedenken, het opsporen van hardwareproblemen, het kalibreren van de microfoons, de leuke gesprekken in het akoestisch lab en voor het aanhoren van mijn frustraties wanneer het soms niet wilde lukken.

Henny, bedankt voor het ontwerp van de voorversterkers, waardoor het mogelijk was om zoveel microfoons te gebruiken bij de metingen. Ook bedankt voor de praktische tips die je gaf toen ik met het ontwerp van de opstelling bezig was.

Debbie, bedankt voor het regelen van alles rondom dit promotieonderzoek en voor de gezellige gesprekken.

Luc, Minke en Vasos, bedankt voor het gezellige kantoor, de leuke gesprekken, de mogelijkheid om af en toe mijn frustraties rondom het promoveren even te uiten, en voor alle gezelligheid tijdens en na werktijd.

Wouter, ik vond het fijn dat we samen een aantal conferenties en vakken konden volgen. Dankjewel voor de gezellige koffiepauzes en lunchwandelingen, al jouw tips en suggesties, het meedenken en het template voor dit proefschrift.

Tim, bedankt voor de gezellige koffiepauzes en lunchwandelingen, de leuke gesprekken, potjes poolen, diners, en natuurlijk de geweldige vakantie.

Astrid, Bram, Jip, Jordy, Jurnan, Karlijn, Koen, Marijn, Merit, Ronald, Sil, Timm, Wouter en alle andere AMDA- en PE-leden: bedankt voor de gezellige koffiepauzes en lunchwandelingen.

Ik wil alle vrienden van 'thuis' bedanken, en in het bijzonder Dionne, Floris, Reno en Sarin. Terwijl ik met dit onderzoek bezig was, hebben we zo ontzettend veel leuke ervaringen gedeeld. Bedankt daarvoor!

De laatste woorden van dit proefschrift wil ik wijden aan pa, ma, Annemarth, Julian en verdere familie. Bedankt voor de interesse en steun in de afgelopen jaren, ook al was het soms lastig uitleggen wat ik nou precies deed. Ik hoop dat de presentatie bij mijn verdediging meer duidelijkheid zal geven.